Quantum many-body systems and Tensor Network algorithms

Dissertation submitted for the award of the title

"Doctor of Natural Sciences"

to the Faculty of Physics, Mathematics and Computer Science
of Johannes Gutenberg University Mainz

By

Augustine Kshetrimayum
born in Imphal (India)

Mainz, September 2017

Abstract

Theory of quantum many-body systems plays a key role in understanding the properties of phases of matter found in nature. Due to the exponential growth of the dimensions of the Hilbert space with the number of particles, quantum many-body problems continue to be one of the greatest challenges in physics and most of these systems are impossible to study exactly. We therefore need efficient and accurate numerical algorithms to understand them. In this thesis, we exploit a new numerical technique known as Tensor Network algorithms to study exotic phases of matter in three different investigations in one and two spatial dimensions.

In the first part, we use Matrix Product States which is a one-dimensional ansatz of the Tensor Network family to study trivial and topological phases of matter protected by symmetries in a spin-2 quantum chain. For this, we investigate a Heisenberg-like model with bilinear, biquadratic, bicubic and biquartic interactions with an additional uniaxial anisotropy term. We also add a staggered magnetic field afterwards to break the symmetries protecting the topological phases and study their ground state properties.

In the second part of the thesis, we use Tensor Network States in 2D known as Projected Entangled Pair States to study frustrated quantum systems in a kagome lattice, more specifically, the XXZ model. We study the emergence of different magnetization plateaus by adding an external magnetic field and show the delicate interplay between the number of unit cells and the symmetry of the ground state.

Finally, we propose an algorithm based on Tensor Networks to study open dissipative quantum systems in 2D. We then use it to investigate the spin-1/2 Ising and the XYZ model in a square lattice, both of which can be realized experimentally using cold Rydberg atoms.

Publications

This thesis contains the following publications by the author.

1) A. Kshetrimayum, H.-Hao Tu, R. Orus, "All spin-1 topological phases in a single spin-2 chain", Physical Review B **91**, 205118 (2015).

2) A. Kshetrimayum, H.-Hao Tu, R. Orus,"Symmetry-protected intermediate trivial phases in quantum spin chains", Physical Review B **93**, 245112 (2016).

3) A. Kshetrimayum, T. Picot, R. Orus, D. Poilblanc, "Spin-1/2 kagome XXZ model in a field: Competition between lattice nematic and solid orders", Physical Review B **94**, 235146 (2016).

4) A. Kshetrimayum, H. Weimer, R. Orus, "A simple tensor network algorithm for two-dimensional steady states", Nature Communications **8**, 1291 (2017).

Contents

Each path is only one of a million paths. Therefore, you must always keep in mind that a path is only a path. If you feel that you must not follow it, you need not stay with it under any circumstances. Any path is only a path. There is no affront to yourself or others in dropping it if that is what your heart tells you to do. But your decision to keep on the path or to leave it must be free of fear and ambition. I warn you: look at every path closely and deliberately. Try it as many times as you think necessary. Then ask yourself and yourself alone one question. It is this:

Does this path have a heart?

All paths are the same. They lead nowhere. They are paths going through the bush or into the bush or under the bush. Does this path have a heart is the only question. If it does, then the path is good. If it doesn't, then it is of no use.

Carlos Castaneda

Chapter 1

Introduction

Humanity owe its civilization to the discovery of new materials. The importance of such discoveries is highlighted by the fact that different eras of civilization are often named after them: be it the stone, iron or bronze age. From learning how to use tools made of stone to the discovery of iron and steels leading to the industrial revolution, the yearning to discover and develop new materials has never stopped. Today, as our struggle for non-renewable sources of energy gets more alarming, we have to be more and more reliant on renewable forms like the sun and the wind. Converting these raw forms of resources into electricity require electronic devices and this ultimately means finding new materials that have extraordinary properties.

The computer was invented to perform simple computations; now its use has become inevitable in our everyday life. Unfortunately, even the power of such traditional computing, which is based on the silicon chips, is on the verge of collapse and it seems certain that Moore's law [1] will ultimately hit the ceiling in the years to come. One of the ways to solve the crisis posed by the failure of Moore's law would be through the use of quantum computers. Unlike traditional computers, quantum computers would obey the laws of quantum mechanics and its applications have far-reaching consequences in physics, computer science and other related fields. One of the key ingredients in the successful development of quantum computers is Topologically Ordered state [2] which exhibits a new kind of quantum order characterized by non-local topological properties. The importance of these topological states of matter has been brought into the limelight by the 2016 Nobel Prize for Physics awarded to Thouless, Haldane and Kosterlitz for their works on it [3]. Such phases of matter are characterized by interesting features such as robust ground state degeneracy, perfectly conducting edge states, quasi-particle fractional statistics, etc and they have promising applications in quantum computation [4].

Furthermore, with the discovery of exotic scientific phenomena like superconductivity, superfluidity, quantum magnetism, materials like polymers, semiconductors, quantum matters, etc, it will not be over optimistic to assume that there is a lot of hope in taking our civilization to the next level. These exotic materials and phenomena can be harnessed for the purpose of next-level computing and also in many useful everyday applications such as electromagnetic superconducting propelled trains (maglev), more efficient power transmission, cheap solar cells, more efficient LEDs, telecommunications, aiding medical sciences, etc.

The above examples are only few of the prospects of finding new materials and this forms the basic motivation of researchers working in the condensed matter physics community. However, understanding the basic properties of matter is not easy because elementary particles are governed by the laws of quantum mechanics. In addition to this, one of the most fascinating properties of materials science is that even if we understand the properties of every single particle, their collective behavior is often drastically different from their individual properties. This phenomenon is beautifully characterized by the words of Aristotle [5]: *The whole is more than the sum of its parts*. This means that understanding the properties of an atom or an electron is not enough. One needs to understand what happens when a collection of such particles combine to form a system. This is known as emergence and gives rise to many interesting and complicated phenomena such as the ones mentioned above. This requires a proper understanding of the quantum many-body theory as they involve a large number of particles and most of the realistic materials are many-body systems anyway.

Our attempt to study quantum many-body systems is often hampered by the *curse of dimensionality*. This means that the number of parameters required in studying a realistic material scales exponentially with the number of particles. To give a simple example, consider a system containing many particles where each particle is a 2-level system. For a realistic material containing of the order of 10^{23} such particles, the total number of parameters required to describe the system is $\sim O(2^{10^{23}})$. To give an overview, this number is much larger than the estimated total number of atoms in the observable universe ($\sim O(10^{80})$) [6]. Therefore, an exact description of such a realistic material is impossible and hence only a few systems can be exactly studied. For the rest, one has to make numerical approximations and/or study simplistic models that capture the physics of the real materials. To achieve this, a lot of numerical techniques have been developed over the years, each with their own advantages and limitations. Mention may be made of the Exact Diagonalization method (ED) [7],

Quantum Monte Carlo method (QMC) [8], Series Expansion (SE) [9], Continuous Unitary Transformations (CUT) [10, 11], Tensor Network techniques e.g. [12], Mean Field Theory (MFT) [13] etc.

This thesis is about the use of one such technique based on Tensor Networks. These techniques exploit the properties of entanglement between the particles to solve the many-body problem as we will discuss in Chapter 2 and 3 of the thesis. We will use these techniques to investigate three different kinds of systems: (i) a spin-2 chain with Heisenberg-like interactions, (ii) a frustrated 2D system in a kagome lattice with XXZ interaction and (iii) an open dissipative spin-1/2 Ising and XYZ model in a square lattice. The first model is interesting because, as we will show, it hosts many exotic phases of matter which cannot be described using the conventional theory of phase transitions. One of them is the Symmetry Protected Topological phases of matter which have been proposed as a resource in measurement-based quantum computing and other areas of quantum information [14, 15, 16]. Our motivation for investigating the second model is inspired by the search for quantum spin liquid which have been suggested as one of the possible mechanisms to explain high-T_c superconductivity [17]. The kagome lattice provides a good playground to explore these phases because it is highly frustrated. Our investigation of the dissipative spin-1/2 Ising and XYZ model is motivated by the fact that systems, in nature, are not isolated and therefore it is very important to include the effects of the environment. This is to be seen from the context that there are hardly any numerical techniques available to study open dissipative systems in 2D that takes into account the correlations in the system. It has a number of important implications because dissipation can be used to engineer topological phases of matter [18] and also in the context of driven dissipative universal quantum computation [19]. The important results of our investigation can be found in Chapter 4, 5 and 6. Below, we provide a detailed outline of the whole thesis.

In Chapter 2, we make a formal introduction to the concept of entanglement. We briefly discuss the history, importance and its applications. We introduce the concept of qubits and give the formal definition of entanglement and show how one can quantify it. For this, we introduce the concept of Schmidt Decomposition which is a very important tool and its relationship to the Singular Value Decomposition used in linear algebra. Finally in this chapter, we introduce some important concepts relevant in the context of condensed matter physics such as the Variational Principle and Quantum Phase Transitions. We also take the example of the spin-1/2 Transverse Field Ising model and familiarize ourselves with concepts such as symmetry broken states, local

order parameters, etc which will be very useful in understanding Symmetry Protected Topological phases of matter to be discussed in Chapter 4 of the thesis.

In Chapter 3, we introduce Tensor Network (TN) States. We discuss its history and the motivation behind using this technique. We then systematically describe the two major families of TN States: the Matrix Product States (MPS) and the Projected Entangled Pair States (PEPS) which will then be used in the rest of the thesis. We discuss their properties and give some important examples. Details on how to compute the ground states of the many-body Hamiltonian and expectation values of operators with these techniques can be found in Appendix B and C. Other TN states are also discussed briefly.

In Chapter 4, we investigate two novel and exotic phases of matter in 1D. These are the Symmetry Protected Topological (SPT) and Symmetry Protected trivial (SPt) phases of matter. We give their definitions and explain how they are different from the conventional phases of matter. We then show that, using our technique, we can obtain several effective spin-1 SPT and SPt phases that have never been obtained before in a spin-2 chain numerically. For this, we study a spin-2 Heisenberg like model with bilinear, biquadratic, bicubic and biquartic interactions with additional uniaxial anisotropy and a staggered magnetic field. We show how conveniently TN algorithms can be used to distinguish the several spin-1 SPT(t) phases based on the irreducible representation of the symmetries protecting them. This chapter contains the first two publications of the author along with other details.

Chapter 5 is dedicated to studying Frustrated Quantum systems. These systems are very delicate due to the high quantum fluctuations and they often host a lot of exotic phases of matter in 2D. After defining and describing some properties of frustrated systems, we introduce one of the most difficult problems in the field of condensed matter physics: the Kagome Heisenberg Antiferromagnet (KHAF). We use infinite Projected Entangled Pair States (iPEPS) to study this model and show that our TN ansatz provides a very good approximation compared to other existing techniques based on the ground state energy of this model. As a generalization of this model, we further study the XXZ model with a field in the kagome lattice and study the 1/3 magnetization plateau as a function of the anisotropy term. We study this using a 6-site, 12-site iPEPS and a 9-site iPESS (infinite Projected Entangled Simplex States). This chapter contains the third publication of the author along with additional details.

In Chapter 6, we use the iPEPS to study open dissipative quantum systems in 2D. These are systems that are governed by the Lindbladian master equation. We use the

fact that any valid physical density operator can be vectorized and hence we can use the usual iTEBD (infinite Time Evolving Block Decimation) algorithm to study these systems. To probe the validity of our algorithm, we investigate the dissipative spin-1/2 Ising model in 2D in the thermodynamic limit. This is particularly interesting because of the controversies surrounding its phase diagram and also because of its experimental relevance using cold Rydberg atoms. We also investigate the spin-1/2 XYZ model to show that our algorithm is not limited to one specific model.

Finally, we review the whole thesis and make important conclusions concerning the different results. We also suggest possible future directions of our investigation.

Chapter 2

Entanglement and its consequences

Quantum entanglement, a phenomenon that has evoked the sharpest of reactions from the scientific community as well as the general population, was once described by Albert Einstein as "spooky action at a distance". It is the phenomenon by which the measurement of an entangled part affects the other part irrespective of the distance between them. The remark by Einstein reveals how uncomfortable he was with the concept of non-locality. But ironically, it was Einstein's discovery of the law of photo-electric effect [20] (earning him the Nobel Prize in 1921) that led to the revolution in quantum theory. Later on, Einstein along with Podolsky and Rosen formulated the famous EPR paradox [21]. In this paper, they argued that quantum theory is incomplete because they could not accept the concept of non-locality. They attributed the failure of quantum theory to some hidden variable. This led John Bell to derive his well-known inequality [22] which, when tested experimentally, would verify if there was indeed a hidden variable or quantum mechanics was complete. The experiment was finally performed and it was found that the Bell inequality was violated meaning that the local realist view cannot be correct [23, 24]. This proved that entanglement is real and quantum theory is complete. It is worth mentioning that recently, there has been a surge in the number of experiments filling the various loopholes that had existed associated with the previous Bell experiments [25, 26, 27, 28].

Not only is quantum theory correct, it was realized that the properties of quantum mechanics can be exploited to our advantage. It turns out that entanglement can be used as a resource after all! Understanding the concept of entanglement could have far reaching consequences in science. It has led to successfully conducting the first quantum teleportation experiments [29]. Quantum algorithms such as Shor's [30], Grover's search [31], etc have been shown to be much more superior than the classical algorithms we are used to for certain problems. We are currently racing to build the world's first quantum computer although there have been several claims so

far on its realization. For example, in 2011, D-Wave Systems announced the "first commercially available Quantum computer" called the D-Wave One, claiming a 128 qubit processor. Prior to their publication in Nature [32] explaining details of their mechanisms, there was a lot of criticism from the academics community on the quantum model of the machine [33, 34]. Besides D-Wave, there has also been a lot of work on this front by scientists at IBM, Google, Microsoft, etc. The 2012 Nobel Prize in Physics was awarded to David J. Wineland and Serge Haroche for their work on quantum optics paving the way for the development of quantum computers [35]. By the time this thesis was written, a quantum simulator with 51 qubits was announced by a group of US researchers [36]. Quantum cryptography is another emerging application exploiting the properties of quantum mechanics to perform cryptographic tasks such as quantum key distribution [37]. Besides its application in computing, quantum information has motivated new perspectives in studying properties of quantum many-body systems. In this thesis, we will see how we can use the properties of quantum entanglement for studying such systems using Tensor Network algorithms. Before we get into the details of this, let us familiarize ourselves with some basic properties of entanglement first.

2.1 Qubits

A bit is any 2-level system. The computers we see around us are based on classical bits. It means that a signal can be 'ON' or 'OFF', '0' or '1', etc. Unlike a classical bit, a quantum bit, also known as a *qubit*, can exist in any linear combination of the two states. A qubit is a unit of quantum information, a quantum mechanical two-level system. It could be the polarization of a photon (vertical or horizontal polarization) or the spin of a spin-1/2 particle (up or down).

The two states in which a qubit may be measured are known as basis states. The two computational basis states are usually written as $|0\rangle$ and $|1\rangle$. A generic state $|\psi\rangle$ of a qubit is a linear combination of these two states:

$$|\psi\rangle = \alpha|0\rangle + \beta|1\rangle, \tag{2.1}$$

where α and β are complex numbers representing the probability amplitudes of the two states respectively. By definition, they satisfy $|\alpha|^2 + |\beta|^2 = 1$. There is a very convenient and visual way of representing quantum states. It is known as the *Bloch sphere* representation. Bloch sphere is the geometrical representation of pure quantum

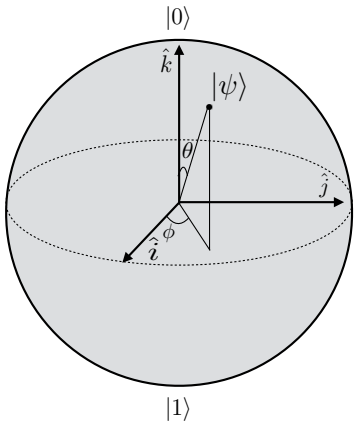

Figure 2.1: Bloch sphere representation of a pure quantum state $|\psi\rangle$.

states of a two-level system (qubit). In this representation, any generic pure state as in Eq. 2.1 can also be written as

$$|\psi\rangle = \cos\left(\frac{\theta}{2}\right)|0\rangle + e^{i\phi}\sin\left(\frac{\theta}{2}\right)|1\rangle, \tag{2.2}$$

where θ and ϕ are the polar and azimuthal angle of a point on the surface of the sphere. Thus, any physical state of a qubit can be parameterized in terms of two real parameters θ and ϕ. This results in the state $|\psi\rangle = |0\rangle$ when $\theta = 0$ and $|\psi\rangle = e^{i\phi}|1\rangle$ when $\theta = \pi$. Thus, the two orthogonal states lie opposite to each other in a Bloch sphere. This is shown in Fig. 2.1. The above discussion is only valid for the representation of pure states. If we want to represent mixed states, we need to use density matrices. A physical density matrix ρ has the following properties: (i) Trace$(\rho) = 1$ (ii) $\rho = \rho^\dagger$ (iii) positive semi definiteness i.e. no negative eigenvalues of ρ. The density matrix for a pure state $|\psi\rangle$ is simply the projector $|\psi\rangle\langle\psi|$ and for an ensemble of states $|\psi_j\rangle$ each prepared with probability p_j, it is

$$\rho = \sum_j p_j |\psi_j\rangle\langle\psi_j|. \tag{2.3}$$

The Bloch sphere can also be used to represent mixed states. They lie in the interior of the sphere.

2.2 Defining and quantifying entanglement

A pure state is said to be entangled if it cannot be expressed as a product state of the wave functions of the subsystems. To illustrate this with an example, consider two systems defined over the Hilbert spaces $\mathcal{H}_1$ and $\mathcal{H}_2$ such that

$$|\psi\rangle_1 \in \mathcal{H}_1, \;\; |\psi\rangle_2 \in \mathcal{H}_2. \tag{2.4}$$

A new composite system can be defined by the tensor product of these two Hilbert spaces:

$$\mathcal{H}_3 = \mathcal{H}_1 \otimes \mathcal{H}_2. \tag{2.5}$$

In terms of the basis states, we have

$$\begin{aligned} \{|0\rangle_1, |1\rangle_1\} &\in \mathcal{H}_1, \\ \{|0\rangle_2, |1\rangle_2\} &\in \mathcal{H}_2, \\ \{|0\rangle_1 \otimes |0\rangle_2, |0\rangle_1 \otimes |1\rangle_2, |1\rangle_1 \otimes |0\rangle_2, |1\rangle_1 \otimes |1\rangle_2\} &\in \mathcal{H}_3. \end{aligned} \tag{2.6}$$

We can now construct two possible states defined in $\mathcal{H}_3$ as follows:

$$\begin{aligned} |\psi\rangle &= \frac{1}{\sqrt{2}}(|0\rangle_1 \otimes |0\rangle_2 + |0\rangle_1 \otimes |1\rangle_2) \equiv \frac{1}{\sqrt{2}}(|0\rangle|0\rangle + |0\rangle|1\rangle), \\ |\phi\rangle &= \frac{1}{\sqrt{2}}(|0\rangle_1 \otimes |0\rangle_2 + |1\rangle_1 \otimes |1\rangle_2) \equiv \frac{1}{\sqrt{2}}(|0\rangle|0\rangle + |1\rangle|1\rangle). \end{aligned} \tag{2.7}$$

The prefactors are the normalization constants and the tensor product symbol has been omitted in the RHS of the above equations for simplicity.

From the definition of entanglement, we see that the wave function $|\phi\rangle$ is entangled because it cannot be expressed as a tensor product of the wave functions of the subsystems i.e.

$$|\phi\rangle \neq |\psi\rangle_1 \otimes |\psi\rangle_2 \Rightarrow \text{entangled}, \tag{2.8}$$

while the wave function $|\psi\rangle$ is separable because it can be decomposed into a tensor product of its subsystems i.e.

$$|\psi\rangle = |0\rangle_1 \otimes (|0\rangle_2 + |1\rangle_2) \Rightarrow \text{separable}. \tag{2.9}$$

Until now, we have only considered the case of pure states. However, most systems in nature and experiments are mixed since quantum systems cannot be isolated perfectly from the surroundings. For generic mixed states, we say that a given state ρ comprising of n parts is entangled if

$$\rho \neq \sum_k p_k \rho_1^k \otimes \rho_2^k \otimes \cdots \otimes \rho_n^k, \tag{2.10}$$

where p_k is the probability distribution function and ρ_n^k is the density matrix representing the nth state of the given ρ. Otherwise, it is separable. Checking the

separability of a quantum state can be done using a method known as *Schmidt decomposition* for pure states which will be discussed in the subsequent sections. For mixed states, such a decomposition does not exist and one has to use other concepts such as entanglement negativity, bound entanglement, PPT states [38, 39], etc. To quantify bipartite entanglement in pure states, we use *von Neumann entropy* which is an extension of the classical *Gibbs entropy*. As it measures entanglement in a bipartite system, it is also referred to as entanglement entropy. For a formal definition, consider a bipartite pure state $|\psi\rangle \in \mathcal{H}_A \otimes \mathcal{H}_B$. We can define the reduced density matrix of a subsystem by tracing out the other subsystem i.e

$$\rho_A = \mathrm{tr}_B(|\psi\rangle\langle\psi|), \;\; \rho_B = \mathrm{tr}_A(|\psi\rangle\langle\psi|). \tag{2.11}$$

The von Neumann entropy of such a partition is defined as

$$S(\rho_A) \equiv -\mathrm{tr}(\rho_A \ln \rho_A) = S(\rho_B). \tag{2.12}$$

By properties of a reduced density matrix, ρ_A can be expressed in terms of its eigenvalues as

$$\rho_A = \sum_{\alpha=1}^{\chi} \nu_\alpha |\alpha\rangle_A \langle\alpha|_A \tag{2.13}$$

where ν_α is the eigenvalue of the different basis and χ is the rank of the reduced density matrix ρ_A. Then, we see that the von Neumann entropy is

$$S(\rho_A) = -\sum_{\alpha=1}^{\chi} \nu_\alpha \ln \nu_\alpha. \tag{2.14}$$

We will show how we can compute the reduced density matrix of a subsystem from a bipartite state using a method known as Schmidt decomposition. The von Neumann entropy defined in this way can be used to study the phase diagram of a Hamiltonian. A product state will have a vanishing entropy while a maximally entangled state will have $S = \ln(\chi)$ where χ is the *Schmidt rank* of the system. This is the upper bound of the entanglement entropy. The von Neumann entropy is not a unique measure of bipartite entanglement. There are other quantities such as Renyi entropy [40], single copy entanglement [41, 42], etc. For multipartite systems, one needs to use other measures such as Geometric entanglement [43], 3-tangle [44] for tripartite systems, etc.

2.3 Schmidt Decomposition and SVD

The Schmidt decomposition can be used to obtain the reduced density matrix of a bipartite system which can then be used to obtain other quantities such as entanglement entropy, entanglement spectrum, etc. The theorem can be stated as follows.

Theorem: Given a pure state $|\psi\rangle$ consisting of two parts A and B, there exists orthonormal states $|i_A\rangle$ of system A and $|i_B\rangle$ of B such that

$$|\psi\rangle = \sum_{i}^{\chi} \lambda_i |i_A\rangle |i_B\rangle, \tag{2.15}$$

where λ_i's are positive real numbers satisfying $\sum_i \lambda_i^2 = 1$. They are known as *Schmidt coefficients* and are related to the eigenvalues of the reduced density matrix of the bipartition. It is a very useful quantity as we will explain it later. The number of non-zero Schmidt coefficients is the Schmidt rank. From Eq. 2.13, we see that the reduced density matrix of the subsystems are given by

$$\begin{aligned} \rho_A &= \mathrm{tr}_B(|\psi\rangle\langle\psi|) = \sum_i \lambda_i^2 |i_A\rangle\langle i_A|, \\ \rho_B &= \mathrm{tr}_A(|\psi\rangle\langle\psi|) = \sum_i \lambda_i^2 |i_B\rangle\langle i_B|. \end{aligned} \tag{2.16}$$

Thus, one can see that the Schmidt coefficients of a bipartition is the square root of the eigenvalues of the reduced density matrix of each of the subsystems and it does not depend on whether we trace out system A or B from the composite system. The vectors $|i_A\rangle$and$|i_B\rangle$ are called *Schmidt vectors*. Now, consider the states in Eq. 2.7, we see that

$$\begin{aligned} |\psi\rangle &: \chi = 1, \lambda_1 = 1 \\ |\phi\rangle &: \chi = 2, \lambda_1 = \lambda_2 = 1/\sqrt{2}. \end{aligned} \tag{2.17}$$

Thus, a state is separable iff the Schmidt rank of its decomposition $\chi = 1$. Hence, the Schmidt decomposition of a state is a very powerful tool to determine if a state is entangled or not simply by looking at its Schmidt rank and entropy. The proof of the Schmidt theorem can be done by using what is known as *Singular Value Decomposition (SVD)* in linear algebra. We provide it below.

Proof: Consider the case where the subsystems A and B have the state space of the same dimension. Let us assume $|j\rangle$ and $|k\rangle$ to be any fixed orthonormal bases for

systems A and B, respectively. Then $|\psi\rangle$ can be written as

$$|\psi\rangle = \sum_{jk} a_{jk}|j\rangle|k\rangle, \tag{2.18}$$

where a is a matrix of some complex numbers a_{jk}. By the definition of singular value decomposition, we can express any matrix a (real or complex) as $a = u * s * v$ where s is a diagonal matrix with non-negative elements, and u and v are unitary matrices. Therefore, we can write the above expression as

$$|\psi\rangle = \sum_{ijk} u_{ji} s_{ii} v_{ik}|j\rangle|k\rangle. \tag{2.19}$$

Now, we can define new vectors $|i_A\rangle \equiv \sum_j u_{ji}|j\rangle$, $|i_b\rangle \equiv \sum_k v_{ik}|k\rangle$, $\lambda_i \equiv s_{ii}$, we can express Eq. 2.19 as

$$|\psi\rangle = \sum_{i} \lambda_i |i_A\rangle|i_B\rangle, \tag{2.20}$$

which is in the Schmidt form. Besides its applications in quantifying entanglement properties, SVD allows us to make lower-ranked matrix approximations which is a very crucial step in our TN algorithms. This will be discussed in the later part of the thesis.

2.4 Entanglement in condensed matter

Before we conclude this chapter, it will be useful to introduce some concepts related to entanglement in the context of condensed matter systems. All these properties and results will be used in the later chapters when we study specific problems of interest.

2.4.1 Variational Principle

Theorem: Consider a Hamiltonian H (for simplicity, let us consider H with a discrete spectrum) and let E_0 be its lowest energy eigenvalue. Then the variational principle states that $\langle\Psi|H|\Psi\rangle \geq E_0 \ \forall \ |\Psi\rangle$.
Proof: We can write the eigenvalue equation:

$$\hat{H}|\psi_E\rangle = E|\psi_E\rangle \tag{2.21}$$

and from the spectral theorem we also know that

$$\sum_{E_i \in Spec(H)} |\psi_{E_i}\rangle\langle\psi_{E_i}| = \mathbb{1}. \tag{2.22}$$

Now,

$$\begin{aligned}\langle\Psi|H|\Psi\rangle &= \sum_{\lambda_i,\lambda_j\in Spec(H)} \langle\Psi|\psi_{\lambda_i}\rangle\langle\psi_{\lambda_i}|H|\psi_{\lambda_j}\rangle\langle\psi_{\lambda_j}|\Psi\rangle \\ &= \sum_{\lambda_i\in Spec(H)} \lambda_i|\langle\psi_{\lambda_i}|\Psi\rangle|^2 \\ &\geq \sum_{\lambda_i\in Spec(H)} E_0|\langle\psi_{\lambda_i}|\Psi\rangle|^2 = E_0\end{aligned} \tag{2.23}$$

As we see, E_0 represents a lower bound to the expectation value of H. We can use this principle to find an upper bound to the ground state energy by searching for the state $|\phi_\alpha\rangle$ out of a certain set of states that gives the infimum of the expectation value of H:

$$E_0 \leq \inf_\alpha \frac{\langle\phi_\alpha|H|\phi_\alpha\rangle}{\langle\phi_\alpha|\phi_\alpha\rangle}. \tag{2.24}$$

Thus, we can approximate the ground state of any Hamiltonian with the lowest expectation value of the ground state energy. The variational principle forms the basis of many numerical techniques used to study condensed matter systems including some TN methods such as DMRG [45, 46], variational PEPS [47], etc.

2.4.2 Quantum Phase Transitions

Quantum phase transition can simply be defined as the transition between different phases of matter at zero temperature when we vary a physical parameter such as the magnetic field. In order to illustrate it, let us take the example of the spin-1/2 Transverse Field Ising model in 1D. We will discuss the concepts of local order parameters, spontaneous symmetry breaking, how to detect phase transitions, etc for this model. The nearest-neighbor spin-1/2 Ising model in a transverse field in 1D is a relatively simple and well-understood problem in the field of condensed matter theory. This model is gapped, meaning that the correlation function of the ground state should decay exponentially. The Hamiltonian can be written as follows

$$H = -\sum_{\langle i,j\rangle} \sigma_i^z\sigma_j^z - h_x\sum_i \sigma_i^x, \tag{2.25}$$

where $\sigma_i^{x,z}$ are the familiar Pauli matrices residing on site i of our chain. The Pauli matrices are used to represent the quantum degrees of freedom. In the basis where σ^z is diagonal, they can be written in the following matrix form

$$\sigma^x = \begin{pmatrix}0 & 1\\ 1 & 0\end{pmatrix};\ \sigma^y = \begin{pmatrix}0 & -i\\ i & 0\end{pmatrix};\ \sigma^z = \begin{pmatrix}1 & 0\\ 0 & -1\end{pmatrix}. \tag{2.26}$$

As we can see, the operator σ^z has two eigenvalues $+1$ and -1. We can use the two eigenstates corresponding to these two eigenvalues as the possible configuration of an Ising spin i.e $|\uparrow\rangle$ and $|\downarrow\rangle$. The first term in the Hamiltonian in Eq. 2.25 represents interaction between different spins. We assume that the coefficient of this interaction strength is one. The symbol $\langle i, j\rangle$ means that we only consider nearest-neighbor spin interactions. The negative sign means that the spins prefer ferromagnetic alignment. The second term in the Hamiltonian corresponds to an external transverse magnetic field. Thus, we can see that the Hamiltonian describes ferromagnetic interaction along the σ^z direction along with an external field in σ^x direction.

The ground state of the Hamiltonian in Eq. 2.25 depends on the parameter h_x. So, let us consider two opposing limits i.e. when $h_x \ll 1$ and $h_x \gg 1$. When $h_x \ll 1$, the first term of the Hamiltonian dominates. For example, when $h_x = 0$, the ground state of the Hamiltonian is the state where all the spins are pointing either up or down due to the ferromagnetic nature of interaction i.e.

$$|\uparrow\rangle = \prod_i |\uparrow\rangle_i \text{ or } |\downarrow\rangle = \prod_i |\downarrow\rangle_i. \tag{2.27}$$

In the thermodynamic limit, a system always chooses one of the above two states as its ground state. This is known as the *spontaneous breaking* of the $\mathbb{Z}_2$ symmetry. Let us consider the other scenario in which $h_x \gg 1$. In this case, the second part of the Hamiltonian dominates. The ground state of the Hamiltonian in this case will be

$$|+\rangle = \prod_i |\rightarrow\rangle_i, \tag{2.28}$$

where $|\rightarrow\rangle_i = (|\uparrow\rangle_i + |\downarrow\rangle_i)/\sqrt{2}$ and $|\leftarrow\rangle_i = (|\uparrow\rangle_i - |\downarrow\rangle_i)/\sqrt{2}$ are the two eigenstates of σ^x with eigenvalues ± 1. This means that there is a critical value $h_x = h_{xc}$ at which the ground state changes qualitatively from one to the other. This is where the phase transition takes place and we call this h_{xc} the quantum critical point (QCP). It is possible to have more then one QCP for a Hamiltonian. But for the Ising model with a transverse field, there is only one QCP. The system is known to be gapless at QCP. This means that the energy gap separating the ground state and the first excited state is zero at this point. This is not true for a gapped system which lies on either side of the QCP in our model. In order to study the phase diagram of the model one needs to identify a *local order parameter*. It is a quantity that detects the spontaneous breaking of a certain symmetry of the model. A suitable local order parameter in our case could be the magnetization or the expectation value of the σ^z operator. This quantity should be non-zero for ground states when $h_x \ll 1$ and zero for the other case.

In the next chapter, we will investigate phase of matter exhibited by a spin-2 chain with a particular Hamiltonian that goes beyond the above discussions of symmetry broken phases. These are phases of matter that do not break any symmetries of the Hamiltonian and cannot be distinguished using the concept of local order parameters as we discussed before.

2.5 Summary

Quantum entanglement is a phenomenon in which the measurement of the quantum state of one particle affects the state of the other particle. This phenomenon has no classical counterpart. The properties of quantum entanglement can be exploited for applications in quantum teleportation, quantum computing, cryptography, developing new algorithms and studying many-body systems in nature.

A quantum state is usually represented using the Dirac notation for a pure state and a density matrix for a mixed state. Unlike a classical state, a quantum state can exist as a linear superposition of several states. Pure states are represented on the surface of a Bloch sphere while mixed states lie in the interior of the Bloch sphere. A pure state is said to be entangled if it cannot be expressed as the product of its subsystems. It is possible to quantify entanglement for pure states using the von Neumann entropy. We can use the Schmidt decomposition to compute the von Neumann entropy of a pure state. This decomposition is related to the singular value decomposition in linear algebra. For mixed states, the von Neumann entropy quantifies the 'mixedness' of the system and one needs to use other measures to quantify entanglement.

Entanglement has very important consequences in the context of quantum many-body systems. For example, the properties of entanglement can be used to identify quantum phase transitions in these systems where they are known to diverge at the critical point. To identify different phases, one can define some local order parameter that is zero in one phase and non-zero in the other. However, there are phases of matter that go beyond such classifications. They will be discussed in Chapter 4 of the thesis.

Chapter 3

Tensor Network States

Numerical techniques play a very important role in the study of quantum many-body systems. In the introductory part of the thesis, we have already mentioned some important numerical techniques. These techniques come with their own disadvantages. Exact Diagonalization (ED) [7] techniques can only study small systems far from the thermodynamic limit where the phase transition occurs. Mean Field Theory (MFT) [13] cannot incorporate the effect of quantum correlations in the system. Quantum Monte Carlo (QMC) [8] is a very well known technique in the field but it suffers from the infamous sign problem, therefore it is not so suitable for studying fermionic and frustrated systems. There are other techniques like Series Expansion (SE) [9] (which relies on perturbation theory calculations), Continuous Unitary Transformation (CUT) [10, 11] (which relies on the approximate solution of a system of infinitely-many coupled differential equations), and many more, each with their own limitations on either the system size or the kind of models they can study.

In this chapter, we will describe in detail one new technique: Tensor Network technique. TN techniques do not suffer from any of the problems mentioned. In fact, one of its advantages is its flexibility. It can be used for studying different kinds of systems both in one and two spatial dimensions for finite and infinite systems [48, 49, 50, 51, 52]. One can impose different boundary conditions [53, 54, 55] and even implement symmetries [56, 57]. It can also be used to study bosonic [58, 59], fermionic [60, 61, 62] or frustrated spin systems [63, 64, 65, 66]. TN algorithms can even be used to study dissipative open quantum systems and thermal states [67, 68]. Nowadays, TN theory is being used in other fields of study like AdS/CFT correspondence in quantum gravity [69, 70, 71, 72, 73, 74] and quantum chemistry [75, 76]. The most popular example of a TN algorithm is the Density Matrix Renormalization Group (DMRG) introduced by Steven White in 1992 [45, 46]. This technique has been one of the most successful algorithms to study gapped 1D systems. Besides DMRG,

there are many other algorithms available now to study both 1D and 2D quantum matter using TN such as the Time Evolving Block Decimation (TEBD) [77, 78, 79, 52], Projected Entangled Pair States (PEPS) [80, 50], Tensor Renormalization Group (TRG) [81], Multi-scaled Entanglement Renormalization Ansatz (MERA) [82], continuous Matrix Product States (cMPS) and continuous Tensor Networks [83, 84], Higher Order Tensor Renormalization Group (HOTRG) [85], etc.

Although TN techniques have various advantages and their popularity has increased drastically over the recent years, they are not free from limitations either. However, their drawbacks are not due to the type or size of systems but rather due to the amount and structure of entanglement present in the system. For example, it is known that MPS cannot reproduce the properties of critical or scale invariant systems where the correlation length is known to diverge [86, 87]. We will soon see that TN states are parameterized by something known as the 'bond dimension' which quantifies the amount of entanglement present in the system. However, in most of the cases we are interested in, it is possible to handle the issue of entanglement with a reasonable value of bond dimension within our computational limit. This is because of the following reasoning.

A quantum many-body system can be represented by specifying the coefficients of its wave function in a given basis. As we have discussed, the number of these coefficients scales exponentially with the number of particles and for a many-body system, it is impossible to access all the regions of the Hilbert space exactly when the number of particles involved is very large. However, it turns out that not all the regions of the Hilbert space are relevant for us. Most realistic materials can be approximated by a Hamiltonian that have only local interactions (finite range interactions). It is possible to show that the low energy states of local gapped Hamiltonian obey the so-called area law for the entanglement entropy in 1D [88, 89, 90]. In 2D, this is known to be true for any temperature T. For these states, the entanglement entropy scales with the boundary of the system and not with its volume (shown in Fig. 3.1(a)). Therefore, they can be efficiently represented by TNs because these states target the relevant corner of the Hilbert space satisfying the area law [91, 92][1]. Thus, instead of targeting the whole Hilbert space which is almost impossible and not even relevant for us, we can directly target the tiny corner of the Hilbert space with our TN states (shown in Fig. 3.1(b)). Not only this, it will become clearer in the next section of this chapter that not only is TN an efficient way of representing many-body quantum states, it

[1]There are states that satisfy the area law but cannot be approximated using Tensor Networks [93].

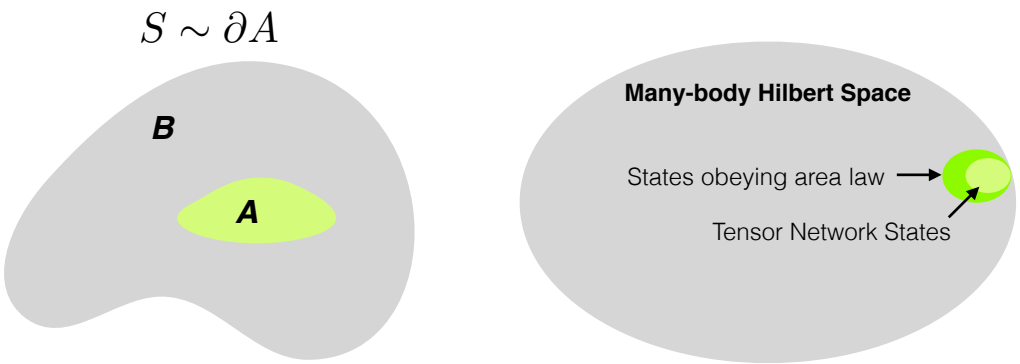

Figure 3.1: (a) Entanglement entropy between system A and B scales with the boundary (area law); (b) Many realistic materials obeying the area law in nature corresponds to a tiny corner in the Hilbert space.

also provides intuition about the structure of entanglement present in different parts of the system. The other good thing about TN is its simplicity. Rather then writing complicated equations involving lots of coefficients and indices, one can simply draw TN diagrams and perform calculations based on it. Therefore, it can be used a new language for condensed matter physics. This is illustrated in the next section of the chapter. We will also discuss some properties and examples of two important families of TN states: MPS and PEPS. Before we get into the details, let us provide some introduction and motivation to TN techniques in general. Our review of TNs in this chapter is based on [12]. More detailed and extended reviews can be found in [94, 95, 96, 97, 86, 87].

3.1 Tensor Network representation

A tensor is defined as a multi-dimensional array of complex numbers. The rank of a tensor is given by the number of its indices. Thus, a scalar is a rank-0 tensor (s), a vector a rank-1 tensor (v_i), a matrix a rank-2 tensor (m_{ij}) and so on. We can define a tensor with an arbitrary number of indices. We will now introduce the diagrammatic notation of tensors. We will represent a tensor with a ball and its index with a line coming out from it. Tensors of rank 0, 1 and 2 are shown in Fig. 3.2. We will assume that every index can assume $D(d)$ different values. This number could be the bond dimension or the physical dimension of our tensor network. We will explain this in more detail later on.

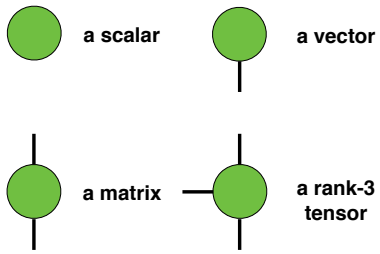

Figure 3.2: Diagrammatic notation of elementary tensors.

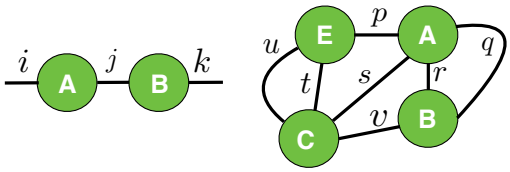

Figure 3.3: Diagrammatic notation of the tensor operations in Eq. 3.1 and Eq. 3.2.

Now, we will explain how we can make basic tensor operations using the notation we just introduced. An index contraction of the tensors is defined as the sum over all possible values of the repeated indices of a set of tensors. For example, the product of two matrices can be written as

$$C_{ik} = \sum_{j=1}^{D} A_{ij} B_{jk} \tag{3.1}$$

We can define more complicated tensor operations such as

$$F = \sum_{p,q,r,s,t,u,v=1}^{D} A_{pqrs} B_{qrv} C_{utsv} E_{utp} \tag{3.2}$$

where A, B, C, E are tensors having different number of indices. This is an example of a simple case where we assume that every leg has the same dimension D. In principle, this does not have to be the case. The result of this operation is just a scalar as there is no open index left. The common indices are the ones over which the tensors have been contracted. The above two operations can be denoted in the TN language as in Fig. 3.3. Thus, instead of writing complicated equations with large numbers of indices, it is much simpler to denote it in the TN language. TNs are like the Feynman diagrams in quantum field theory: they can be used to understand the

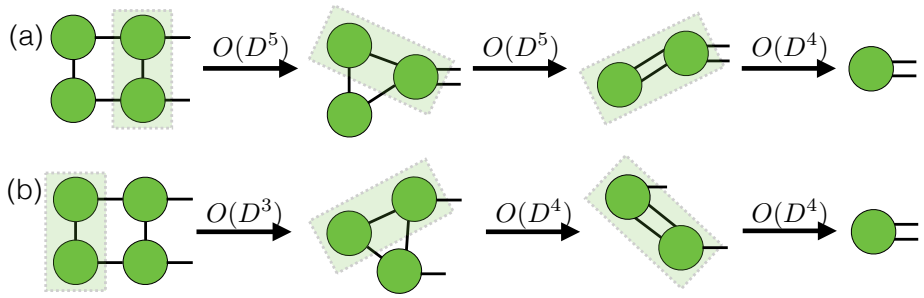

Figure 3.4: Following different orders of contraction for the same TN. The order of contraction in (b) is obviously more efficient.

structure and pattern of entanglement in a much more intuitive and visual manner. It is worth mentioning here that determining the optimum order of contraction is indeed a very important step in contracting the tensors. This is what determines the efficiency of a TN algorithm mostly. For example, let us consider the contraction of the TN in Fig. 3.4. It is a TN comprising of two tensors with two indices and two tensors with three indices. For simplicity, let us assume that each of the index has the same bond dimension D. In Fig. 3.4(a), we start the tensor network contraction from the two right-most tensors while in Fig. 3.4(b), we start the contraction with the two left-most tensors. We see that in the former case, the order of contraction is at most $O(D^5)$ while in the latter case, the order of contraction is at most $O(D^4)$ and hence a better option. Thus, one needs to be careful in choosing the optimum order of contraction. In the remaining part of the thesis, we will try to use TN diagrams as much as possible.

Let us now turn ourselves to the discussion of how one can represent quantum many-body states using TN language. Consider a quantum many-body system of N particles. Let us say that each particle can be described with p different states. Thus, we have a system of N p-level particles. For a spin-1/2 particle, the value of p is 2 as the spins can point either up or down. For a spin-1 particle, $p = 3$ and so on. The many-body wave function $|\psi\rangle$ for such a quantum many body system can be written in the following way

$$|\psi\rangle = \sum_{i_1 i_2 \ldots i_N} C_{i_1 i_2 \ldots i_N} |i_1\rangle \otimes |i_2\rangle \otimes \cdots |i_N\rangle, \tag{3.3}$$

once we choose an individual basis $|i_r\rangle$ for the states of each particle $r = 1, 2, \ldots N$. In the above equation, $C_{i_1 i_2 \ldots i_N}$ are p^N complex numbers (independent up to a normalization constant). The symbol $\otimes$ denotes the tensor product of the states of all

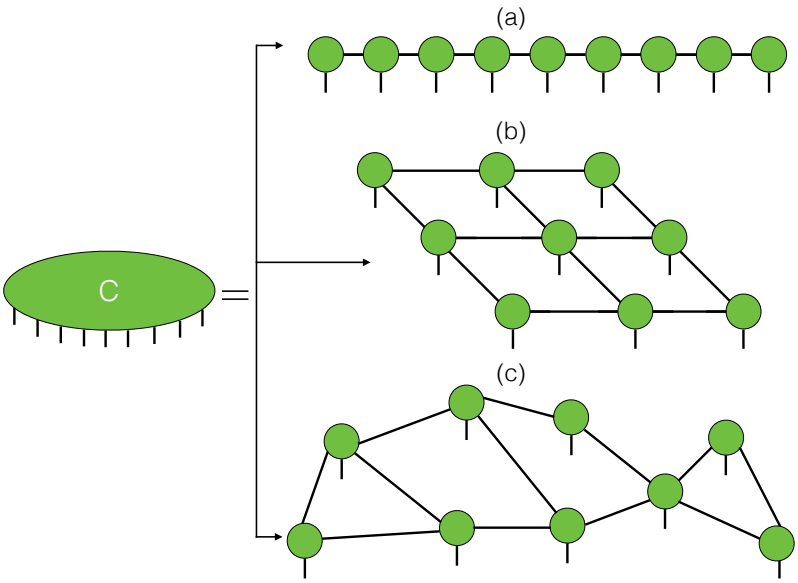

Figure 3.5: Decomposition of the big tensor C into a network of smaller ranked tensors: (a) a 1D TN known as Matrix Product States (MPS) with open boundary conditions; (b) a 2D TN known as Projected Entangled Pair States (PEPS) with open boundary conditions; (c) an arbitrary TN. It can be seen that all the TNs represent the wave function of a system with 9 particles.

the individual particles in the system and $i_r = 1, .., p$ for each of them. We can think of the coefficient $C_{i_1 i_2 ... i_N}$ as a tensor of N indices where each index i_r can take up to p different values. This tensor has p^N coefficients. This means that the number of parameters that are required to describe the wave function in the above equation is exponentially large in the system size. Each index in the tensor is called the physical index and the value of p is what we call the physical dimension of our TN.

One of the main aims of TN is to reduce the complexity in the representation of such quantum many-body states by replacing the 'big' tensor C with a TN of 'smaller' tensors. By 'big' and 'small', we refer to the rank of the respective tensors. Thus, we will decompose our huge tensor C into a network of smaller ranked tensors which are much easier to handle. This can be done in many different ways depending on the system we are studying. This is illustrated in Fig. 3.5. The TN in Fig. 3.5(a) is the well known Matrix Product States [98, 99] used to represent 1D phases of matter. The one in Fig. 3.5(b) is used to represent 2D phases of matter and are known as Projected Entangled Pair States [80, 50]. We will be using these two TN states to investigate our different models in the rest of the chapter. In Fig. 3.5, we see that a big tensor C can be decomposed into a network of smaller tensors. In doing so, we

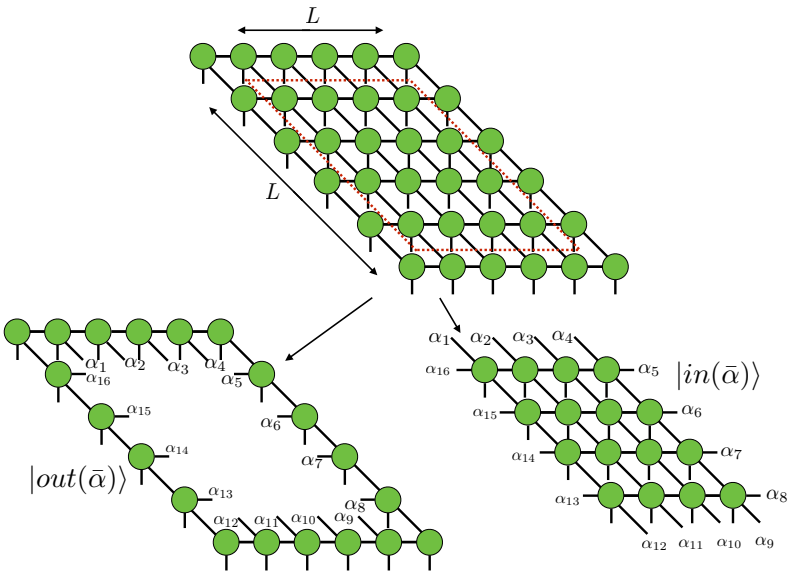

Figure 3.6: The given TN can be decomposed into the states $|in(\bar{\alpha})\rangle$ and $|out(\bar{\alpha})\rangle$ for a 4×4 block of a 6×6 PEPS.

notice that we have introduced extra degrees of freedom beside the physical index. These are the indices connecting the different tensors in the network. These indices have a very important physical meaning in the sense that they represent the structure of the many-body entanglement in the quantum state $|\psi\rangle$. They are known as bond indices or ancillary indices. And the maximum values these indices can take is known as the bond dimension of the TN, usually referred to as D or χ. We will use the symbol χ to represent the bond dimension of our TN in 1D systems and D for the same in 2D systems.

Let us now understand how the bond dimension of a TN is related to the entanglement contained in the system. Imagine we have a TN as shown in Fig. 3.6. As we have mentioned, this is a 2D TN known as Projected Entangled Pair States. Let us assume that all the indices have the same bond dimension D. For this state, let us estimate the entanglement entropy of a block of linear length L (shown in the figure). Let $\bar{\alpha} = \alpha_1\alpha_2...\alpha_{4L}$ be the combined index of all the TN indices across the boundary of the block. If each index can take D values, then the combined index of our block $\bar{\alpha}$ can take D^{4L} values. Now, let us express our wave function in the following way (ignoring the normalization).

$$|\psi\rangle = \sum_{\bar{\alpha}}^{D^{4L}} |in(\bar{\alpha})\rangle \otimes |out(\bar{\alpha})\rangle. \tag{3.4}$$

Tracing out the outer part of the wave function, we obtain the density matrix of the inner part as

$$\rho_{in} = \sum_{\bar{\alpha},\bar{\alpha}'} X_{\bar{\alpha},\bar{\alpha}'} |in(\bar{\alpha})\rangle\langle in(\bar{\alpha}')|, \tag{3.5}$$

where $X_{\bar{\alpha},\bar{\alpha}'} \equiv \langle out(\bar{\alpha}')|out(\bar{\alpha})\rangle$. The reduced density matrix of the inner part, as can be clearly seen, has a rank that is at most D^{4L}. This is true if we also consider the reduced density matrix of the outer part by tracing out the inner part. Now, we know that the entanglement entropy $S(L) = -\mathrm{tr}(\rho_{in} \log \rho_{in})$ is upper-bounded by the logarithm of the rank of ρ_{in}. Thus, finally we arrive at the following conclusion that

$$S(L) \leq 4L \log D, \tag{3.6}$$

which is an upper-bound version of the area law for entanglement entropy [88, 89, 90]. Also, we can see from the above equation that every broken bond index contribute at most $\log D$ to the total entanglement entropy. It is also very clear from the above equation that for a tensor network with $D = 1$, the entanglement entropy $S(L) = 0$, no matter the size of the block. This corresponds to no entanglement in the system; this type of ansatz is used for example in the mean field theory [2]. In our TN algorithms, one can put more entanglement in the system by simply increasing the value of D. The above result has a very important consequence in the TN theory. It means that the ground states of Hamiltonians with local interactions and obeying area law can be accurately approximated using TNs. In the next section, we describe in more detail the important properties and some examples of two important families of TN: Matrix Product States (MPS) and Projected Entangled Pair States (PEPS).

3.1.1 Matrix Product States

Matrix Product States (MPS) are the most popular examples of the TN family. They are very well-suited to study gapped 1D quantum many-body systems with local interactions using methods like Density Matrix Renormalization Group (DMRG) [45, 46], Time Evolving Block Decimation (TEBD) [77, 78, 79, 52], Power Wave Function Renormalization Group (PWFRG) [100], etc. MPS consists of one-dimensional array

[2] A Tensor Network with bond dimension 1 means that there is no entanglement in the system and therefore just a product state. This is equivalent to replacing the interactions by a mean local field created by the other particles at every site.

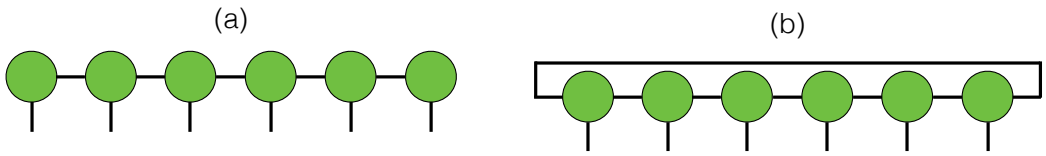

Figure 3.7: Matrix Product States with (a) Open boundary conditions (b) Periodic boundary conditions

of tensors. An example is shown in Fig. 3.5(a). Each tensor is used to represent one site in the many body system and the tensors are connected together by the bond indices each of which can take up to D different values. The open index corresponds to the physical index of each site which can take p different values e.g. $p = 2$ for a spin-1/2 particle. In the context of condensed matter theory, the boundary condition of the MPS is often important. In Fig. 3.7 we show two different MPS each with 6 sites (or tensors) with different boundary conditions. In principle, for such a finite MPS, all the tensors could be different. It is also possible to construct an infinite MPS by assuming some translational invariance over the 1D lattice. What we mean is that in the thermodynamic limit, a quantum state can be represented by an infinite MPS by choosing some unit cell that is repeated over the whole lattice. For example, for a unit cell of two tensors, our MPS will be made up of these two tensors repeated periodically. This is the kind of unit cell, we will be using in simulating our model in Chapter 4 of the thesis. It is worth reminding that MPS can represent the low energy states of most of the gapped local Hamiltonians in 1D with a very high accuracy with a reasonably finite value of D. This is because MPS satisfy the area law scaling of the entanglement entropy which is also satisfied by the ground states of gapped 1D local Hamiltonian. For sufficiently large bond dimensions of the MPS, one can cover other states beyond the area law and in principle the entire Hilbert space. But this is not so relevant in most of the cases. One limitation of the MPS is that it cannot reproduce the properties of critical or scale-invariant systems in 1D. This is because such systems are known to have diverging correlation length and it known that the correlation length of an MPS is always finite [86, 87]. Other important details such as the canonical form, computing the expectation values of the MPS, etc will be discussed in Chapter 4 and Appendix B of the thesis. Let us now discuss some

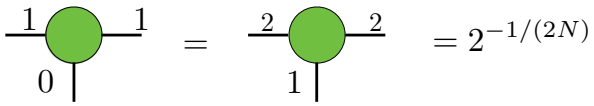

Figure 3.8: Non-zero components of the tensors in the GHZ state.

important and famous examples of 1D systems that can be represented accurately using MPS.

(a) GHZ state: The GHZ (Greenberger-Horne-Zeilinger) state [101] of N spin-1/2's can be written as

$$|GHZ\rangle = \frac{1}{\sqrt{2}}(|0\rangle^{\otimes N} + |1\rangle^{\otimes N}) \tag{3.7}$$

where $|0\rangle$ and $|1\rangle$ could be the eigenstates of the Pauli σ_z operator. Although there is no unique measure of multipartite entanglement, many measures define this state to be maximally entangled and is known to violate certain N-partite entanglement. Despite having non-trivial entanglement properties, such a state can be represented by an MPS with bond dimension $D = 2$ and periodic boundary conditions. The non-zero coefficients of the tensor in this case is shown in Fig. 3.8.

(b) AKLT model: The 1D AKLT (Affleck-Kennedy-Lieb-Tasaki) model is one of the few examples of a parent Hamiltonian whose ground state has an exact MPS representation [102, 103]. It is also the first analytical example of a model satisfying the Haldane conjecture [104, 105] which states that antiferromagnetic Heisenberg spin-chains with integer spins must have a finite excitation gap. This is very relevant in our case because it is an example of what is known as a 'Symmetry Protected Topological' phases of matter [106] which is what Chapter 4 of the thesis is about. The AKLT Hamiltonian of spin-1 chain is given by following

$$H = \sum_i \vec{S}_i \vec{S}_{i+1} + \frac{1}{3}(\vec{S}_i \vec{S}_{i+1})^2 \tag{3.8}$$

where $\vec{S}_i$ is the vector of spin-1 operators at site i where we assume an infinite size system. The ground state of this AKLT model has an exact MPS with bond dimension $D = 2$. This can be understood by considering a collection of spin-1/2 singlets, whose spins are paired and projected into spin-1 subspace. The construction of the MPS representing its ground state is shown in Fig. 3.9. The MPS tensors can always be

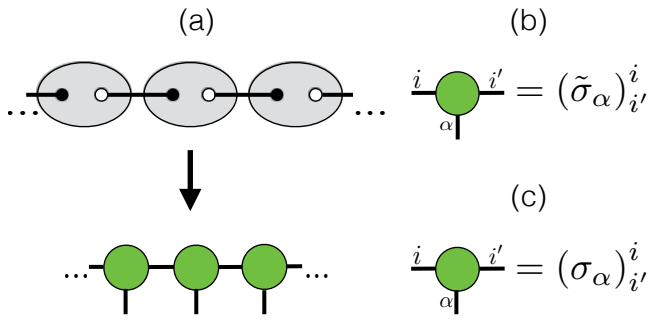

Figure 3.9: The AKLT ground state. (a) The spin-1/2 particles forming singlets $\frac{1}{\sqrt{2}}(|01\rangle - |10\rangle)$ are depicted by the black lines. They are projected by pairs into the spin-1 subspace depicted by the Grey blocks. (b) Non-zero components of the tensors of the infinite MPS with a one-site unit cell in terms of $\tilde{\sigma}_1 = \sqrt{2}\sigma_+$, $\tilde{\sigma}_2 = \sqrt{2}\sigma_-$ and $\tilde{\sigma}_3 = \sigma_z$. (c) There is a gauge degree of freedom such that one can use the usual spin-1/2 Pauli matrices for the coefficient of the tensors so that $\sigma_1 = \sigma_x$, $\sigma_2 = \sigma_y$ and $\sigma_3 = \sigma_z$.

written in terms of the three spin-1/2 Pauli matrices due to the gauge freedom. The details of the construction can be found in [87] for the interested readers.

3.1.2 Projected Entangled Pair States

Projected Entangled Pair States (PEPS) are the natural generalization of MPS to higher spatial dimensions. Here, we consider the case of 2D systems only. This TN ansatz forms the basis of Chapter 5 and 6 of this thesis. Besides, (infinite) PEPS, there are other algorithms to study 2D systems such as Tensor Renormalization Group (TRG) [81], Second Renormalization Group (SRG) [107], Higher Order Tensor Renormalization Group (HOTRG) [85] and other methods based on Corner Transfer Matrices (CTM) and Corner Tensors [51, 108, 109, 110].

As we have seen in Fig. 3.5(b), PEPS correspond to a 2D array of tensors. Like MPS, they can have open or periodic boundary conditions (Fig. 3.10 left and right). They also have 2 kinds of index, physical index p and bond index D. A PEPS could be defined on a square or lattices such as triangular, honeycomb, kagome, etc. MPS and PEPS share many other similar properties. Just like MPS, the tensors in a finite PEPS could all be different or in the case of the thermodynamic limit (the infinite case), one can could also assume certain translational invariance. In Chapter 5, we work with 2 and 4-site unit cell repeated periodically. Also, like the case of MPS, PEPS can represent any quantum state of the many-body Hilbert space if the bond

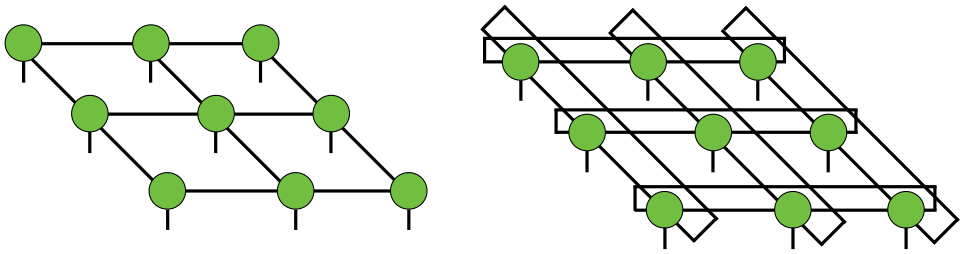

Figure 3.10: Projected Entangled Pair States with 9 sites with open and periodic boundary conditions (left and right).

dimension is sufficiently large. In order to cover the entire region of the Hilbert space, the bond dimension needs to be exceptionally large. In practice, it is known that the value of D required to represent a 2D state is very low compared to MPS. For example, a PEPS with bond dimension $D = 2$ can already handle critical states [111]. This is one of the differences with MPS that can handle only exponentially decaying correlation function. PEPS also satisfy the 2D area law scaling of the entanglement entropy. Another difference with MPS is that, unlike MPS where exact contraction of the tensors can be done efficiently, the exact contraction of the PEPS is considered a ♯P-Hard problem [112] in the language of computational complexity. This class of problems is related to counting the number of solutions to NP-Complete problems. This is a class of very difficult problems in computational complexity for which there is no classical (or even quantum) algorithm that can solve the problems in this class using polynomial resources in the size of the input. This means that exact contraction of two arbitrary PEPS of N sites will take $O(\exp(N))$ time. However, this is not so much of a serious problem as there are several numerical algorithms available to approximate the environment of a PEPS to a very large accuracy such as Corner Transfer Matrices (CTM) [51, 110], Higher Order Tensor Renormalization Group (HOTRG) [85], etc. Details on how to compute the environment, the ground state, the expectation value using the environment is described in Appendix C of the thesis. Now, let us discuss a few examples of 2D model that can be described using PEPS.

(a) Toric Code model: Perhaps the most important Hamiltonian with PEPS as a ground state, the Toric Code introduced by Kitaev [113] is a spin-1/2 model on the links of a 2D square lattice. This Hamiltonian can be written as:

$$H = -J_a \sum_s A_s - J_b \sum_p B_p \tag{3.9}$$

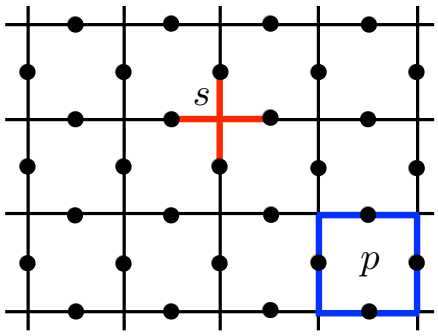

Figure 3.11: Toric code with star and plaquette operators.

where A_s and B_p are star and plaquette operators defined as

$$A_s = \prod_{\vec{r} \in s} \sigma_x^{[\vec{r}]}, \quad B_p = \prod_{\vec{r} \in p} \sigma_z^{[\vec{r}]} \tag{3.10}$$

i.e. A_s is the product of σ_x operators for the spins around a star and B_p is the product of σ_z operators for the spin around a plaquette. This is shown in Fig. 3.11. This is a very interesting model because it can be viewed as a lattice instance of a $\mathbb{Z}_2$ lattice gauge theory. It is also the simplest model known that exhibits topological order [2]. The ground state of the system is the $+1$ eigenstate of all the stabilizer operators (the set of star and plaquette operators $\{A_s\}$ and $\{B_p\}$). For an infinite 2D square lattice, the ground state is unique and can be written as

$$|\Psi_{TC}\rangle = \prod_s \frac{(I + A_s)}{2} \prod_p \frac{(I + B_p)}{2} |0\rangle^{\otimes N \to \infty} \tag{3.11}$$

Since the state $|0\rangle^{\otimes N \to \infty}$ is already a $+1$ eigenstate of the operators B_p for any plaquette p, we can write the above equation as

$$|\Psi_{TC}\rangle = \prod_s \frac{(I + A_s)}{2} |0\rangle^{\otimes N \to \infty} \tag{3.12}$$

Thus the ground state of this Toric Code Hamiltonian can be written as a PEPS with $D = 2$ and a 2-site unit cell with tensors A and B as defined in Fig. 3.12. Thus, even a PEPS with $D = 2$ can already handle topologically ordered states of matter. Besides the Toric Code, other models that can be written exactly as PEPS include the 2D Cluster State, 2D Resonating Valence Bond State, 2D AKLT model, etc.

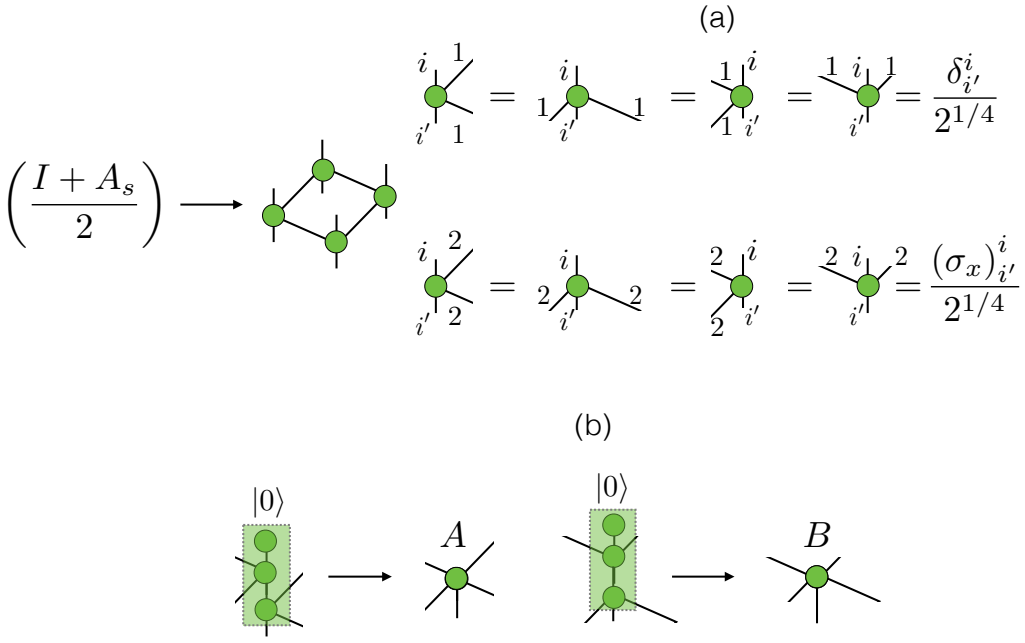

Figure 3.12: The Toric Code ground state can be written as a PEPS as defined in (a) and (b).

3.1.3 Other Tensor Network States

Besides MPS and PEPS, there are various other families of TN states such as continuous Matrix Product States (cMPS) and continuous Tensor Networks [83, 84], Tree Tensor Network (TTN) [114, 115, 116], Multi-scaled Entanglement Renormalization Ansatz (MERA) [82], Projected Entangled Simplex States (PESS) [117] and many more. The continuous Matrix Product States and continuous Tensor Network states can be used to describe systems beyond the quantum lattice models such as quantum field theories and continuum models. The Tree Tensor Network method is useful for simulating many-body quantum systems that has a tree-like structure like highly-branched polymers. The MERA is a class of quantum many-body states on a D-dimensional lattice that can be efficiently simulated with a classical computer. This technique is based on entanglement renormalization [118], a novel coarse-graining scheme for many-body quantum systems on a lattice. The Projected Entangled Simplex States is very similar to the PEPS we described but they extend the pair-correlation basis of PEPS to a simplex.

There are other important concepts in Tensor Network theory which we do not discuss in this thesis such as implementation of symmetries (this can improve the

efficiency of the algorithms to a very large extent), simulating fermionic systems (this can be done by introducing a fermionic swap gate which takes care of the sign problem), relationship between TNs and the holographic principle and the AdS/CFT correspondence. A more detailed review on some of these topics can be found in [119].

3.2 Summary

In this chapter, we have introduced a new kind of numerical technique for studying quantum many-body systems known as Tensor Network techniques. These techniques are based on writing the coefficients of the quantum many-body wave function in different arrangement of tensors which are multidimensional arrays of complex numbers. Unlike the other existing numerical techniques, the limitations of TN states are of different nature i.e. the amount of entanglement content in the system. TN diagrams provide a very simple and intuitive representation of quantum many-body states. So, instead of writing long and complicated equations, one can use these diagrams to represent our tensor operations. TN states, by construction, obey area law and therefore they are the ideal ansatz to study gapped phases of matter.

Two important families of TN that will be used in the rest of this thesis are the Matrix Product States and Projected Entangled Paired States. MPS are nothing but 1D array of tensors used to represent gapped quantum phases of matter in 1D. An MPS with bond dimension 2 can already represent highly non-trivial 1D systems such as the AKLT state. Similarly, PEPS can be used to represent 2D phases of matter including critical states. A PEPS with bond dimension 2 can handle topologically ordered states such as the Toric code. Besides MPS and PEPS, there are several other families of TN states which can be used to represent different kinds of systems and geometries efficiently.

Chapter 4

Symmetry Protected Topological and trivial phases

Haldane conjectured in 1983 that integer-spin Heisenberg antiferromagnet chains differ qualitatively from the half-integer case [104, 105]. He suggested that integer-spin chains should have a finite excitation gap with an exponential decay of the ground state correlation function while the half-integer case should be gapless with power-law decay of the ground state spin correlations. This came as a surprise to many people working in the field because his conjecture marked a huge deviation from what Bethe had found in 1931 [120]. The Bethe ansatz solution had predicted gapless excitations for the spin-1/2 chain and it was thought that other spin chains would have similar behavior. This issue remained in large for a while because of the non-rigorous nature of Haldane's argument involving topological terms in quantum-field theories. The numerical and experimental evidence of the existence of a finite gap for the case of $s = 1$ spin chain finally came [121, 122, 123, 124, 125, 126, 127, 128] and further developments made the situation more clear. For example, Lieb, Schultz and Mattis had already provided the rigorous proof of zero-gap in 1961 for spin $s = 1/2$ chain [129]. This proof was later extended for any arbitrary half-integer spin s but it was shown that it failed for integer spin s chain [130]. The Lieb-Schultz-Mattis theorem states that any half-integer spin chain with essentially any local Hamiltonian respecting the translational and rotational symmetry either has a zero gap or has degenerate ground states corresponding to spontaneously broken parity.

The Haldane phase of the spin-1 chain belongs to a new class of quantum matter known as the Symmetry Protected Topological phase, the definition of which falls beyond the conventional Landau symmetry breaking theory [131]. According to this theory, most conventional phases of matter and their phase transitions can be understood in terms of spontaneous breaking of a certain symmetry in the system.

Therefore, most conventional phases of matter can be described using a local order parameter which gives a non-zero value in one phase and zero in the other. We have discussed this kind of phase transition in Chapter 2 of this thesis by taking the example of the spin-1/2 transverse field Ising model. Symmetry Protected Topological (SPT) phases of matter, on the other hand, cannot be characterized using such local order parameters because there is no spontaneous breaking of symmetries taking place in these phases. They are 'short-range' entangled states meaning that they can be adiabatically connected to product states if one breaks the symmetries protecting them. The ground state of the AKLT model [102] which was also discussed in the previous section was the first model to satisfy the properties of the Haldane conjecture for a spin-1 system. SPT phases have exotic properties: for example the Haldane phase of the spin-1 chain has a hidden string order [132], two-fold degeneracy in the entanglement spectrum [133] of the reduced density matrix of one of the bipartition, etc, all of which are protected by symmetries. We will discuss these properties in more detail in the subsequent sections. Because of their exotic properties that remain robust against any perturbations that preserve the symmetries of the SPT, these phases of matter have been proposed as a resource in measurement-based quantum computing and other areas of quantum information in 1D and 2D [14, 15, 16].

It is worth mentioning that SPT phases are different from the so called 'Intrinsic Topological Order' which are also characterized by the absence of a local order parameter and are 'long-range' entangled. The difference between them is that while intrinsic topological order are robust against any local perturbations, SPT phases are robust only against local perturbations that preserve the symmetry. The term 'Topological Order' usually refers to the latter long-range entangled states. Such states usually have gapless boundary excitations which are protected by the topology of the system. An example would be the Fractional Quantum Hall States [134]. It is for this reason that Symmetry Protected Topological phases are also sometimes called as Symmetry Protected trivial phases because they can be adiabatically connected to a product state by some path that destroys the symmetries of the SPT. This is not to be confused with our definition of Symmetry Protected trivial phases which are also 'short-ranged' entangled states that are adiabatically connected to a product state but by a path that preserves the symmetries of the phase. It is easy to get tricked and confused by these nomenclatures. But we will stick to the latter nomenclature throughout this thesis. We will use the abbreviation SPT for Symmetry Protected Topological phases and SPt for Symmetry Protected trivial phases which are quite different from each other. Our nomenclature is consistent with the one in Ref. [135].

In 1992, Oshikawa conjectured the existence of an intermediate, effective spin-1 Haldane phase in higher spin-chains [136]. The search for such an effective spin-1 Haldane phase has received considerable interest since then and has only been found recently [137, 138, 139] for a spin-2 chain. In all these investigations, the focus was to find the well-known spin-1 Haldane phase. However, from the perspective of SPT phases, this is not the only spin-1 SPT phase that can be realized in a spin-2 chain [140] and so there must be more effective spin-1 'Haldane-like' phases. In this chapter, we investigate a spin-2 quantum chain with a Heisenberg-like bilinear, biquadratic, bicubic and biquartic nearest-neighbor interactions. We will show that it is possible to realize several other effective spin-1 SPT phases besides the Haldane phase corresponding to different projective representations of the $\mathbb{Z}_2 \times \mathbb{Z}_2 + T$ symmetry group where $\mathbb{Z}_2$ is some π rotation in the spin internal space and T is time reversal. Besides the spin-1 SPT phases, the model also exhibits an SO(5) Haldane phase which is also an SPT. We also study the phase transitions between the different SPT phases and describe them using Conformal Field Theory. We also study the extension of SPT phases to what is known as SPt or Symmetry Protected trivial phases. We do this by adding a staggered magnetic field to our existing spin-2 model. We will study its properties and discuss how it is different from the SPT phases.

4.1 SPT phases in spin-2 chain

Having discussed the origin and context of our problem, let us now jump directly into the investigation of Symmetry Protected Topological phases in a spin-2 quantum chain using our TN algorithms. It is worth mentioning here that our algorithms have been tested with several benchmarking results but we did not include them in this thesis. For this chapter, we use the infinite Matrix Product States with the iTEBD algorithm with a two-site unit cell. We go up to bond dimension $\chi = 120$ which proves sufficient for our purpose. This section in entirely based on the publication [141] by the author.

4.1.1 Model and symmetries

We investigate the following spin-2 chain

$$H = \sum_j \sum_{\gamma=1}^{4} J_\gamma (\vec{S}_j \cdot \vec{S}_{j+1})^\gamma + D \sum_j (S_j^z)^2 \tag{4.1}$$

in the thermodynamic limit. The first term involves the spin-spin Heisenberg interactions but with terms up to the fourth power. In the absence of the biquadratic, bicubic and biquartic spin-spin interaction, this model would be just the spin-2 Heisenberg model. The second term in the Hamiltonian is the uniaxial anisotropy term. In the limit of very large D, the ground state of the above Hamiltonian is described by a state in which all the sites are in the $|S^z = 0\rangle$ states. This model was studied in [139] for specific values of J_γ i.e. $J_1 = -11/6, J_2 = -31/180, J_3 = 11/90$ and $J_4 = 1/60$. For these specific values of J_γ's and when $D = 0$, the above Hamiltonian is an exactly solvable point with SO(5) symmetry and has an exact MPS as its ground state [142, 143]. To see this, we notice that the model in this limit can be rewritten as

$$H = 2\sum_j [P_2(j, j+1) + P_4(j, j+1)], \tag{4.2}$$

where $P_{S_T}(j, j+1)$ projects onto total spin-S_T states of neighboring sites j and $j+1$. To identify the SO(5) symmetry, we work in the standard S^z basis $|m\rangle$ ($m = \pm 2, \pm 1, 0$) and define the SO(5) Cartan generators

$$L^{12} = |2\rangle\langle 2| - |-2\rangle\langle -2| \tag{4.3}$$

$$L^{34} = |1\rangle\langle 1| - |-1\rangle\langle -1|. \tag{4.4}$$

By defining additionally

$$L^{15} = \frac{1}{\sqrt{2}}|2\rangle\langle 0| + |0\rangle\langle -2| + \text{H.c.} \tag{4.5}$$

$$L^{35} = \frac{1}{\sqrt{2}}|1\rangle\langle 0| + |0\rangle\langle -1| + \text{H.c.} \tag{4.6}$$

the SO(5) commutations relations

$$[L^{ab}, L^{cd}] = i(\delta_{ac}L^{bd} + \delta_{bd}L^{ac} - \delta_{ad}L^{bc} - \delta_{bc}L^{ad}) \tag{4.7}$$

fix the ten generators $L^{ab}(1 \le a < b \le 5)$. In the limit described previously, the Hamiltonian commutes with all the ten operators $\sum_j L_j^{ab}$, and therefore has SO(5) symmetry.

When $D > 0$ the $SO(5)$ symmetry is explicitly broken down to $U(1) \times U(1)$ [139]. This is easy to see if we rewrite the uniaxial anisotropy term using

$$(S^z)^2 = 4(L^{12})^2 + (L^{34})^2. \tag{4.8}$$

This implies that the operators $\sum_j L_j^{12}$ and $\sum_j L_j^{34}$ commute with the full Hamiltonian H as well as with each other, implying a $U(1) \times U(1)$ symmetry. Additionally, the

Hamiltonian in this regime has several point group symmetries including site-centered inversion I_s, time reversal T, as well as a set of $\mathbb{Z}_2$ symmetries corresponding to π rotations of the form

$$u^{ab} = e^{i\pi L^{ab}} \tag{4.9}$$

for all L^{ab}. The $\mathbb{Z}_2$ operators form a $(\mathbb{Z}_2 \times \mathbb{Z}_2)^2$ group, whose elements can be chosen as $\{\mathbb{1}, u^{12}\} \times \{\mathbb{1}, u^{15}\} \times \{\mathbb{1}, u^{34}\} \times \{\mathbb{1}, u^{12}\}$. As shown in [139], the model in this regime has two SPT phases: (i) one for low D, called the SO(5) Haldane phase, and (ii) one for intermediate D, corresponding to an intermediate spin-1 Haldane phase. The symmetries protecting these phases, as well as their different characterizations, were also discussed. In our case, we would like to investigate the above model for arbitrary values of J_γ. When we change the values of J_γ's from the $SO(5)$ symmetric values, the Hamiltonian has a $[U(1) \times \mathbb{Z}_2] + T$ symmetry where $U(1)$ corresponds to S_z conservation. We focus, however on the reduced discrete symmetry $\mathbb{Z}_2 \times \mathbb{Z}_2 + T$, so that in principle we could also add terms breaking the $U(1)$ symmetry down to $\mathbb{Z}_2$. Such a symmetry is known to protect up to 16 different possible SPT phases [140] of which four of them are typical of spin-1 chains. The 16 phases can be understood by defining four different *Symmetry Protected Topological Order* parameters, each of which can take two unique values $+1$ and -1 and symmetry operators acting on the bond index of the MPS [144]. We will discuss these in more detail shortly. We will first study the phase diagram of the above model for arbitrary values of the interaction strength J_γ and the anisotropy D; and therefore the symmetry relevant for us will be $(\mathbb{Z}_2 \times \mathbb{Z}_2) + T$. We focus on four two dimensional projections of the phase diagram obtained by fixing all the J_γ except one to the values mentioned above. Thus, we study the four two-dimensional planes $\langle J_1, D\rangle$, $\langle J_2, D\rangle$, $\langle J_3, D\rangle$ and $\langle J_4, D\rangle$ with the rest of interaction parameters fixed to the values mentioned for each case.

4.1.2 Identifying SPT phases

We now study our phase diagram using a number of properties which we discuss one by one.

Entanglement spectrum:

Let us consider the ground state of a 1D gapped system written as a translationally invariant MPS of length L ($L >> 1$). Such an MPS has the following form

$$|\psi\rangle = \sum_{i_j} \Gamma_{i_1} \lambda ... \Gamma_{i_L} \lambda |i_1 ... i_L\rangle, \tag{4.10}$$

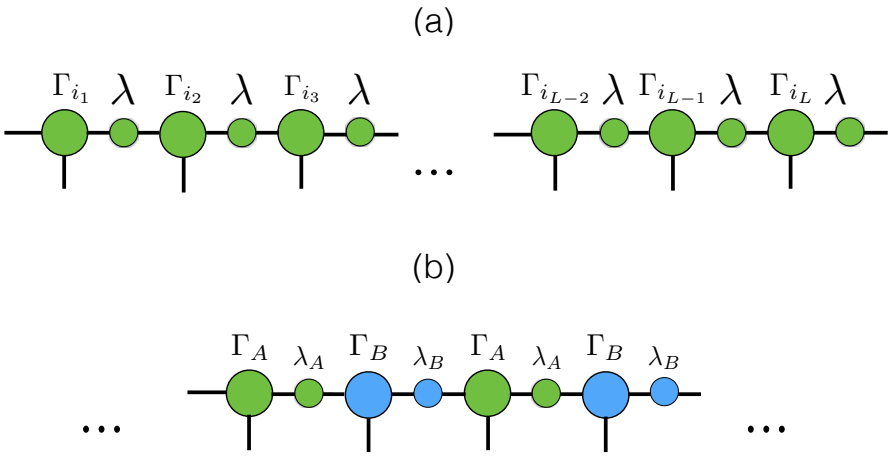

Figure 4.1: (a) A translationally invariant MPS of length L. All the tensors are identical here. (b) A translationally invariant MPS of infinite length and unit-cell of two sites. All the tensors appear alternately in this case.

where Γ_i are $\chi \times \chi$ matrices with χ being the bond dimension of the MPS and λ is a real diagonal matrix of dimension $\chi \times \chi$. The index i is the physical index corresponding to the spin states on each site. The pictorial representation is shown in Fig. 4.1(a). The matrices Γ and λ can be chose such that they satisfy the following form

$$\sum_i \Gamma_i \lambda^2 \Gamma_i^\dagger = \sum_i \Gamma_i^\dagger \lambda^2 \Gamma_i = \mathbb{1}, \tag{4.11}$$

they are said to be in the so-called canonical form of the MPS. The pictorial representation is shown in Fig. 4.2(a). Our iTEBD algorithm automatically ensures that our ground state MPS is already in this form. This canonical form automatically ensures that the following transfer matrix

$$T_{mm';nn'} = \sum_i \Gamma_{in}^m (\Gamma_{in'}^{m'})^* \lambda_n \lambda_{n'} \tag{4.12}$$

has a right eigenvector $\delta_{nn'}$ with eigenvalue $\lambda = 1$. One can similarly construct a transfer matrix with a similar left eigenvector and eigenvalue.

The wave function of the 1D chain described in Eq. 4.10 can be Schmidt decomposed at a certain bond as

$$|\psi\rangle = \sum_\alpha \lambda_\alpha |\alpha L\rangle |\alpha R\rangle, \tag{4.13}$$

where $|\alpha L\rangle$ and $|\alpha R\rangle$ ($\alpha = 1, ..., \chi$) are orthonormal basis vectors of the left and right partition respectively. In the limit $L \to \infty$, and under the canonical conditions

described above, the Schmidt eigenvalues λ_α are simply the entries of the matrix λ. The λ_α^2's are the eigenvalues of the reduced density matrix of this partition. They are known as *entanglement spectrum*. It was Haldane and Li [145] who proposed that the entanglement spectrum can be used as a finger print to identify topological order in general. The spin-1 Haldane phase, for example, is known to have a degeneracy of two in the entanglement spectrum of their ground state [133] while for the SO(5) Haldane phase, it was shown to have a four-fold degeneracy in the entanglement spectrum [139]. Such degeneracies produced by a virtual cut in the system mimics the physical edge states in these states and they are protected by the symmetries of the Hamiltonian i.e. they are there as long as the symmetries present are not broken. For example, the degeneracy pattern in the spin-1 Haldane phase is known to be protected by either the spatial inversion (bond-centered) or the time reversal symmetry. It is worth mentioning that from the numerical perspective, the iTEBD algorithm gives us this information for free while computing the ground state. Fig. 4.1(b) is a Matrix Product State of infinite size and with a unit cell of two sites. Thus, all the tensors in this case appear alternately. This TN is the one we use in our numerical simulations. Thus, the entanglement spectrum is merely the entries of the diagonal matrices λ_A or λ_B in our case. For an infinite MPS of two-site unit cell, the canonical form is depicted in the following sections in Fig. 4.8(a). Details on how to transform any generic MPS into the canonical form and its consequences can be found in Ref. [12].

For now, we want to understand the action of symmetries on our MPS and how it leads to non-trivial degeneracy of the entanglement spectrum. If our wave function $|\psi\rangle$ is invariant under a local symmetry $\Sigma_{ii'}$ (a unitary matrix acting on the spin basis), then the action of this symmetry on the Γ matrices can be written as [146]

$$\sum_{i'} \Sigma_{ii'} \Gamma_{i'} = e^{i\theta_\Sigma} \cdot U_\Sigma^\dagger \Gamma_i U_\Sigma, \tag{4.14}$$

where U_Σ are unitary matrices acting on the bond indices of the MPS that commute with the λ matrices and forms a projective representation of the symmetry of the wave function. $e^{i\theta_\Sigma}$ is a phase factor. This action is illustrated in Fig. 4.2(b). For the case of spatial inversion, the above transformation can be written as

$$\Gamma_i^T = e^{i\theta_I} \cdot U_I^\dagger \Gamma_i U_I \tag{4.15}$$

where U_I is a unitary matrix and $e^{i\theta_I}$ is the phase factor corresponding to the inversion symmetry. Applying this transformation one more time to the above, we get

$$\begin{aligned} \Gamma_i &= e^{2i\theta_I} \cdot (U_I U_I^*)^\dagger \Gamma_i U_I U_I^* \\ \implies \sum_i \Gamma_i^\dagger \lambda U_I U_I^* \lambda \Gamma_i &= e^{2i\theta_I} \cdot U_I U_I^*, \end{aligned} \tag{4.16}$$

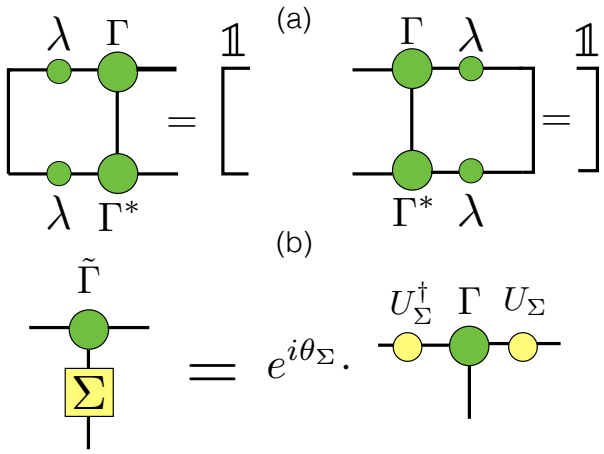

Figure 4.2: (a) Left and right canonical condition of a translationally invariant iMPS. (b) Action of a symmetry operator on a translationally invariant iMPS.

where we have used the properties of the canonical condition of the Γ and λ matrices. Therefore, $U_I U_I^*$ is an eigenvector of the transfer matrix T with eigenvalue $e^{2i\theta_I}$. But we know that the eigenvalue of T is $\lambda = 1$ and this value is unique. So, $e^{2i\theta_I} = 1$ and we can write $U_I U_I^* = e^{i\phi_I}\mathbb{1}$ where ϕ_I is a phase. Hence, it follows that $U_I^T = U_I e^{-i\phi_I}$. Repeating this relation one more time, we get $e^{-2i\phi_I} = 1$ i.e. $\phi_I = 0$ or π. This fact that ϕ_I can only take discrete values (0 or π) leads to phase transition between different states which cannot be characterized using the Landau paradigm. When $\phi_I = \pi$, then U_I is an antisymmetric matrix which means that all its eigenvalues are at least doubly degenerate which is what we see in the entanglement spectrum of the Haldane phase protected by this symmetry. Our argument follows from Ref. [133].

One can show the same for time reversal symmetry. For the SO(5) Haldane phase with quadruple degeneracy, it is beyond the scope of these two symmetries and one needs to consider the $(\mathbb{Z}_2 \times \mathbb{Z}_2)^2$ symmetry which allows a non-trivial four-dimensional irreducible projective representation. The details of this argumentation can be found in Ref. [139]. The non-trivial degeneracy in the entanglement spectrum for the two SPT phases is shown in Fig. 4.3. The Large-D phase has no degeneracy in the entanglement spectrum of its ground state MPS. This is a trivial state and is the ground state of our Hamiltonian (Eq. 4.1) when $D \to \infty$. We can see that in the SO(5) Haldane phase, the Schmidt coefficients are always grouped into clusters of four with the same magnitude while in the case of Intermediate Haldane phase, they are grouped into clusters of two with the same magnitude. However, there is no such pattern for the Large-D phase. We can now use this criteria of the degeneracy of

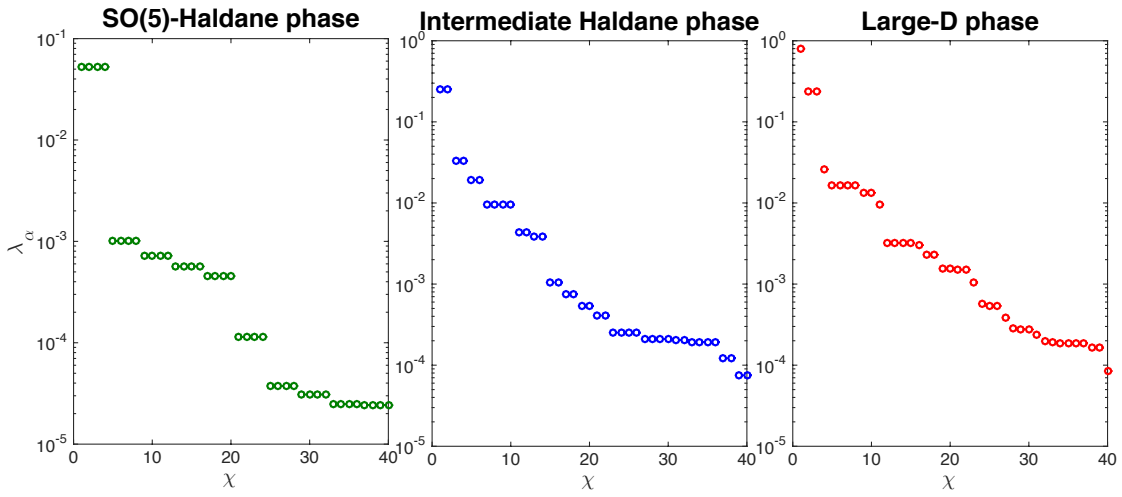

Figure 4.3: Values of the Schmidt coefficients for the SO(5) Haldane phase (left), Intermediate Haldane phase (middle) and the Large-D phase (right) for an MPS with bond dimension $\chi = 40$. We can easily see that for the SO(5) Haldane phase, there is a four-fold degeneracy in the entanglement spectrum, the IH phase has two-fold degeneracy and the Large-D phase has no degeneracy.

the entanglement spectrum to study the phase diagram of our model with arbitrary values of J_γ's and D by projecting it into four two-dimensional planes. This is shown in Fig. 4.4. Thus, we identify three different phases based on the entanglement spectrum. We find a small green region in all the four planes with degeneracy four in the entanglement spectrum. This is the SO(5) Haldane phase region. The blue region has degeneracy two in the entanglement spectrum. This is the Intermediate or spin-1 Haldane phase region and we see that this region is very large in all the four planes. The other phase is the one shown in Grey region. It does not exhibit any degeneracy in the entanglement spectrum and hence is a trivial phase. In order to confirm these three phases, we will compute something known as the 'String Order Parameter'.

String Order Parameter

It is known that the ground state of the spin-1 Haldane phase has a perfectly hidden antiferromagnetic order [132]. It means that in the S_z basis, the $|+1\rangle$ and $|-1\rangle$ states appear alternately with arbitrary number of $|0\rangle$s in between. An example of an allowed configuration would then look like: $|+100-10+1-10+1000-10+1-1+1-100+1-10000000000+100-1+1-1\rangle$. On removing the zeros in between, one would get $|+1-1+1-1+1-1+1-1+1-1+1-1+1-1+1-1\rangle$, an

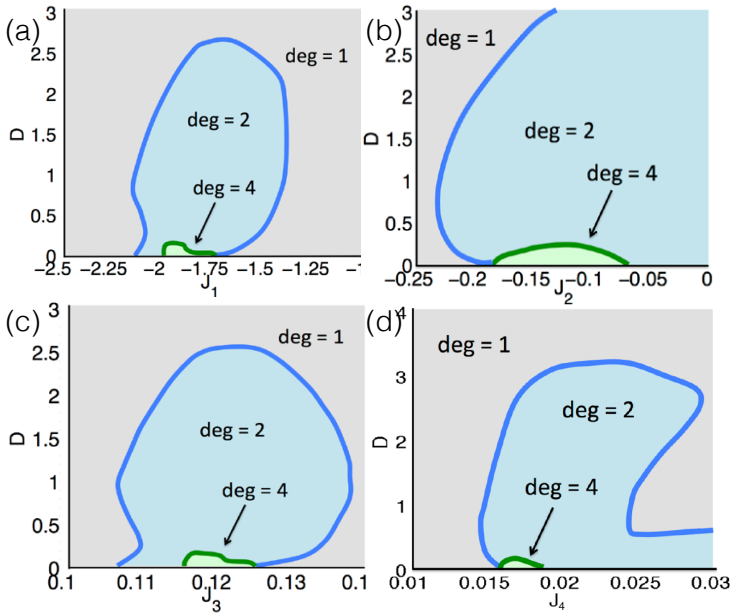

Figure 4.4: Degeneracy in the entanglement spectrum of the reduced density matrix of a bipartition for the four two-dimensional planes. In each $\langle J_\gamma, D\rangle$ plane, the rest of the J_γ's are fixed to their SO(5) symmetric point. The green region in each plane with degeneracy four is the SO(5) Haldane phase, the blue region with degeneracy two is the spin-1 SPT phase and the Grey region with degeneracy one is a trivial phase.

Phase	$\mathcal{O}^{12}$	$\mathcal{O}^{34}$
SO(5) Haldane	$\neq 0$	$\neq 0$
Intermediate Haldane	$= 0$	$\neq 0$
Large D	$= 0$	$= 0$

Table 4.1: Distinguishing the SO(5) Haldane phase from the Intermediate Haldane phase using the two String Order Parameters defined in Eq. 4.18.

antiferromagnetic state. Such a hidden AF order can be measured by the so-called 'String Order Parameter' which gives a non-zero value for the Haldane phase and zero for the trivial phase. It is defined as

$$\mathcal{O}^{\alpha}_{str} = \lim_{|k-j|\to\infty} \left\langle S^{\alpha}_{j} \prod_{l=j+1}^{k-1} \exp(i\pi S^{\alpha}_{l}) S^{\alpha}_{k} \right\rangle, \tag{4.17}$$

where S^{α}_{i}, for example, could be the spin-1 S^{z} operator at site i. For the case of our spin-2 model, we can define two new SOPs (String Order Parameters) as follows

$$\begin{aligned} \mathcal{O}^{12} &= \lim_{|k-j|\to\infty} \left\langle L^{12}_{j} \prod_{l=j+1}^{k-1} \exp(i\pi L^{12}_{l}) L^{12}_{k} \right\rangle \\ \mathcal{O}^{34} &= \lim_{|k-j|\to\infty} \left\langle L^{34}_{j} \prod_{l=j+1}^{k-1} \exp(i\pi L^{34}_{l}) L^{34}_{k} \right\rangle \end{aligned} \tag{4.18}$$

where L^{12} and L^{34} were previously defined as the Cartan generators of the SO(5) group in the S^{z} basis written as $L^{12} = |2\rangle\langle 2| - |-2\rangle\langle -2|$ and $L^{34} = |1\rangle\langle 1| - |-1\rangle\langle -1|$. It was shown in Ref. [139] that these two SOPs can be used to distinguish the spin-1 SPT (or the Intermediate Haldane) phase from the SO(5) Haldane phase. This can be understood from Table 4.1. In order to understand intuitively how the SOPs change for different phases, let us consider the case for which $D = 0$ and the J_{γ}'s are fixed to their SO(5) symmetric values. In this case, the MPS ground state is known to have a perfect hidden string order in the S^{z} basis i.e. $|2\rangle$ and $|-2\rangle$ states appear alternately in the configuration of our MPS if we ignore the $|0\rangle$ and $|\pm 1\rangle$ states in between. Similarly, if we remove the $|0\rangle$ and $|\pm 2\rangle$ states in between, we will find that $|1\rangle$ and $|-1\rangle$ states also appear alternately. Therefore, this hidden string order of the $|\pm 1\rangle$ and $|\pm 2\rangle$ states is reflected in the non-zero value of $\mathcal{O}^{12}$ and $\mathcal{O}^{34}$ as seen in the table. The Intermediate Haldane phase (or the spin-1 SPT) is found when we increase the value of D but not too much. This is why this phase is also known as the Intermediate D phase. In this case, what happens is that on

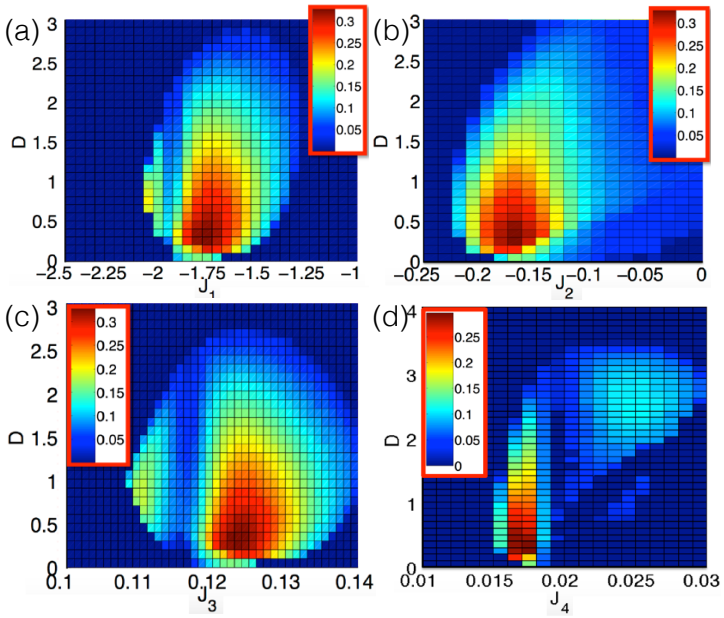

Figure 4.5: Nonlocal String Order Parameter $\mathcal{O}^{34}$ for all the four two-dimensional planes. This quantity is non-zero both for SO(5) Haldane phase and Intermediate Haldane phase and zero for the other regions.

increasing D, the uniaxial anisotropy starts suppressing both the $|\pm 2\rangle$ and $|\pm 1\rangle$ states but with greater effect on the former one. Therefore, the string order for the $|\pm 2\rangle$ states is destroyed while the string order for $|\pm 1\rangle$ states stay. Hence, this phase has a non-zero value for $\mathcal{O}^{34}$ and a zero value for $\mathcal{O}^{12}$. This is because the L^{12} and L^{34} operator act on the $|\pm 2\rangle$ and $|\pm 1\rangle$ states respectively. In the third case, when D is really large, we expect it to destroy the string order of both the $|\pm 1\rangle$ and $|\pm 2\rangle$ states completely. Therefore, both the string orders $\mathcal{O}^{12}$ and $\mathcal{O}^{34}$ is zero in this case. The numerical support of our argument is provided in Fig. 4.5 and Fig. 4.6. In Fig. 4.5, we compute the value of the string order parameter $\mathcal{O}^{34}$ for all the points in the four different planes $\langle J_1, D\rangle$, $\langle J_2, D\rangle$, $\langle J_3, D\rangle$ and $\langle J_4, D\rangle$. We can see that this quantity is non-zero for both the SO(5) region and the Intermediate Haldane phase region. In order to distinguish between the two, we compute the SOP $\mathcal{O}^{12}$ for all the points in the different planes. We only show it for the $\langle J_1, D\rangle$ and $\langle J_3, D\rangle$ plane here in Fig. 4.6. It is worth mentioning that in Fig. 4.5, the SOP $\mathcal{O}^{34}$ seem to disappear in the middle of the IH region in (a), (c) and (d). This led us to suspect that there could indeed be a phase transition in these regions although there is no such hint from the plot of the entanglement spectrum in Fig. 4.4. If there is indeed a phase transition between different IH regions, it is beyond the scope of the entanglement

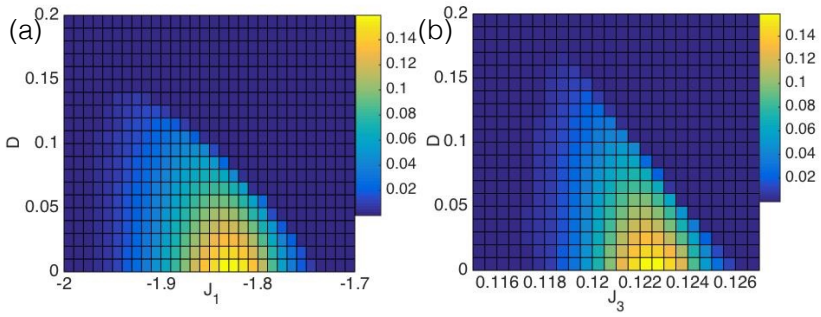

Figure 4.6: Nonlocal String Order Parameter $\mathcal{O}^{12}$ for the two planes $\langle J_1, D\rangle$ and $\langle J_3, D\rangle$ plane. This quantity is non-zero for the SO(5) Haldane phase and zero for the other phases.

spectrum or the SOPs to distinguish them. One needs to have a detailed study of the projective representation of the symmetries protecting the IH phase. But before we take a look at these quantities, we would like to confirm that there is indeed a phase transition from what we find based on the behavior of the entanglement entropy in these regions. This is discussed in the next section.

Entanglement entropy

We have already discussed in detail the concept of entanglement entropy (also known as von Neumann entropy) in Chapter 2 of the thesis. Let us revise. Given a bipartite pure state $|\psi\rangle \in \mathcal{H}_A \otimes \mathcal{H}_B$, one can express the wave function as follows using the Schmidt theorem

$$|\psi\rangle = \sum_i^{\chi} \lambda_i |i_A\rangle |i_B\rangle, \tag{4.19}$$

where $|i_A\rangle$ and $|i_B\rangle$ are some orthonormal states of system A and B and λ_i are positive real numbers satisfying $\sum_i \lambda_i^2 = 1$ known as Schmidt coefficients and χ is the Schmidt rank. As we know, the Schmidt coefficients are related to the eigenvalues of the reduced density matrix of the bipartition. Let us see how. Our wave function in the above equation can be written in the form of a density matrix as

$$\rho = \sum_i^{\chi} \lambda_i^2 |i_A\rangle |i_B\rangle\langle i_B| \langle i_A|. \tag{4.20}$$

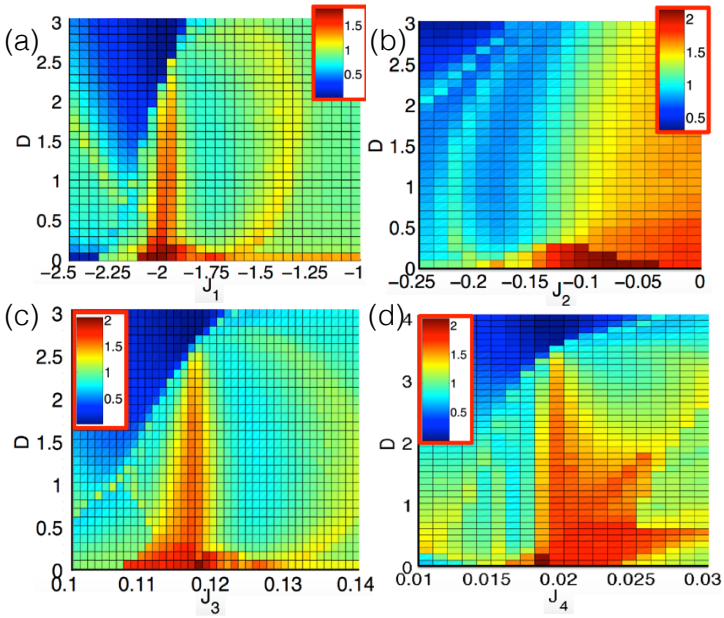

Figure 4.7: Entanglement entropy of half an infinite chain for the four two-dimensional planes.

In order to get the reduced density matrix of the subsystems, one needs to trace out the other subsystem. Doing this, we get the density matrix of the two subsystems as

$$\begin{aligned} \rho_A &= \mathrm{tr}_B(|\psi_{AB}\rangle\langle\psi_{AB}|) = \sum_i \lambda_i^2 |i_A\rangle\langle i_A| \\ \rho_B &= \mathrm{tr}_A(|\psi_{AB}\rangle\langle\psi_{AB}|) = \sum_i \lambda_i^2 |i_B\rangle\langle i_B| \end{aligned} \tag{4.21}$$

i.e. the eigenvalues of the reduced density matrices of the bipartition is equal to the squares of the Schmidt coefficients of the bipartition. Therefore, from Eq. 2.14, one can write the von Neumann entropy as

$$S(\rho_A) = S(\rho_B) = -\sum_{i=1}^{\chi} \lambda_i^2 \ln \lambda_i^2. \tag{4.22}$$

These λ_i's are very easy to extract from our numerical simulations. They are nothing but the entries of the diagonal matrices λ_A or λ_B in Fig. 4.1 (b). The form of this TN in this figure is automatically ensured when we compute the ground state of our Hamiltonian using the iTEBD algorithm and by the choice of our number of unit cells (two in this case). We then plot this entanglement entropy for the same parameter regime as in Fig. 4.4 for all the four planes. This is shown in Fig. 4.7. From this figure, one can get an idea of where the entropy diverges and therefore locate the critical

region in the phase diagrams. We can see that the location of the phase transition agrees very well with the plots in Fig. 4.5 where the non-local string order parameter seems to vanish exactly at these regions. The nature of these phase transitions will be described shortly in the following sections.

Projective representation of $\mathbb{Z}_2 \times \mathbb{Z}_2 + T$ symmetry

The confirmation of the existence of phase transitions in the middle of the Intermediate Haldane (IH) phase region in $\langle J_1, D\rangle$, $\langle J_3, D\rangle$ and $\langle J_4, D\rangle$ plane automatically ensures that the IH phases lying on either side of the phase transition are indeed different. The distinction between these different IH phases cannot be done using the entanglement spectrum or the SOPs as they have the same degeneracy and non-zero value of $\mathcal{O}^{34}$. These phases are, however, actually effective spin-1 SPT phases having different projective representations of the $\mathbb{Z}_2 \times \mathbb{Z}_2 + T$ symmetry group where $\mathbb{Z}_2$ is some π rotation in the spin internal space and T is the time reversal. Let us try to understand them in more detail.

In Ref. [140] a complete classification of all the SPT phases protected by $(\mathbb{Z}_2 \times \mathbb{Z}_2) + T$ symmetry is provided, based on the grounds of group-theory properties. This classification is summarized in Table I of that paper, where it is seen that there are a total of 16 different phases, and which introduces the notation T_0, T_x, T_y and T_z used in this paper for the typical spin-1 SPT phases. However, it is possible to understand in a much simpler way the 16 phases in spin chains with $(\mathbb{Z}_2 \times \mathbb{Z}_2) + T$ symmetry. This goes as follows: in MPS language, we have a set of (projective) symmetry operators R_x, R_z and R_t which are actually the matrix representations of π rotations around the x axis, π rotations around the z axis, time reversal T acting on the bond indices. Without loss of generality, we choose $R_x^2 = R_z^2 = \mathbb{1}$ (if $R_x^2 = -\mathbb{1}$, it is always possible to redefine R_x and R_z by multiplying a factor i, so $R_x^2 = \mathbb{1}$ is just a gauge choice). The nontrivial sign $\omega = \pm 1$ denotes the commutation relation between R_x and R_z, which cannot be gauged away. This means, $R_x R_z = \omega R_z R_x$. Together with the sign $\beta = \pm 1$ defined from $R_t^2 = \beta \mathbb{1}$, there are in total four choices:(1) $\omega = 1, \beta = 1$, (2) $\omega = 1, \beta = -1$ (3) $\omega = -1, \beta = 1$ and (4) $\omega = -1, \beta = -1$. For each of the above four choices, there are still four possibilities:(a) $[R_z, R_t] = 0$ and $[R_x, R_t] = 0$, (b) $[R_z, R_t] = 0$ and $\{R_x, R_t\} = 0$, (c) $\{R_z, R_t\} = 0$ and $[R_x, R_t] = 0$ and (d) $\{R_z, R_t\} = 0$ and $\{R_x, R_t\} = 0$. Other commutators are all fixed by the above relations. The above four choices correspond to the index γ in Table I of Ref. [140], and we label them by the values of signs $\mu = \pm 1$ and $\nu = \pm 1$ defined respectively from $R_x R_t = \mu R_t R_x$ and $R_z R_t = \nu R_t R_z$. Thus, there are in total $4 \times 4 = 16$ phases (1a, 1b, 1c, 1d, 2a,

2b,..., 4d), which can be labeled uniquely by the four signs $(\beta, \omega, \mu, \nu)$. For the sake of clarity, let us rewrite the four different relations from which these SPTO parameters can be extracted

$$R_t^2 = \beta \mathbb{1} \tag{4.23}$$
$$R_x R_z = \omega R_z R_x \tag{4.24}$$
$$R_x R_t = \mu R_t R_x \tag{4.25}$$
$$R_z R_t = \nu R_t R_z. \tag{4.26}$$

Let us mention that in their paper, operators R_x, R_z and R_t do not correspond to the gauge that we are using here, where $R_x^2 = R_z^2 = \mathbb{1}$. To recover the above results, one has to remove a factor "i" for R_x and R_z in Table I of that reference, so that they square to $\mathbb{1}$. Then one can check that the commutation relations among R_x,R_z and R_t just correspond to the above 16 cases. Before we start classifying the different phases based on the values of these SPTO parameters $(\beta, \omega, \mu, \nu)$, let us discuss briefly how to obtain them from a numerical perspective. As we can see from the above commutation relations, the most important step involved is in extracting the matrices R_x, R_z and R_t. We will explain briefly here how to extract these matrices for one particular case, the R_x matrix for example. We list the important steps of this process as follows:

1. Define the local symmetry operators as $X = e^{i\pi S^x}$, $Y = e^{i\pi S^y}$, $Z = e^{i\pi S^z}$ where S^x, S^y and S^z are the usual spin-2 operators.

2. Make sure that the MPS tensors are in their canonical form. In our case, we use the iTEBD algorithm to simulate the ground state of our Hamiltonian using an iMPS of two-site unit cell. The iTEBD algorithm automatically ensures that the tensors in the ground state are in their canonical form. This is shown in Fig. 4.8(a) for clarity.

3. Apply the local symmetry operator to the tensors as shown in Fig. 4.8(b) and obtain the relevant transfer matrix.

4. Extract the eigenvector of this transfer matrix and take its complex conjugate transpose. In Fig. 4.8(b), the eigenvector is denoted by W. We can now obtain the matrix $U_x = W^\dagger$. We therefore obtain the R_x matrix from this. The other matrices R_z and R_t can be obtained similarly.

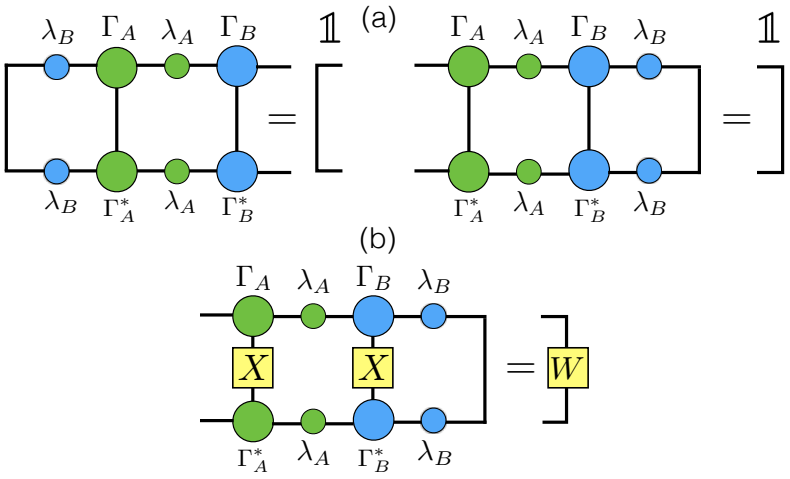

Figure 4.8: (a) Left and right canonical conditions of an iMPS of two-site unit cell (b) Extracting the projective representation matrix of the symmetry operator $X = e^{i\pi S^x}$.

The matrices R_x, R_z and R_t can now be obtained from the U_x, U_z and U_t matrices using the definition $U_x \equiv R_x, U_z \equiv R_z$ and $U_t \equiv R_t K$. Here K is the complex conjugation operation, defined by $KAK^{-1} = A^*$ and $K = K^{-1}$. The important steps involved are shown in Fig. 4.8 for illustrations. The procedure explained in Ref. [133] is just a simple MPS calculation, and we address the interested reader to that reference for further information. In this reference, the procedure shown is for an infinite MPS with one-site translational invariance which is different from our case.

Once the above matrices have been determined as we explained, we normalize them so that $R_x^2 = R_z^2 = \mathbb{1}$, and $R_t^2 = U_t K U_t K = U_t U_t^* = \pm\mathbb{1}$. Let us assume that all these matrices are $\chi \times \chi$, with χ the MPS bond dimension. It is easy to see that the parameters $(\beta, \omega, \mu, \nu)$ can now be computed as

$$\beta = \frac{1}{\chi}\mathrm{tr}(R_t^2) = \frac{1}{\chi}\mathrm{tr}(U_t K U_t K) = \frac{1}{\chi}\mathrm{tr}(U_t U_t^*) \tag{4.27}$$

$$\omega = \frac{1}{\chi}\mathrm{tr}(R_x R_z R_x^\dagger R_z^\dagger) \tag{4.28}$$

$$\mu = \frac{1}{\chi}\mathrm{tr}(R_x R_t R_x^\dagger R_t^\dagger) = \frac{1}{\chi}\mathrm{tr}(R_x U_t K R_x^\dagger K U_t^\dagger) = \frac{1}{\chi}\mathrm{tr}(R_x U_t R_x^T U_t^\dagger) \tag{4.29}$$

$$\nu = \frac{1}{\chi}\mathrm{tr}(R_z R_t R_z^\dagger R_t^\dagger) = \frac{1}{\chi}\mathrm{tr}(R_z U_t K R_z^\dagger K U_t^\dagger) = \frac{1}{\chi}\mathrm{tr}(R_z U_t R_z^T U_t^\dagger). \tag{4.30}$$

Once the SPTO parameters have been computed, the different spin-1 SPT phases can be identified based on the classification scheme used in [140]. Of the 16 SPT phases protected by $\mathbb{Z}_2 \times \mathbb{Z}_2 + T$ symmetry, four of them can be realized in a spin chain. These effective spin-1 SPT phases based on the different values of SPTO parameters

Phase	β	ω	μ	ν
$T_0 = \text{IH}$	-1	-1	-1	-1
T_x	+1	-1	-1	+1
T_y	+1	-1	+1	+1
T_z	+1	-1	+1	-1

Table 4.2: Different effective spin-1 SPT phases protected by $(\mathbb{Z}_2 \times \mathbb{Z}_2) + T$ symmetry.

are listed in Table 4.2. The numerical results of where these SPT phases are found in the phase diagram of our model are shown in Fig. 4.9. In this way, we are able to determine precisely to which one of the 16 SPT phases protected by $(\mathbb{Z}_2 \times \mathbb{Z}_2) + T$ symmetry belongs a given MPS.

4.1.3 Final phase diagram and phase transitions

In the previous sections, we have identified the different SPT phases based on their entanglement properties, hidden string orders, etc. Not only this, we have also distinguished between the different spin-1 SPT phases using the projective representation of the $\mathbb{Z}_2 \times \mathbb{Z}_2 + T$ symmetry which cannot be done otherwise using the previous techniques. Based on all these results, we plot the final phase diagram of our spin-2 model for the four different planes. This is shown in Fig. 4.10. It can be seen from this figure that the SO(5) Haldane phase characterized by a quadruple degeneracy in the entanglement spectrum, non-zero value of the SOPs $\mathcal{O}^{12}$ and $\mathcal{O}^{34}$ appear in all the four planes. The four different planes (a,b,c and d) correspond to the $\langle J_1, D\rangle$, $\langle J_2, D\rangle$, $\langle J_3, D\rangle$ and $\langle J_4, D\rangle$ plane respectively. The $\langle J_1, D\rangle$ plane is marked with the presence of three different effective spin-1 SPT phase: the T_0, the T_y and the T_z phase. The $\langle J_2, D\rangle$ plane has only the T_0 phase for the parameter regime considered in this study. The $\langle J_3, D\rangle$ plane is very similar to the $\langle J_1, D\rangle$ plane with almost the same phases. The $\langle J_4, D\rangle$ plane is marked with the presence of T_0 phase and the T_x phase which were not present in the other planes. All these T_0, T_x, T_y and T_z phases are effective spin-1 SPT phases characterized by a double degeneracy of the entanglement spectrum and non-vanishing value of the SOP $\mathcal{O}^{34}$. Of all these phases, we noticed that the T_y phase has a very large entanglement entropy. There are two possible scenarios for this. The first possibility is that the T_y phase is a gapped phase with a very small gap. The second possibility is that it is indeed a gapless critical phase (which is a bit counter-intuitive to the definition of SPT phase). We have explicitly checked that the entropy seems to increase with the bond dimension in this phase and

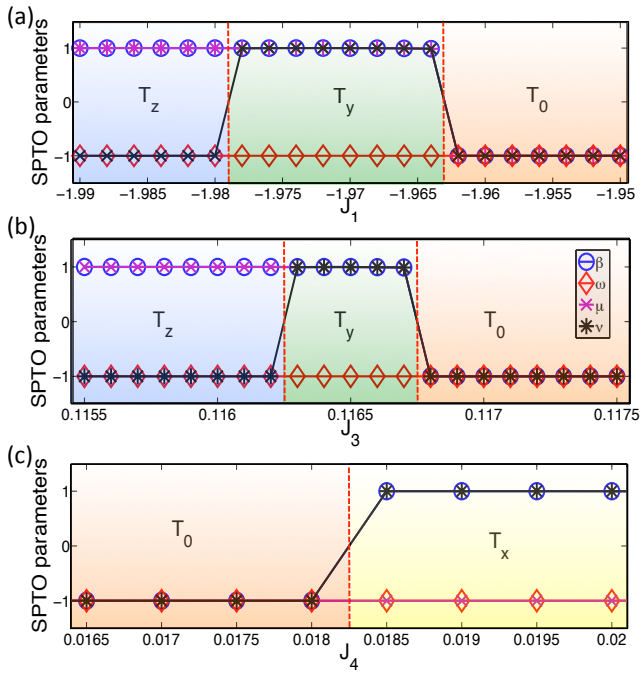

Figure 4.9: SPT parameters $(\beta, \omega, \mu, \nu)$ for (a) the $\langle J_1, D\rangle$ plane at $D = 1$, (b) the $\langle J_3, D\rangle$ at $D = 1.5$, and (c) the $\langle J_4, D\rangle$ plane at $D = 1$. The data are consistent with four different effective spin-1 SPT phases, separated by vertical red dashed lines.

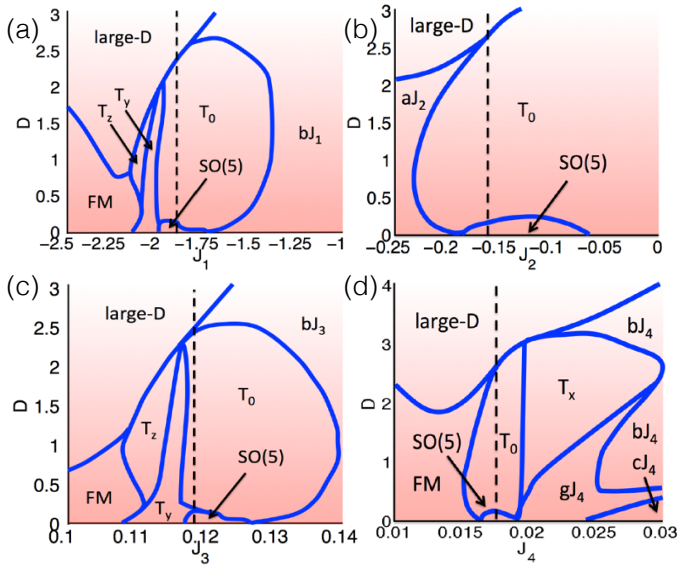

Figure 4.10: Final phase diagram of our spin-2 chain in the four two-dimensional planes. We identify five different SPT phases: the SO(5) Haldane phase, the T_0 phase, the T_x phase, the T_y phase and the T_z phase, the later four of which are effective spin-1 SPT phases. The dashed line in each panel corresponds to the SO(5) symmetric point for $D = 0$.

therefore the second possibility seems more likely. If this is indeed the case, we can say that the T_y phase in our model exhibits both gapless degrees of freedom and to some extent, SPT order, which deserves further investigations. It is worth mentioning that the possibility of the existence of gapless SPT phases have been reported in some cases [147].

Before we discuss other interesting features of the phase diagram, it is important that we describe the phase transition between the different SPT phases in the different planes. It is known that the entanglement entropy of a block of length L obeys the following scaling law [148, 149, 149, 150, 150]

$$S(L) \sim \frac{c}{3} \log L + O(1/L) \tag{4.31}$$

for $L \gg 1$ where c is the central charge of the transition. After extracting the value of this central charge, one can understand the phase transition using the CFT description. For example, consider the phase transition between two different spin-1 SPT phases T_y and T_0 in $\langle J_1, D\rangle$ plane in Fig. 4.10. We compute the entanglement entropy at this region for a block of different lengths (up to $L = 100$) for increasing bond dimensions (up to $\chi = 120$). The scaling of this entanglement entropy with both the system size L and $\log L$ is shown in Fig. 4.11. By making an appropriate fit for this scaling, we extract the central charge of this transition and found it to be $c = 3 \times 0.6528 \approx 2$. Such a transition can be understood in terms of five Majorana fermions [139]. A detailed description of the phase transition in terms of these Majorana field theories can be found in appendix A of the thesis. A similar behavior was obtained for the phase transitions between the other spin-1 SPT phases. Meanwhile, the phase transition between the SO(5) Haldane phase and Intermediate Haldane phase and the phase transition between IH phase and the Large-D phase was found to correspond to a CFT with central charge $c = 2 \times \frac{1}{2} = 1$. The Majorana field theory of these transitions is described in Ref. [139].

Besides the topological phases, we find a number of interesting features in our model which we discuss very briefly here. For example, in the $\langle J_4, D\rangle$ plane, we find a candidate for gapless phase which we call $gJ4$ which has an entanglement spectrum degeneracy of 2 but no string order. We conjecture this phase to be in the XY universality class, as this was also found in other spin-2 chains. We also find very high and low- J phases at every planes which are topologically trivial and which correspond to different symmetry-breaking orders (e.g. ferromagnetic). An in-depth analysis of all these phases, together with the phase diagram of the model in the full parameter space could be really interesting for future studies.

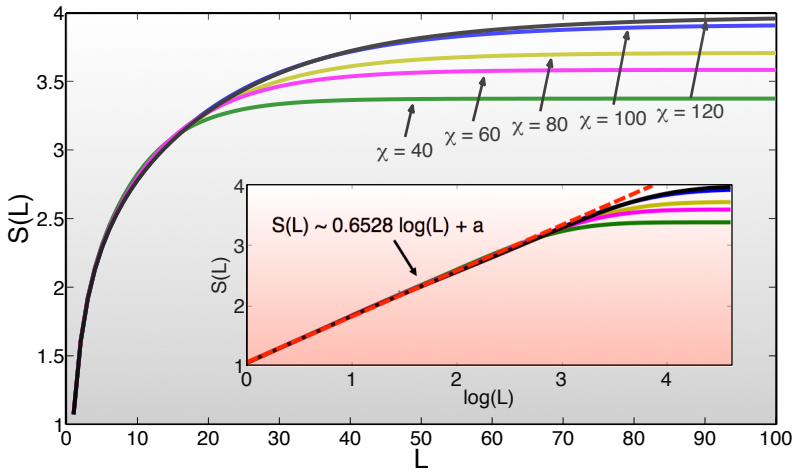

Figure 4.11: Scaling of the entanglement entropy $S(L)$ of a block of length L for the T_y -T_0 transition in Fig. 4.9(b) at $D = 1.5$. In the inset we plot the same data, but in semi logarithmic scale. The results are consistent with a central charge $c = 3 \times 0.6528 \approx 2$. χ is the MPS bond dimension.

4.2 SPt phases in spin-2 chain

Having discussed the concept of Symmetry Protected Topological phases, their classification based on the projective representation of the symmetries protecting them and their phase transitions, in this section, let us discuss a new class of material known as the Symmetry Protected trivial phases (SPt) phases. Symmetry Protected trivial phases are the product-state analog of Symmetry Protected Topological (SPT) phases. They can be adiabatically connected to a product state by some path that preserves the protecting symmetry unlike the SPT phases that can be connected to the product state only by a path that breaks the protecting symmetry. Thus, SPT and SPt phases can be adiabatically connected to each other when interaction terms that break the symmetries protecting the SPT are added in the Hamiltonian. However, two distinct SPt phases cannot be adiabatically connected to each other unless the symmetries protecting them is explicitly broken in the Hamiltonian. In other words, there are distinct product states that can be infinitely close in the limiting regions of a given phase diagram yet separated by a quantum critical point with diverging correlation lengths between them. These phases of matter were studied for the first time in [135] in the context of a spin-1 chain. The SPt phases found there are protected by a combination of site-centered inversion (I_s) and a π rotation about the z axis. It is worth reminding here that according to the convention used by Wen [106], SPT phases are also called Symmetry Protected trivial states because

there is no long-range entanglement (or intrinsic topological order such as string-net models). In our convention, (i) SPT means that the corresponding quantum states cannot be fully disentangled without breaking the protecting symmetry (equivalently, they are not adiabatically connected to a product state by any path preserving the symmetry), and (ii) SPt means that the corresponding quantum states can be fully disentangled without breaking the protecting symmetry (equivalently, they are adiabatically connected to a product state by some path preserving the symmetry). Our convention here is, however, compatible with the one in Ref. [135].

In this section, we will investigate the existence of different SPt phases in the spin-2 chain discussed previously along with their phase transitions. This study can be understood in the context of generalizations of SPt phases for higher spin-chains. We use the same numerical tool as we did before in the previous section i.e. Matrix Product States with iTEBD algorithm to obtain the ground states. We will characterize the phases of this model by studying quantities such as entanglement entropy, symmetry-related non-local order parameters and 2-site fidelities. The field theory description of the quantum phase transitions is also discussed in Appendix A. This section is based on the publication [151] by the author.

4.2.1 Model and symmetries

We will simply add a staggered magnetic field to our Hamiltonian in Eq. 4.1 for a spin-2 chain. The reason for this will be apparent soon. The Hamiltonian of our model now has the following form.

$$H = \sum_j \sum_{\gamma=1}^{4} J_\gamma (\vec{S}_j \cdot \vec{S}_{j+1})^\gamma + D \sum_j (S_j^z)^2 - h_z \sum_j (-1)^j S_j^z, \tag{4.32}$$

where $\vec{S}_j$ and S_j^z are the usual spin-2 vector and its z component, D is a uniaxial anisotropy and h_z is a staggered magnetic field, and J_γ's are values of bilinear, biquadratic, bicubic and biquartic couplings, respectively, for $\gamma = 1, ..., 4$. We have already discussed the case for which $D = 0$ and for specific values of J_γ's for which the model has an exact SO(5) symmetry and the ground state can be written as an MPS with bond dimension 4. We have also discussed in detail the case for an arbitrary J_γ and non-zero values of D. Now, let us discuss the case for which D and h_z in the above Hamiltonian are non-zero but J_γ's are fixed to their SO(5) symmetric values (i.e. $J_1 = -11/6, J_2 = -31/180, J_3 = 11/90, J_4 = 1/60$). In this case, the presence of the staggered field destroys all the symmetries protecting the SPT order.

However, the model is still symmetric under site-centered inversion I_s and π rotations with either the u^{12} or the u^{34} defined as

$$u^{12} = e^{i\pi L^{12}}, u^{34} = e^{i\pi L^{34}}, \tag{4.33}$$

where $L^{12} = |2\rangle\langle 2| - |-2\rangle\langle -2|$ and $L^{34} = |1\rangle\langle 1| - |-1\rangle\langle -1|$ are the SO(5) Cartan generators. We can then define quantized SPt order parameters using the combined symmetries as follows

$$\begin{aligned} I'_{12} &= I_s \times u^{12} \\ I'_{34} &= I_s \times u^{34} \end{aligned} \tag{4.34}$$

which are also exact symmetries of the Hamiltonian in this regime. As we shall see later, the presence of these two symmetries protect three trivial phases in our model, separated by quantum critical points corresponding to $c = 1$ CFTs. One of these phases is adiabatically connected to the intermediate Haldane phase for $h_z = 0$, and corresponds to an intermediate SPt phase.

4.2.2 Identifying SPt phases

Our aim, now, is to study the phase diagram of the spin-2 quantum Hamiltonian in Eq. 4.32, where the couplings J_γ are fixed to the SO(5) point, and both D and h_z can take finite values. For the sake of simplicity, we restrict ourselves to the case $D > 0$ and $h_z > 0$. In our numerical simulations, we approximated the ground state of the system by an infinite MPS with a 2-site unit cell using the iTEBD algorithm as before. We used MPS of bond dimension up to $\chi = 100$, which turned out to be already sufficient for our purpose. We compute the following parameters numerically which are described in detail along with important discussions of the results as follows.

Entanglement entropy

As a first numerical calculation we computed the entanglement entropy (von Neumann entropy) of half an infinite chain, which can be extracted easily from the MPS tensors. Details on how to extract the entanglement entropy from the ground state MPS were already discussed in the previous section. We compute this for a very large number of points in the $\langle D, h_z\rangle$ plane. This is shown in Fig. 4.12. The left part of the figure

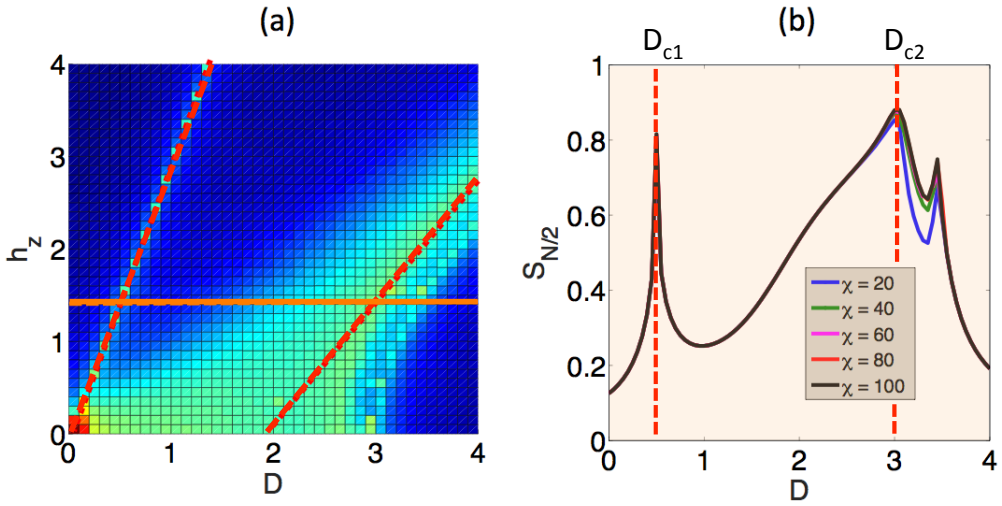

Figure 4.12: (a) Entanglement entropy of half an infinite chain for $\chi = 100$, aerial view. The two red dashed lines correspond to the asymptotic laws in Eq. 4.35 for the entropy maxima at $D \gg 1$. The horizontal orange line corresponds to $h_z = 1.5$, for which the entanglement entropy is plotted on the right panel. (b) Entanglement entropy of half an infinite chain for $h_z = 1.5$ and different bond dimensions χ. Results largely overlap within our precision away from criticality. The two maxima on the right-hand side tend to get closer as χ and D increases (not shown).

shows the entanglement entropy of half an infinite chain from the ground state MPS of bond dimension $\chi = 100$. The right part of the figure also shows the same quantity but for $h_z = 1.5$ and for different bond dimensions. From this, we can see that the entanglement entropy increases with the bond dimension χ at the two regions marked as D_{c1} and D_{c2}. In the limit $\chi \to \infty$, we expect such entropies to diverge, thus pinpointing two quantum critical lines separating three phases. As we shall see, this interpretation is also consistent with the analysis of nonlocal order parameters. We also find that the maxima for the entanglement entropy in the critical lines follows the following laws for the two critical regions

$$\begin{aligned} h_z &\sim a_l + 3D(\text{left}), \\ h_z &\sim a_r + D(\text{right}), \end{aligned} \tag{4.35}$$

when $D \gg 1$, and for some constants $a_l(\text{left})$ and $a_r(\text{right})$. Such a behavior is expected [152] and we provide an intuitive argument as following. For $h_z = D$, we find that the non-interacting part of the Hamiltonian in Eq. 4.32 for an even site j can be written using the usual spin-2 z basis as

$$D(|2\rangle\langle 2| + |-1\rangle\langle -1|) + 6|-2\rangle\langle -2|) \tag{4.36}$$

with a similar result for odd sites but interchanging $|2\rangle$ with $|-2\rangle$ and $|1\rangle$ with $|-1\rangle$. This means that for large enough D, the dominant low-energy physics will happen mostly in the 2-dimensional local subspace spanned by $\{|0\rangle, |1\rangle\}$ for even sites and $\{|0\rangle, |-1\rangle\}$ for odd sites. So, locally, the low-energy physics in this limit resembles that of a spin-1/2 system. After projecting the interacting part of the Hamiltonian into this local basis, one gets a behavior similar to that of the spin-1/2 XXZ model, which in its critical region has $c = 1$ CFT. Similarly, for $h_z = 3D$ we find that the non-interacting piece of Eq. 4.32 for an even site is given by

$$D(-2(|-2\rangle\langle -2| + |-1\rangle\langle -1|) + 4|1\rangle\langle 1| + 10|2\rangle\langle 2|), \tag{4.37}$$

again with a similar result for odd sites but interchanging $|2\rangle$ with $|-2\rangle$ and $|1\rangle$ with $|-1\rangle$. This could also suggest that for large D, the dominant physics happens in a 2-dimensional local subspace, namely, the one spanned by $\{|-2\rangle, |-1\rangle\}$ for even sites and $\{|2\rangle, |1\rangle\}$ for odd sites. Following the same argumentation as before, the relevant low-energy properties in this limit would then be that of some spin-1/2 XXZ model with $c = 1$. Of course, this is just an intuitive argument and needs to be taken with care, but it would be in agreement with the field theory description in the case of having critical lines. Nevertheless, as we shall discuss, it is also plausible that one has a scenario with first-order transitions, and therefore these limiting cases should be taken with care.

Indeed, these results are also compatible with the numerical study of the scaling of the entanglement entropy. As shown in Fig. 4.13, the scaling of the entanglement entropy $S(L)$ of a block of size L is compatible in both cases with the CFT scaling in the thermodynamic limit as we discussed before

$$S(L) \sim \frac{c}{3} \ln L + c_1' \tag{4.38}$$

with central charge $c \sim 1$, once again in agreement with the previous considerations (in the above equation, c_1' is a non-universal constant for an infinite chain, but for open boundary conditions it may also include the Affleck-Ludwig boundary entropy [153]). More precisely, at $h_z = 1.5$ and for the first critical point D_{c1} we get $c = 0.2501 \times 3 \approx 0.75$, whereas for the second critical point D_{c2} we get $c = 0.34 \times 3 \approx 1.02$. The lower numerical central charge at D_{c1} can be explained by the fact that this is a fine-tuned quantum phase transition between two trivial phases, corresponding to product states under renormalization group theory. It is thus expected that the central charge is slightly underestimated by this fact, since trivial phases have very little entanglement. The same would be expected for the numerical central charge at D_{c2} . However, this

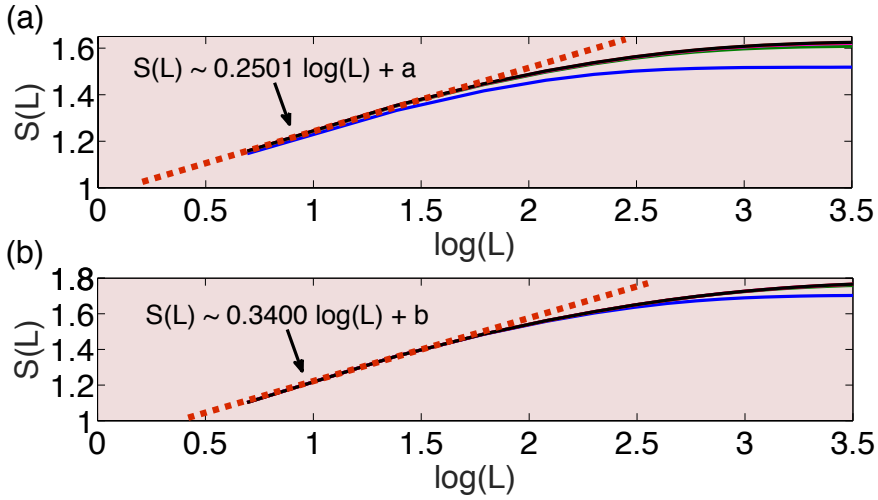

Figure 4.13: Entanglement entropy of a block of size L, at the two maxima of Fig. 4.12 for $h_z = 1.5$: (a) at $D_{c1} = 0.5$; (b) at $D_{c2} = 3$. The orange dashed line is a fit to the law in Eq. 4.38 in the scaling region. The values of the bond dimension are the same as in Fig. 4.12.

point is in the middle of a region with more entanglement (see Fig. 4.12), which apparently softens the underestimation of c. Our conclusion is that both lines are compatible with a critical behavior, and seem to correspond to CFTs with central charge $c = 1$ which can be described using two sine-Gordon bosons and one Majorana fermion. The details of this explanation can be found in Appendix A of the thesis. In any case, we would like to stress that within our accuracy we cannot rule out the possibility that the first phase transition is indeed first order, with a saturation of the entanglement entropy in the bond dimension of the MPS. This scenario would also be a plausible explanation of the observed low value for the central charge in our calculations.

Two-site fidelities

It is clear that introducing the staggered field term breaks explicitly the symmetries protecting the SPT phases at $h_z = 0$. Thus, for large values of h_z one may expect distinct polarized phases. In order to identify them, we have computed the two-site

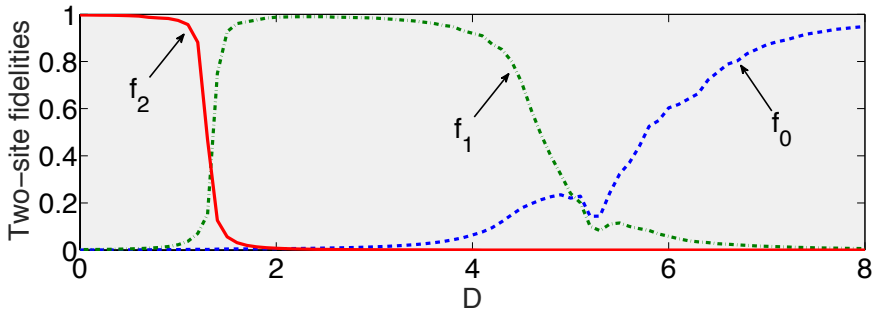

Figure 4.14: Two-site fidelities f_0, f_1 and f_2 as defined in Eq. 4.39 at $h_z = 4$, signaling 3 different trivial phases for $\chi = 100$.

fidelities defined as follows

$$\begin{aligned} f_0 &= \frac{1}{2}\left(\langle 0|\rho_{odd}|0\rangle + \langle 0|\rho_{even}|0\rangle\right), \\ f_1 &= \frac{1}{2}\left(\langle 1|\rho_{odd}|1\rangle + \langle -1|\rho_{even}|-1\rangle\right), \\ f_2 &= \frac{1}{2}\left(\langle 2|\rho_{odd}|2\rangle + \langle -2|\rho_{even}|-2\rangle\right), \end{aligned} \tag{4.39}$$

where ρ_{odd} is the 1-site reduced density matrix of the system for an odd site, and analogously for ρ_{even}. The results are shown in Fig. 4.14, and clearly show that the ground state of the system tends to be in three different trivial phases, which have the following product states as representatives for large h_z: $|2,-2,2,-2...\rangle$ for small D, $|1,-1,1,-1...\rangle$ for intermediate D, and $|0,0,0,0...\rangle$ for large D.

Nonlocal order parameter

Our numerical calculations also indicate that the three distinct trivial phases discussed above are in fact protected by symmetries. More specifically, the symmetries protecting the phases are those specified in Eq. 4.34: I'_{12} and I'_{34} consisting of site-centered inversion combined with a π rotation according to operator u^{12} or u^{34} in Eq. 4.33. Therefore, one can define some nonlocal order parameters that can be used to distinguish the three trivial phases. Such nonlocal order parameters can be computed very easily in the MPS framework. Such calculations were proposed for the first time in [144] in the context of SPT phases. Let us review here briefly for the sake of completeness how to compute this for an infinite-size MPS with translational invariance at every two sites (which is what we used in our simulations). The different steps are summarized in Fig. 4.15. First, given an infinite MPS in canonical form and with a two-site unit cell, we can define two tensors A and B as in Fig. 4.15(a) satisfying

O^A_{12}	O^A_{34}	Representative	Phase
-1	+1	$\|2,-2,2,-2,...\rangle$	small D
+1	-1	$\|1,-1,1,-1,...\rangle$	intermediate D
+1	+1	$\|1,-1,1,-1,...\rangle$	Large D

Table 4.3: Different SPt phases found in our spin-2 quantum chain. The one for intermediate D corresponds to an intermediate SPt phase.

right-canonical conditions as in Fig. 4.15(b). The symmetry operator $I' = I_s \times \mathbb{Z}_2$ acts on the MPS tensors as shown in Fig. 4.15(c), which for our spin-2 case will be defined at a later stage, and where the site-centered inversion I_s simply takes the transpose of the bond indices in the MPS tensors A and B. Matrices u_A and u_B correspond to representations of the symmetry operators acting on the MPS bond indices, and can be computed from the dominant right eigenvectors of 2-site MPS transfer matrices as shown in Fig. 4.15(d). In turn, angles θ_A and θ_B can be extracted from the single-site MPS transfer matrices as shown in Fig. 4.15(e). Finally, angles ϕ_A and ϕ_B are computed as in Fig. 4.15(f). With all the data extracted in this way, one can then define the SPt nonlocal order parameter following [144] as

$$O^A \equiv e^{i(\theta_A - \phi_A)} = \pm 1 \tag{4.40}$$

Equivalently, one can also define O^B using θ_B and ϕ_B. Let us stress at this point that the non-local order parameter depends on the definition of the π rotation operator u. In our spin-2 case, we use the following different operators defined in Eq. 4.33 in order to distinguish the different phases emerging in our model as follows

$$u^{12} = e^{i\pi L^{12}}, \;\; u^{34} = e^{i\pi L^{34}}, \tag{4.41}$$

where L^{12} and L^{34} are the SO(5) Cartan generators defined previously. Using these definitions of the operations, one can now distinguish the different phases in our model. This is shown in Fig. 4.16. Thus, we have classified the different SPt phases using the two operators. The results are summarized in the Table 4.3.

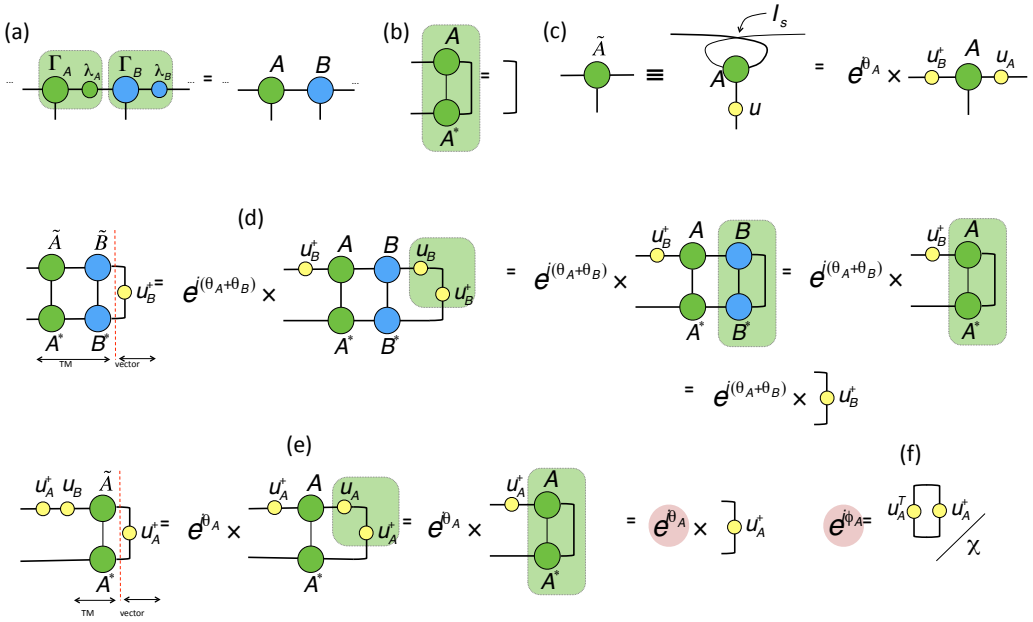

Figure 4.15: (a) MPS tensors A and B are defined;(b) tensor A satisfies the right canonical condition (similarly for B); (c) action of the symmetry operator $I' = I_s \times \mathbb{Z}_2$ on tensor A (similarly for B); (d) matrix $u_B^\dagger$ is the right eigenvector of a 2-site MPS transfer matrix (TM), with eigenvalue $e^{i((\theta_A+\theta_B))}$ (one reaches a similar conclusion by interchanging A with B); (e) the phase $(e^{i\theta_A})$ (highlighted in red) can be extracted using $u_A^\dagger$ and a 1-site MPS transfer matrix built with tensor A (one reaches a similar conclusion by interchanging A and B); (f) the phase $(e^{i\phi_A})$ (highlighted in red) can be extracted as shown in the diagram, where χ is the MPS bond dimension.

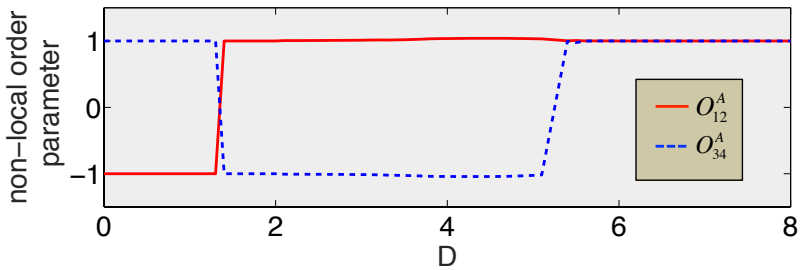

Figure 4.16: Nonlocal order parameters O_{12}^A and O_{34}^A as in Eq. 4.40 at $h_z = 4$ determining 3 different SPt phases, for $\chi = 100$.

4.3 Conclusions and outlook

In this chapter, we have discussed the concept of Symmetry Protected Topological (SPT) and Symmetry Protected trivial (SPt) phases which are different from the conventional phases of matter and therefore lies beyond the Landau paradigm of phase classification. The usual techniques used in classifying conventional phases of matter cannot be applied in these cases. To give a formal definition, SPT phases of matter are short-range entangled states that can be adiabatically connected to a product state only after we destroy the symmetries protecting them. Two SPT phases cannot be adiabatically connected to each other without removing the symmetries protecting them. Because SPT phases are robust against any local external perturbations that preserve the symmetry, they have been proposed as a resource in certain measurement-based quantum computing and other areas of quantum information. The Haldane phase of the spin-1 chain is a very important example of such SPT phases. This is a gapped phase characterized by interesting properties such as non-trivial degeneracy of the entanglement spectrum, presence of hidden string orders, etc. The search for spin-1 Haldane phase in higher spin-chains has been a hot topic of research since it was conjectured in 1992. Symmetry Protected trivial (SPt) phases, on the other hand, are the product state analogue of SPT phases. These are short range entangled states that can be adiabatically connected to product states by some path that preserves the symmetry. Just like SPT phases, two SPt phases cannot be adiabatically connected to each other unless we remove the symmetries protecting them. The main conclusions and outlook of this chapter are summarized below.

- Using a spin-2 quantum chain with a Heisenberg-like bilinear, biquadratic, bicubic and biquartic interactions along with an uniaxial anisotropy term, our studies have confirmed the existence of several effective spin-1 SPT phases. Not only did we find the spin-1 Haldane phase in our study, we also found other spin-1 SPT phases which are also typical of the Haldane phase protected by $\mathbb{Z}_2 \times \mathbb{Z}_2 + T$ symmetry. All these phases were studied using a number of quantities such as entanglement spectrum, string order parameter, entanglement entropy, projective representation of the symmetries protecting the phases, etc.

- Our studies also form the first numerical evidence of phase transitions between different spin-1 SPT phases. These phase transitions can be described using a $c = 2$ CFT which can be understood in terms of five Majorana fermions.

- During our investigation, we have found a phase namely the T_y phase that has the properties of an SPT but possibly exhibiting gapless degrees of freedom. This is somewhat counter-intuitive to the definition of SPT phases which are gapped and therefore deserves further investigation. It will also be interesting to explore the full phase diagram of our model in all the possible regimes. These ideas could form the basis of a possible future work.

- We have also shown how to characterize an SPt phase based on a number of properties such as entanglement entropy and its scaling, nonlocal order parameters, 2-site fidelities, etc as well as how to distinguish it from an SPT phase. We have also shown that just like the case of SPT, our spin-2 model also contain an effective spin-1 SPt phase when we add an external staggered magnetic field to it. We found three distinct SPt phases protected by a combination of site-centered inversion and π rotation along one of the axes.

- We also studied the phase transition between the different SPt phases and found that they can be described with a $c = 1$ conformal field theory which can be understood in terms of two sine-Gordon bosons and one Majorana fermion.

- Concerning perspectives, it would be interesting to determine whether an SPt phase with negative value of both nonlocal order parameters $\mathcal{O}_A^{12}$ and $\mathcal{O}_A^{34}$ could also exist in a simple quantum spin chain. Another interesting open problem is the characterization of SPt phases in 2D. We leave the study of these problems for the future.

Chapter 5

Frustrated Quantum Systems

Early studies of frustrated quantum systems date back to the study of the antiferromagnetic Ising model on the triangular lattice by G.H. Wannier [154] and R.M.F. Houtappel [155] in 1950. The Heisenberg helical structure which is also a frustrated system was discovered independently by A. Yoshimori, J. Villain and T.A. Kaplan in 1959 [156, 157, 158]. Such systems gained more importance in the context of the study of spin glasses by G. Toulouse and J. Villain in 1977 [159, 160]. Although the investigation of such frustrated quantum systems started a long time back, many properties of frustration still continue to be a puzzle in the era of modern physics and pose some of the hardest challenges in condensed matter physics. Because of the presence of large amounts of quantum fluctuations in such systems, they are a perfect playground for realizing exotic quantum many-body states such as the quantum spin liquid[1] and also serves as an excellent testing ground for approximations and theories. Apart from the fact that most materials in nature do not have a bipartite structure and hence are frustrated, the study of frustrated quantum systems also serves as an important platform in the theoretical understanding of high-T_c superconductors (Anderson's RVB theory for example) [17]. Before getting into any details, let us try to understand how frustration arises and how one can define it formally.

Let us consider two spins $\vec{S}_i$ and $\vec{S}_j$ (classical or quantum) interacting with a strength J. Their interaction energy can then be written as $E = -J(\vec{S}_i \cdot \vec{S}_j)$. Assuming these spin vectors to be of unit length, we see that for $J > 0$ (ferromagnetic interaction), the minimum energy is given by $E_{\text{min}} = -J$ when $\vec{S}_i \parallel \vec{S}_j$ (i.e. when the spins are parallel). For the case of $J < 0$ (antiferromagnetic interaction), we see that the minimum energy $E_{\text{min}} = -J$ is obtained when $\vec{S}_i \uparrow\downarrow \vec{S}_j$ (i.e. when they

[1] A Quantum Spin liquid is defined as a disordered state that preserves all the symmetries of the parent Hamiltonian.

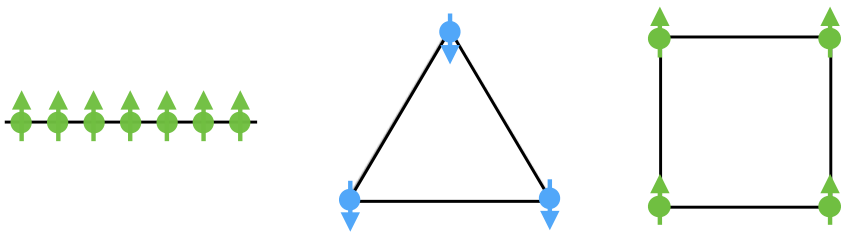

Figure 5.1: Possible ground states of the ferromagnetic Hamiltonian where all the spins are aligned parallel to each other. The ground state does not depend on the structure of the lattice and the energy constraints of all the individual bonds are fully satisfied here.

are antiparallel). Now the following cases can arise for the two different kinds of interactions:

Case 1: For a nearest-neighbor ferromagnetic interaction, the ground state is the configuration where all the spins are aligned in parallel to one another. In this case, the energy constraint of the interaction of every pair of spins is fully satisfied. This condition will be fulfilled for all kinds of lattice structures such as the square lattice, triangular lattice or a 1D chain. There is no frustration in this kind of model. This is shown in Fig. 5.1.

However, for an antiferromagnetic interaction, the configuration of the ground state will depend on the lattice structure as follows

Case 2(a): For lattices containing no elementary triangles (i.e. bipartite, square or simple cubic), the ground state is the configuration where each spin is antiparallel to its neighbor So, in this case also, the energy constraints for all the bonds can be fully satisfied and there is no frustration in the system. This is illustrated in Fig. 5.2(a) for a square lattice.

Case 2(b): Now, consider the case when the spins reside on lattices containing elementary triangles (non-bipartite structures such as triangular, fcc or hcp lattices). In such a scenario, we see that a ground state where all the bonds have a perfectly antiferromagnetic interaction is not possible to construct. Hence the system is said to be frustrated. This is illustrated in Fig. 5.2(b).

Based on the above illustrations, we are now in a position to formally define 'Frustration'. A system is said to be frustrated if the minimum of the total energy does not correspond to the minimum of each bond, or in other words, if the energy

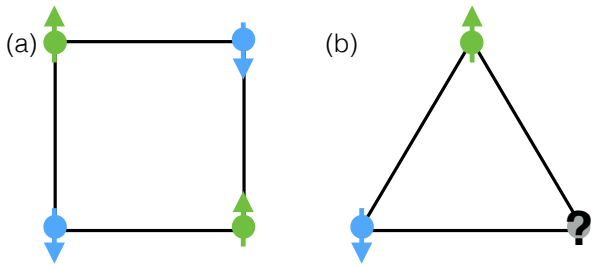

Figure 5.2: (a) Ground state of an antiferromagnetic Hamiltonian in which the neighboring spins are aligned in opposite directions to each other in a square lattice. The energy constraints of all the bonds are simultaneously satisfied and there is no frustration in the system. (b) In the case of a triangular lattice, all the neighboring spins cannot be aligned antiparallel to each other and therefore, the system is said to be frustrated.

constraint of every bond cannot be simultaneously satisfied[2]. Basically, frustration is usually caused by (a) competition of different kinds of interactions and/or (b) the lattice geometry (triangular lattice, fcc, etc). For the former case, one can take the example of a square lattice where there is ferromagnetic interaction on three of the bonds and an antiferromagnetic interaction on the remaining bond. It can be seen easily that in such a system, the energy constraints of all the bonds cannot be simultaneously satisfied and therefore it is frustrated. There is another interesting definition of frustration owing to G. Toulouse [161]. According to him, a plaquette is said to be frustrated if the parameter

$$P = \prod_{\langle i,j \rangle} \text{sign}(J(i,j)) \tag{5.1}$$

is negative. P is the product of the signs of the interaction of all the bonds around the plaquette. An antiferromagnetic (ferromagnetic) interaction has a negative (positive) sign by convention. One can check quickly the examples described above that this is indeed the case. It is worth mentioning that frustration often leads to a lot of interesting phenomenon in physics such as ground state degeneracy, order-by-disorder, etc but it is beyond the scope of this thesis to get into the details of these mechanisms. Examples of highly frustrated lattices include the triangular, kagome, pyrochlore structures, etc. In the next section, we would like to discuss a paradigmatic example of a frustrated quantum system, the ground state of which is controversial even in

[2]'Frustration-freeness' of a Hamiltonian is also often related to the commutivity of its terms.

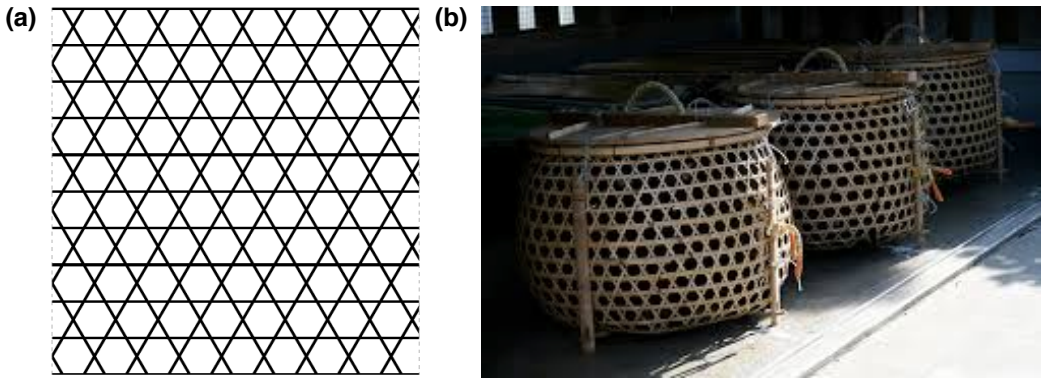

Figure 5.3: (a) Highly frustrated kagome lattice due to the presence of corner sharing triangles. The lattice can be considered as composed of elementary triangles and hexagons. (b) Traditionally woven Japanese bamboo baskets having a kagome pattern.

the present day. This is the spin-1/2 Kagome Heisenberg Antiferromagnet (KHAF). We will study this model using our TN algorithms and see how it compares with the existing state-of-the-art techniques.

5.1 The Kagome Heisenberg Antiferromagnet

The kagome lattice is a highly frustrated lattice due to the presence of corner sharing triangles (shown in Fig. 5.3). The word 'kagome' comes from the two Japanese words 'kago' meaning basket and 'me' meaning eyes. It refers to the pattern of a traditionally woven Japanese bamboo basket (shown in Fig. 5.3(b)). Given the high geometric frustration of the lattice, finding the ground state of the spin-1/2 kagome Heisenberg antiferromagnet is considered to be one of the hardest problems in condensed matter physics and hence it is very hard to tackle this problem either numerically or analytically. This is because of strong quantum fluctuations, giving rise to many low-energy states competing to be the true ground state. Even after more than 20 years of study, there is still no clear consensus about the nature of its ground state [162, 163, 164, 165, 166, 167, 168]. Many techniques have been used so far to attack this problem such as MERA [168], Coupled Cluster Methods [169], Variational Monte Carlo [170], Density Matrix Renormalization Group [171, 172] and many others. There have been two proposals for the ground state of this model: one is the so-called quantum spin liquid (QSL), proposed by Anderson [173]. This

is a very exotic state because the ground state does not break any symmetry of the parent Hamiltonian in this case. It is very difficult to get a cartoon picture of how such a state would look like but it can be considered as a liquid of spins just like a classical liquid where the molecules form a dense and strongly correlated state without forming any static order. As these states do not break any symmetry, there is no local order parameter that can be used to classify them and hence fall beyond Landau's theory of phase transition [131]. Such a state has only been seen in a few materials [174]. The other possible ground state for such a model that has been proposed is the Valence Bond Crystal (VBC). In this case, two spins can form a singlet which is also known as valence bond due to their antiferromagnetic interaction. The ground state would then be a configuration where every spin is bound to some singlet. Such an ordering breaks the lattice symmetry because there is only one specific arrangements of the valence bonds. It also lacks the long-range entanglement and hence is not topologically ordered. However, if we take equal superposition of all the possible configurations of the valence bonds without preferring any specific order, then we will have what is known as the *Resonating Valence Bond (RVB)* state which is a type of Quantum Spin Liquid proposed by Anderson [173]. Thus, it is possible to construct, in principle, a quantum spin liquid from superposition of all the possible VBCs by introducing quantum fluctuations which prohibit the ground state from choosing any specific valence bond order. While the energetically lowest study has claimed a $\mathbb{Z}_2$ quantum spin liquid for the ground state of the Kagome Heisenberg Antiferromagnet [172], there are other studies that favor a Valence Bond Crystal (VBC) [175]. Recently, it was claimed that the ground state of this model is a gapless spin liquid [176]. There are also some experimental results that favor a $\mathbb{Z}_2$ quantum spin liquid as the ground state of this model [174]. This is based on the investigation of many naturally occurring mineral compounds such as *Herbertsmithite* ($ZnCu_3(OH)_6Cl_2$), *Volborthite*($Cu_3V_2O_7(OH)_2 \cdot 2H_2O$) and *Vesignieite* ($BaCu_3(OH)_6Cl_2$) that has a kagome structure with the spin-1/2 Heisenberg antiferromagnetic interaction. Using our TN techniques, we will also investigate the nature of the ground state of this model.

The Hamiltonian of this model can be written as follows

$$H = \sum_{\langle i,j \rangle} \vec{S}_i \cdot \vec{S}_j, \tag{5.2}$$

where $\vec{S}_i = (S_i^x, S_i^y, S_i^z)$ and S_i^x, S_i^y and S_i^z are the usual spin-1/2 operators at a particular site and the sum is over all nearest-neighbor sites in the kagome lattice.

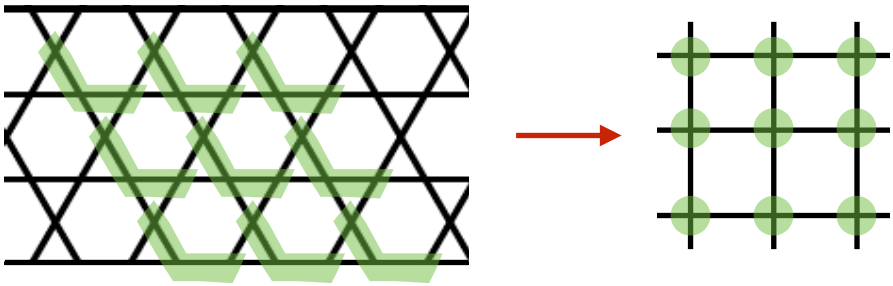

Figure 5.4: Mapping the spins in the kagome lattice to a square lattice. Three spin-1/2s in the kagome lattice is mapped to a single spin in the coarse-grained square lattice. The mapping preserves the locality of interactions.

The interaction is Heisenberg antiferromagnetic and the interaction strength is taken to be unity for simplicity. As we mentioned, such kinds of interaction can also be found in nature in many mineral compounds. In this thesis, we will restrict ourselves only with the spin-1/2 case. Studies for higher spins in the kagome lattice can be found in Ref. [177, 178, 179, 180, 169].

Using our infinite Projected Entangled Pair States (iPEPS) technique, we would, first of all, like to compute the ground state of the Hamiltonian in Eq. 5.2. This can be done using the so-called Simple Update (SU) [181, 182], Full Update (FU) [183] or Fast Full Update (FFU) [184] techniques which are all based on iPEPS. The simple update does not take into account the environment of the tensors while updating the specific tensors while the full update does. The fast full update, as the name suggests, is a faster and more stable version of the full update technique. In this technique, the environment and the specific tensors are simultaneously updated throughout the evolution. The details of these techniques can be found in Appendix C of the thesis for the interested readers. These techniques use the imaginary time evolution (iTEBD) algorithm. But before using the above techniques directly, one needs to map the spins in the kagome lattice to a square lattice. It should be possible to program an iPEPS code directly in the kagome lattice. Still, thanks to this mapping, we are able to use the code for the square lattice, which is much more convenient to program. Moreover, there is the added advantage that the coarse-graining takes exactly into account the interactions between the three spins being coarse-grained. The mapping is shown in Fig. 5.4. It can be seen from this mapping that three spins in the kagome lattice are mapped to a single site in the coarse-grained square lattice. Also, two kagome links correspond to one single link in the square lattice. Because all the nearest-neighbors in

the kagome lattice are mapped to either a single site or nearest-neighbor in the square lattice, such a mapping automatically ensures the locality of interactions. Now that we have a square lattice, we can use the full iPEPS machinery to compute the ground state of our model using the different update schemes. We use an iPEPS algorithm with 2 and 4-site unit cell so that in the original kagome lattice we have a 6 and 12-site unit cell. But for most parts of our algorithm, we will be using the 2-site unit cell in the square lattice. To see how our technique compares with the existing results and other techniques, we will first of all, compute the ground state energy of our model. It is worth mentioning here that our iPEPS algorithm has been bench marked with several other models such as the Classical Ising model, Quantum Ising model, etc in the square lattice by computing observables such as energy, magnetization, etc [183, 185]. We, however, do not present the bench marking results here in this thesis for reasons of brevity.

5.1.1 Energy and nature of the ground state

The ground state energy of the Hamiltonian is defined as

$$E_0 = \frac{\langle \psi_0 | H | \psi_0 \rangle}{\langle \psi_0 | \psi_0 \rangle} \tag{5.3}$$

where $|\psi_0\rangle$ is the ground state wave function of our Hamiltonian H and E_0 is the ground state energy. Thus, once we have the ground state wave function using the different update schemes, we can easily compute the energy as defined above. We shall compute this for different bond dimensions D of the iPEPS. We know that D is the refining parameter of our wave function and it quantifies the amount of entanglement we allow in the system. Another important thing to be mentioned here before presenting the numbers is that in order to compute observables such as the expectation value of the energy or magnetization, one needs to compute the environment of the ground state tensors. This is often the bottleneck in our computations since we consider an infinite system and exact contraction of PEPS tensors is known to be a computationally hard problem [112]. However, one can efficiently approximate the environment of the iPEPS tensors using techniques such as Corner Transfer Matrix Renormalization Group (CTMRG) [51], Higher Order Tensor Renormalization Group (HOTRG) [85], etc. In this thesis, we will only use the CTMRG technique to compute the environment. The bond dimension of the environment χ is also an important parameter to be considered here. The details on how to compute the environment using this technique can also be found in Appendix C of the thesis.

D	χ	Energy (Simple Update)	Energy (Fast Full Update)
2	4	-0.418976421	-0.419483175
3	9	-0.425157130	-0.424253237
4	16	-0.429085014	-0.429323201
5	20	-0.429881267	N/A

Table 5.1: Ground state energy per site for the Kagome Heisenberg Antiferromagnet for different bond dimensions of the iPEPS D and bond dimension of the environment χ using the simple update and fast full update technique. The energy for $D = 5$ could not be computed using the fast full update due to computational limitations. The numbers provided in this table are only for bench marking purposes. In principle, it is possible to go to larger bond dimensions. See Ref. [186].

The ground state energy per site of the KHAF are shown in Table 5.1 for different bond dimensions D for the iPEPS and bond dimension χ for the environment for the different update schemes. In this table, we have only shown the ground state energy per site for bond dimensions $D = 2, 3, 4, 5$ of the iPEPS. The environment bond dimensions are $\chi = 4, 9, 16, 20$ respectively. Usually, it is enough for the environment bond dimension to be the square of the PEPS bond dimension i.e. $\chi \propto D^2$. We could not take $\chi = 25$ for the case of $D = 5$ for computational reasons. The computed energies were obtained using both the simple update and fast full update technique. We also see that the fast full update technique tends to give better energies because it takes into account the full environment while updating the tensors. The energy for $D = 5$, however, with fast full update could not be computed due to limitations on computational memory. Thus, we can see from Table 5.1 that the best value of the energy is given by $D = 5$ simple update which is -0.429881267. The best energy obtained so far for this model is -0.4386 using DMRG [172]. Thus, we can already see that the energy obtained using our technique is going towards this value even with small bond dimensions of the iPEPS. However, it needs to be pointed out here that it is not the purpose of this thesis to push our computational limit and therefore a one-to-one comparison with our technique would not be fair. To have a comparison on fairer grounds using our technique, one can take a look at Ref. [186] where the model was studied for large bond dimensions of the iPEPS and environment. The energies were then extrapolated for infinite bond dimension of the iPEPS using CTMRG method and the energy obtained was -0.43448 This is shown in Fig. 5.5. Moreover, there is still so much more scope in pushing the computational limit of our calculations using different tactics like incorporating symmetries in the tensors so that the computations are much more efficient, using GPUs instead of CPUs to

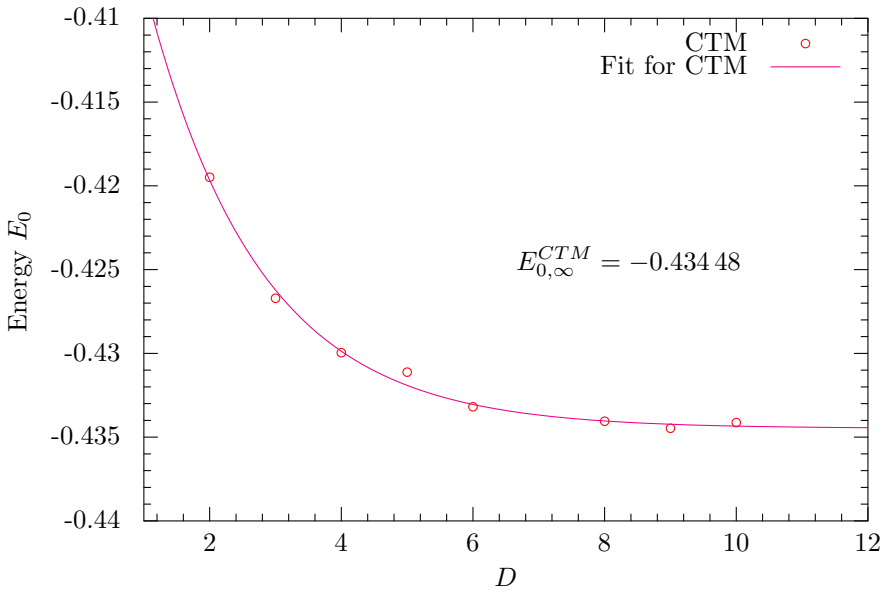

Figure 5.5: Ground state energy per site computed using our iPEPS technique for different bond dimensions D. The energies have been computed using the CTM technique for the environment. The energies were then extrapolated for infinite bond dimensions. This plot has been taken from Ref. [187]

perform computations, parallelizing the code, using faster and more efficient matrix decomposition techniques, etc, just to name a few. These are some of the things that we would like to do in the future.

Let us now probe the nature of the ground state of the model that we have computed using our iPEPS. For this, we will plot something known as the bond strength map. We will compute the energy of every individual bond of the kagome lattice and plot the relative energies of every link in the kagome lattice. This will give us an idea of some of the symmetries our ground state wave function has. For a quantum spin liquid that does not break any symmetries, all the links in the kagome lattice should have similar energies (up to the computational precision). This will not be the case for other forms of ground state. The bond strength map of the ground state of our model is shown in Fig. 5.6 for different bond dimensions D of the iPEPS. From this, we can say that our numerical technique does not give us any hint of a quantum spin liquid. Instead, the spins are arranged in specific patterns of singlets and hence would be some kind of a Valence Bond Crystal. It is indeed possible that the quantum spin liquid ground state is realized only for larger bond dimensions of the iPEPS since they are known to be long-range entangled. But within our computational limit, we are unable to give a definitive conclusion on this.

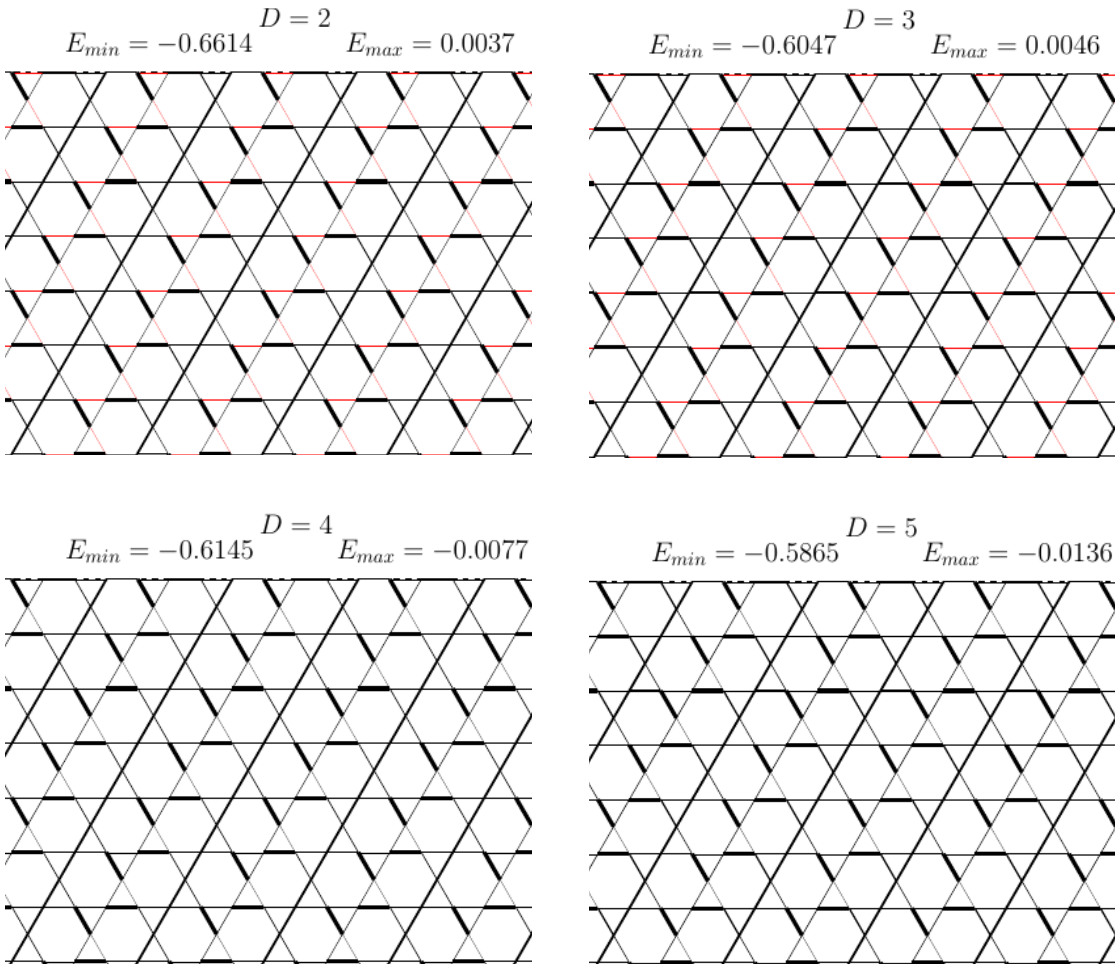

Figure 5.6: Bond strength map of the KHAF for different bond dimensions ($D = 2, 3, 4, 5$) of the iPEPS. We see that the spins form specific pairs of singlets for all the bond dimensions and therefore, it is unlikely that the ground state will be a quantum spin liquid. However, it is difficult to infer how the bond strength map will change for the case of infinite bond dimension of the iPEPS.

5.1.2 KHAF in the presence of a field

Having probed the ground state of the Kagome Heisenberg Antiferromagnet, we would now like to ask the question "What happens when we introduce an external magnetic field to such a frustrated system?" The answer to this question is highly non-trivial and in fact leads to the emergence of many exotic phases of matter occurring as magnetization plateaus with extremely interesting physics. For example it was shown that introducing an external magnetic field to the kagome Heisenberg model leads to the emergence of 1/3 magnetization plateaus [188, 189, 190, 191]. However, this claim was contested by several other studies [192, 193]. In Ref. [194], it was clarified that during the process of magnetization, the magnetization plot does not appear as a curve but rather as a staircase of heights. This was attributed to the possible finite size effects of the numerical technique used. They also noticed that the value of magnetization jumped from 7/9 to the full saturation value. Then in 2013, these so-called plateaus were probed once again for systems in the thermodynamic limit by means of a grand canonical analysis so that there is no finite size effects [195]. The study found the existence of five different plateaus at fractions $M/M_{\text{sat}} = 0, 1/9, 1/3, 5/9$ and 7/9 as well as a magnetic jump from the 7/9 plateau to the full saturation value at $M/M_{\text{sat}} = 1$. The process of saturation occurred exactly at $H_{\text{sat}}/J = 3$. M_{sat} is the full magnetization, H_{sat} the value of the external field at which the saturation occurred and J is the strength of the antiferromagnetic interaction in the Hamiltonian. In ref. [186], the nature and existence of these magnetization plateaus were investigated thoroughly using iPEPS for the spin-S (i.e. $S = 1/2, 1, 3/2, 2$) kagome Heisenberg antiferromagnets. The Hamiltonian in the presence of the external field can be written as

$$H = \sum_{\langle i,j \rangle} \vec{S}_i \cdot \vec{S}_j - h \sum_i S_i^z \tag{5.4}$$

where the first term is the Heisenberg antiferromagnetic interaction summed over all the nearest-neighbors. The second term is the external field along z direction and h is the value of the external field. $\vec{S}_i$ and $\vec{S}_j$ is the usual spin vectors and S_i^z is the z-component of the spin vector at a particular site. They found that the magnetization curve hosted a large number of exotic phases of matter in the presence of the external field. We will try to give an overview of these phases here. The different magnetization plateaus found in these studies for different spin S kagome Heisenberg antiferromagnet is shown in Fig. 5.7. From this plot, we can see the emergence of several magnetization plateaus for the spin-1/2 case such as $1/9, 1/3, 5/9$ and 7/9

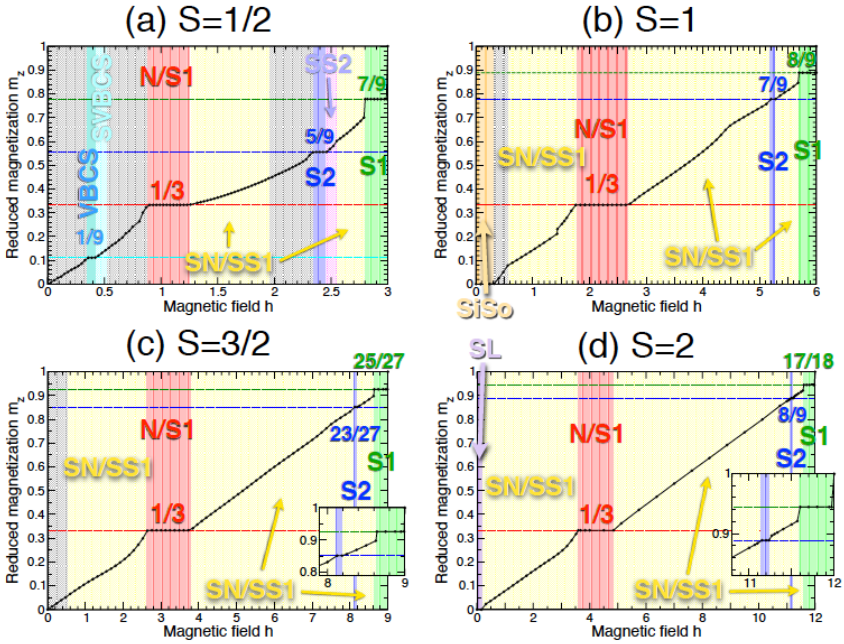

Figure 5.7: Emergence of different magnetization plateaus for different spin S kagome Heisenberg antiferromagnet. The figure has been taken from Ref. [186] with permission from the authors.

plateaus. Besides this, they also found plateaus for the spin-1, spin-3/2 and spin-2 kagome Heisenberg antiferromagnet. For instance, for the $S = 1$ case, we see plateaus at $M/M_{\text{sat}} = 1/3, 7/9, 8/9$, for the spin $S = 3/2$, we see the plateaus at $1/3, 23/27, 25/27$ and finally for spin $S = 2$ at $1/3, 8/9, 17/18$ values of the reduced magnetization. It is beyond the scope of this thesis to discuss all the plateaus for the different spin models. Therefore, we will restrict ourselves only to the case of spin-1/2 which is also the most interesting and widely studied case because of the large amount of quantum frustration present in the system.

The different phases seen in Fig. 5.7 can be classified using Table 5.2 based on the breaking (preserving) of symmetries like the $U(1)$ spin rotational symmetry, translational symmetry G_T, C_6 rotation symmetry and reflection symmetry along two orthogonal axis σ_u and σ_v of the ground state. Thus, the 1/9 plateau in this case was found to be a Valence Bond Crystal Solid (VBCS). Such an incompressible phase preserves the $U(1)$ spin rotational symmetry, breaks the translation symmetry into a $\sqrt{3} \times \sqrt{3}$ structure, breaks the C_6 rotation symmetry entirely and has reflection symmetry along only one axis. The 1/3 plateau is found to be degenerate between the so-called Nematic and Solid 1 phase. The Nematic phase preserves both the $U(1)$

Nature of phase	$U(1)$	G_T	C_6	σ_u	σ_v
Spin Liquid (SL)	✓	✓	✓	✓	✓
Simplex Solid (SiSo)	✓	✓	C_3	✓	×
Superfluid (SF)	×	✓	✓	✓	✓
Solid 1 (S1)	✓	$\sqrt{3}\times\sqrt{3}$	✓	✓	✓
Solid 2 (S2)	✓	$\sqrt{3}\times\sqrt{3}$	C_2	✓	✓
VBC-Solid (VBCS)	✓	$\sqrt{3}\times\sqrt{3}$	×	✓	×
Nematic (N)	✓	✓	C_2	✓	✓
Supersolid 1 (SS1)	×	$\sqrt{3}\times\sqrt{3}$	✓	✓	✓
Supersolid 2 (SS2)	×	$\sqrt{3}\times\sqrt{3}$	C_2	✓	✓
Super VBCS (SVBCS)	×	$\sqrt{3}\times\sqrt{3}$	×	✓	×
Supernematic (SN)	×	✓	C_2	✓	✓

Table 5.2: Classification of the different plateaus based on the symmetries of the ground state.

spin rotational symmetry and translational symmetry G_T. However, it breaks the C_6 rotation symmetry to a C_2 meaning that it is symmetric under rotation by π. It also has reflection symmetry along the two axes σ_u and σ_v. On the other hand, the Solid 1 phase preserves the $U(1)$ spin rotational symmetry but breaks the translation symmetry into a $\sqrt{3}\times\sqrt{3}$ structure. It preserves the rest of the other symmetries. The 5/9 plateau then belongs to the Solid 2 phase which is very similar to the Solid 1 phase except that it breaks the C_6 to a C_2 rotation. Lastly, the 7/9 plateau was also found to belong to the Solid 1 phase. All these plateaus are incompressible phases because, by increasing the magnetic field, we cannot increase their magnetization. In the next section, we will move towards investigating the existence and properties of these plateaus for a more general model i.e. the XXZ model in the kagome lattice with antiferromagnetic interaction. The Kagome Heisenberg Antiferromagnet would then just be a single point in the phase diagram of the general XXZ model. The next section of the chapter is based on the publication [196] of the author.

5.2 The Kagome XXZ model

The Hamiltonian of the Kagome XXZ model with antiferromagnetic interaction can be written as follows

$$\mathcal{H} = \sum_{\langle ij\rangle} \cos\theta \left(S_i^x S_j^x + S_i^y S_j^y\right) + \sin\theta \left(S_i^z S_j^z\right) - h\sum_i S_i^z, \tag{5.5}$$

where $S_i^\alpha = \sigma_i^\alpha/2$ is the spin-1/2 αth operator at site i, h is the magnitude of the magnetic field, θ is the anisotropy angle, and the interaction is for nearest-neighbor spins. For generic values of h and θ this Hamiltonian has $U(1)$ symmetry under spin rotations around the z-axis. Different interesting points can be accessed by tuning the parameter θ, namely:

1. The Heisenberg point for $\theta = \frac{\pi}{4}$.
2. The XY point for $\theta = 0$.
3. The Ising point for $\theta = \frac{\pi}{2}$.

Although there have been a lot of studies recently on the magnetization plateaus of the Heisenberg point $\theta = \pi/4$ as we discussed in the previous section, the case for the XY point has been particularly controversial and the general XXZ model has not been studied so far. For example, in Ref. [197], it was claimed that the 1/3 magnetization plateau does not exist in the XY point. What is more interesting is that in Ref. [198], it was claimed that the 1/3 plateau exists and that it could be a chiral spin liquid at the XY point. These confusion initially instigated our investigation and we would also like to ask the question that if the 1/3 plateau exists at the XY point, what is the nature of its ground state and what happens to it as we tune the anisotropy angle θ i.e. as we go from the XY point to the Ising point passing through the Heisenberg point. We will give the answers to these questions by studying the zero-temperature phase diagram of the model in this section.

In order to obtain the ground state of the above Hamiltonian, we will use an additional numerical technique which is very similar to the iPEPS technique that we described in the previous section. This technique is known as the iPESS (infinite Projected Entangled Simplex State) [117]. It is simply a variation of the usual iPEPS technique except that here we use additional simplex tensors. In this technique, we use an embedded cluster of 9 sites as shown in Fig. 5.8. Thus, there are 9 different site tensors and 6 different simplex tensors which are repeated all over the kagome lattice in the thermodynamic limit[3]. So, finally in the end, we end up using two different techniques: (i) a 9-site iPESS techniques based on simplex tensors and (ii) the usual iPEPS technique with 6 and 12-site unit cell in the kagome lattice (the mapping of the kagome lattice to the square lattice for this case has been discussed

[3]The numerical simulations using the iPESS techniques were done in the group of Prof. Poilblanc in Toulouse. Here, we have presented the results for the sake of completeness and to provide a comparison with our techniques.

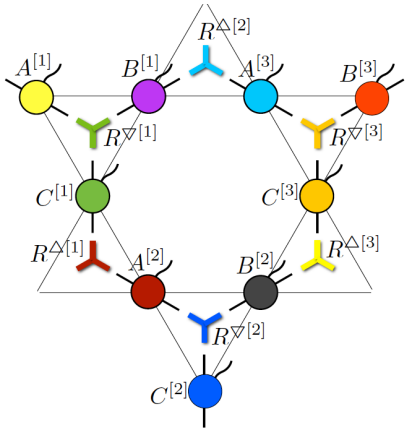

Figure 5.8: Tensor Network of 9 sites per unit cell composed of 9 site tensors and 6 simplex tensors. Figure taken from Ref. [186] with permission from the authors.

in the previous section). We used simple update in both the techniques because of its efficiency. For the second technique, we also used the so called fast full update but since it did not bring any significant difference in the results, we employ the simple update in the remainder of this chapter. The second approach based on the coarse-grained kagome lattice is less efficient but it has more variational parameters, which can handle a larger amount of entanglement in the wave function. In all cases, our refining parameter is the iPEPS bond dimension D, which controls the amount of entanglement in the tensor network, and which we consider up to $D = 5$.

5.2.1 Phase diagram

In this section, we will investigate the ground state phase diagram of our XXZ model as a function of the anisotropy angle θ and the external magnetic field h. Let us first investigate the existence of the different magnetization plateaus for different parameter regimes of our XXZ model using the two different techniques. This is shown in Fig. 5.9 for the 9-site iPESS and Fig. 5.10 for the 6-site iPEPS. Let us, first of all, take a look at the former case. On the horizontal axis is the value of the anisotropy angle θ and on the vertical axis is the value of the external magnetic field h. Thus $\theta = 0$ on the horizontal axis is the XY point, $\theta = 0.25$ the Heisenberg point and $\theta = 0.5$ the Ising point. From this figure, we can clearly see the existence of 1/3 magnetization plateau both for $D = 3$ and $D = 5$. The 1/3 plateau can be seen in all parameter regimes (i.e. all values of θ) of the XXZ model using the 9-site iPESS technique. Using this technique, one can also see the existence of other

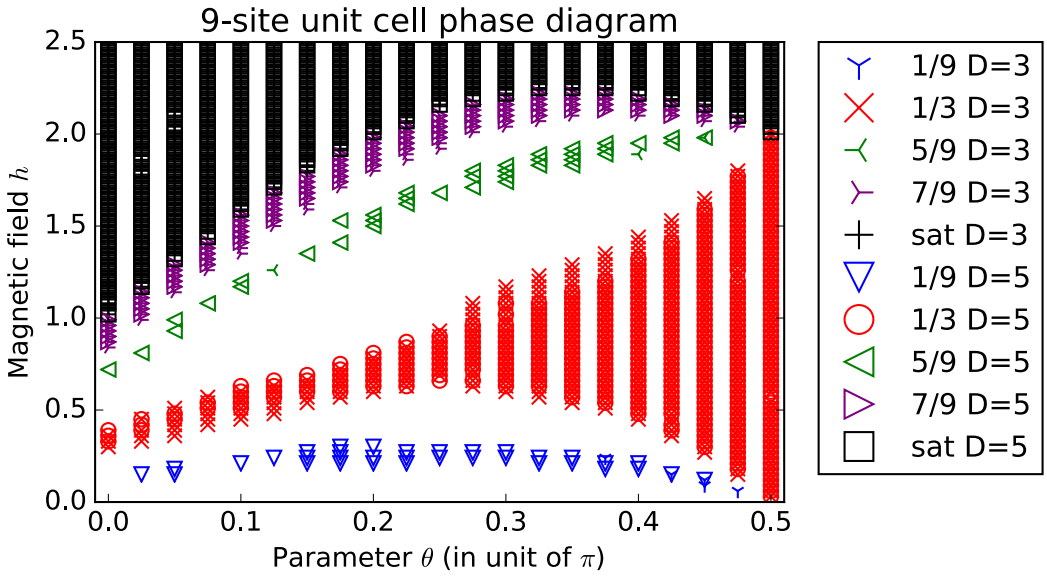

Figure 5.9: Emergence of different magnetization plateaus using the 9-site iPESS technique in different parameter regimes of the model. The results are for bond dimensions $D = 3$ and $D = 5$ for the iPESS algorithm.

plateaus besides the 1/3 such as the 1/9, 5/9 and 7/9 plateaus in different regimes of the model. This is similar to what was earlier found for the Heisenberg case but we also find it for the XY point and other values of the anisotropy angle. Now, let us look at Fig. 5.10. It is the same phase diagram but using the other technique i.e. 6-site iPEPS. Here also, we can find the 1/3 magnetization plateaus for different bond dimensions $D = 3$ and $D = 5$ before it saturates into the full magnetization in different parameter regimes of the model including the XY point. For concreteness, in Fig. 5.11 we show the magnetization curve, i.e. m_z as a function of the external field h obtained with the 6-site algorithm, for different values of the anisotropy angle $\theta \in [0, \pi/2]$. We observe the presence of a very prominent magnetization plateau at $m_z = \frac{1}{3}$, for all the scanned values of θ, including the XY, Heisenberg and Ising points. Away from the Ising point we also see a jump towards the saturation value $m_z = 1$ for several values of θ [189]. The width of the plateau increases as we tune θ from the XY towards the Ising point, see Fig. 5.12. Results for the 12-site algorithm are essentially identical. It is worth noting that the 6 and 12-site iPEPS techniques do not find the presence of 1/9, 5/9 and 7/9 plateaus. This is because they are not commensurate with the expected magnetic structure of the other plateaus. Thus, we realize that incorporating the correct lattice symmetry is quite important while using the iPEPS

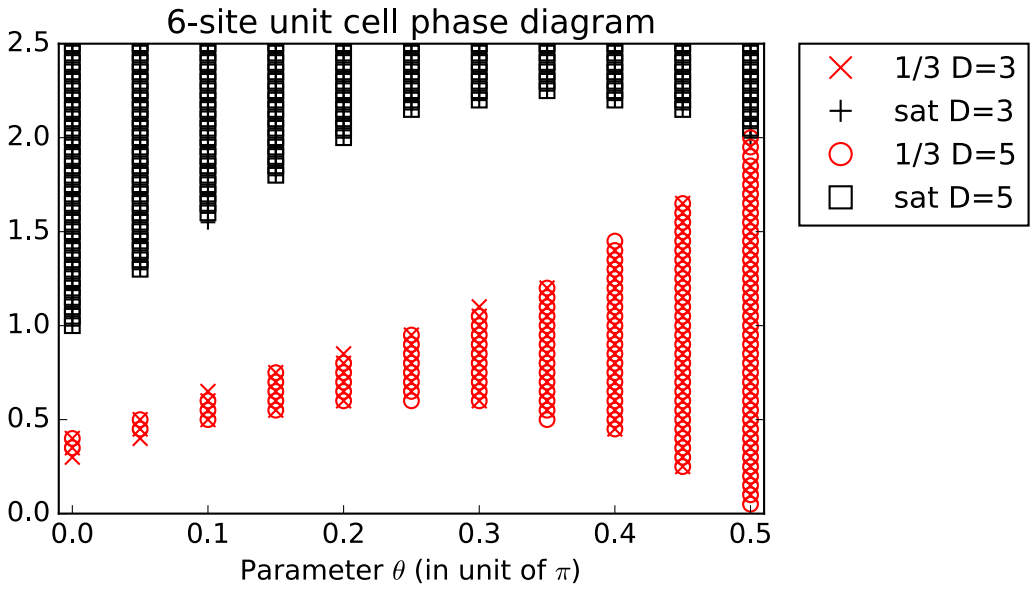

Figure 5.10: 1/3 magnetization plateaus found using the 6-site iPEPS technique in different parameter regimes of the model. The results are for bond dimensions $D = 3$ and $D = 5$ for the iPEPS algorithm. The phase diagram is identical using the 12-site unit cell.

technique. However, based on these two independent numerical techniques, we can confirm the presence of the 1/3 magnetization plateau at the XY point of the XXZ Hamiltonian which was one of the main goals of our investigation.

5.2.2 The 1/3 plateau: Lattice Nematic vs Solid orders

Now that we have confirmed the existence of several magnetization plateaus (including the most prominent 1/3 plateau at the XY point) in the XXZ model using the two different techniques, we would like to focus on the nature of the ground state of these 1/3 plateaus and see if they undergo phase transition as we move from the XY to the Ising through the Heisenberg point. In order to probe this, we will plot the longitudinal magnetization at every site as well as the link energy terms $\langle h_{ij} \rangle$ at every different link (without the Zeeman term), for the 6-site iPEPS and the 9-site iPESS calculations, for points in the $m_z = 1/3$ plateau and four different anisotropy angles θ. This is shown in the right panel of Fig. 5.13 for the 9-site iPESS technique. Using this technique, we found that for every possible value of the anisotropy angle θ, Nematic and Solid 1 orders are degenerate in energy within our accuracy. Let us remind ourselves that the Nematic phase breaks the C_6 rotation symmetry into C_2

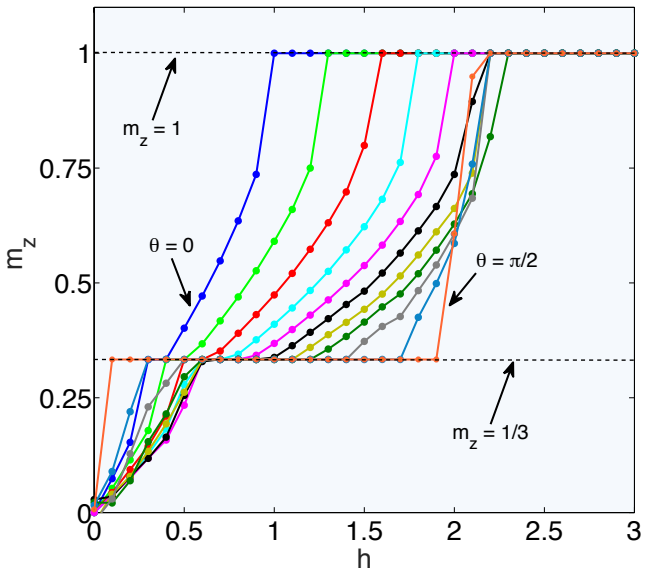

Figure 5.11: Magnetization m_z (along the field) as a function of the external magnetic field h in intervals of $\Delta h = 0.1$ for values of the anisotropy angle $\theta \in [0, \pi/2]$ at intervals of $\Delta\theta = \pi/20$, computed with the 6-site approach with bond dimension $D = 3$. The magnetization saturates at $m_z = 1$ (dotted line), and there is clearly a plateau at $m_z = \frac{1}{3}$ (dotted line) for all θ, including the XY point at $\theta = 0$.

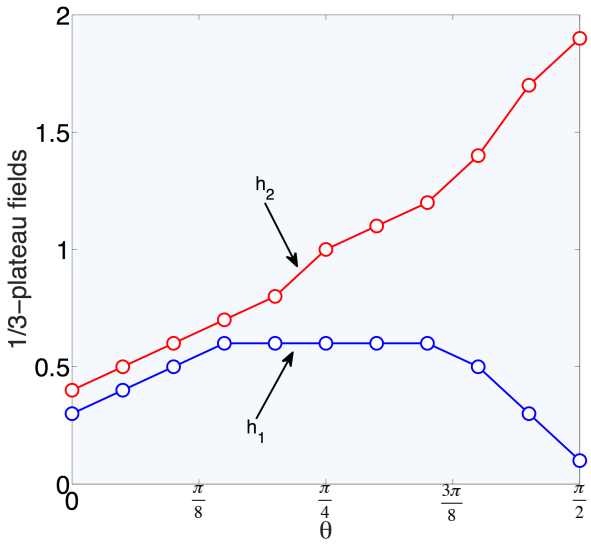

Figure 5.12: Left-most (h_1) and right-most (h_2) values of the field at the $m_z = \frac{1}{3}$ plateau for the different considered angles. The width of the plateau is given by $h_2 - h_1$. The parameters of the simulations are the same as in Fig. 5.11. At the Ising point $\theta = \pi/2$ we find $h_2 - h_1 = 2$ up to our finite-Δh resolution ($\Delta h = 0.1$), in agreement with the exact classical result.

while preserving the rest of the symmetries such as the $U(1)$ spin rotation, translation and reflection symmetry along two orthogonal axes. The Solid 1 phase on the other hand breaks the translation symmetry to a $\sqrt{3} \times \sqrt{3}$ structure while preserving the rest of the symmetries. The structures in Fig. 5.13 are examples of what we obtain in some runs of the algorithm. The red (blue) dot corresponds to positive (negative) value of magnetization and the red (blue) links correspond to positive (negative) value of the energy per links of the kagome lattice. By running the algorithm with different random initial conditions, we get either a Nematic or $\sqrt{3} \times \sqrt{3}$ Solid 1 state, both with the same energy.

In the case of the 6 and 12-site iPEPS, we also find degenerate ground states between Nematic and Valence Bond Crystal Solid. The Valence Bond Crystal Solid in this case breaks the C_6 rotation, breaks the translation symmetry into a 1×2 structure and has reflection symmetry only along one axis. Some examples of what we obtain in different runs of our 6 and 12-site algorithm are shown in the left panel of Fig. 5.13. Thus, we show the Nematic ground state for $\theta = \pi/10, \pi/4$ and 0.35π and 1×2 Valence Bond Crystal-Solid for $\theta = 0.45\pi$. However, we found that the degeneracy between the Nematic and the VBC-Solid seems to be slightly lifted in

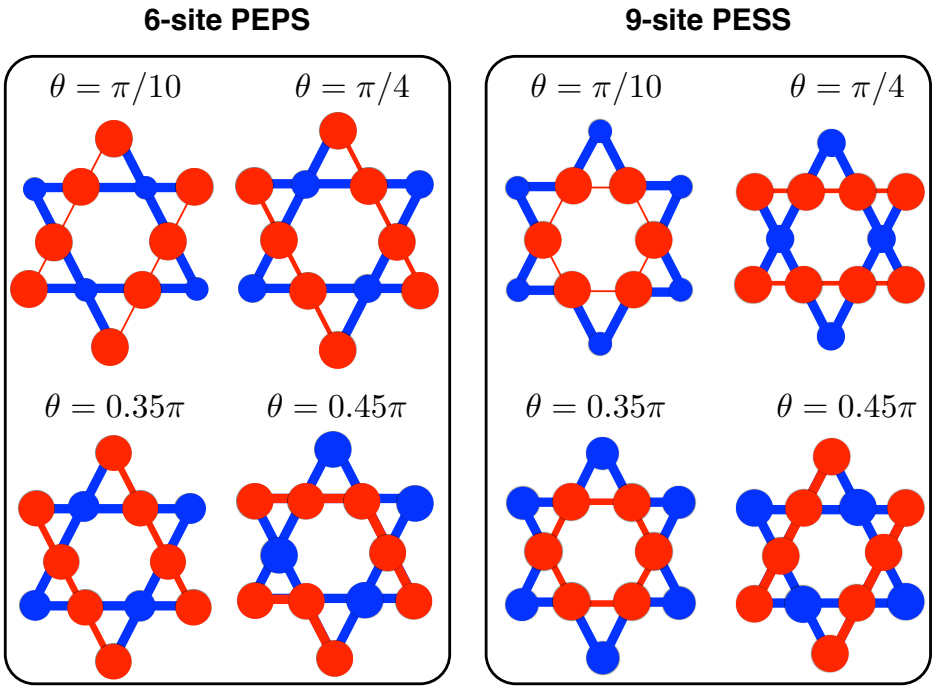

Figure 5.13: Magnetization (along the field) at every site and link energy terms $\langle h_{ij} \rangle$ at every link, for the coarse-grained approach with 6-site unit cell (6 different sites and 12 different links) (left) and the 9-site iPESS approach (9 different sites and 18 different links), and bond dimension $D = 3$, for several anisotropy angles. Red means positive, blue means negative, and the thickness indicates the magnitude in absolute value. We observe a clear competition between Nematic and Solid orders. For the 6-site PEPS we show Nematic for $\theta = \pi/10, \pi/4, 0.35\pi$ and 1×2 VBC-Solid for $\theta = 0.45\pi$. For the 9-site PESS we see degenerate Nematic and $\sqrt{3} \times \sqrt{3}$ VBC-Solid orders for all values of θ (see text). For illustration, Nematic (VBC-Solid) order is shown for $\theta = \pi/4, 0.45\pi$ ($\theta = \pi/10, 0.35\pi$). The approximate values (up to three significant digits) of the on-site magnetization and link energy terms are as follows: (i) for $\theta = \pi/10$: red link ≈ 0.067, blue link ≈ -0.232, red dot ≈ 0.653, blue dot ≈ -0.309 (same within these digits for both panels); (ii) for $\theta = \pi/4$: red link ≈ 0.127, blue link ≈ -0.245, red dot left ≈ 0.758, red dot right ≈ 0.736, blue dot ≈ -0.495 (same within these digits for both panels expect for the red dot); (iii) for $\theta = 0.35\pi$: red link ≈ 0.174, blue link ≈ -0.242, red dot ≈ 0.858, blue dot ≈ -0.710 (same within these digits for both panels); (iv) for $\theta = 0.45\pi$: red link ≈ 0.237, blue link ≈ -0.247, red dot ≈ 0.978, blue dot ≈ -0.956 (same within these digits for both panels).

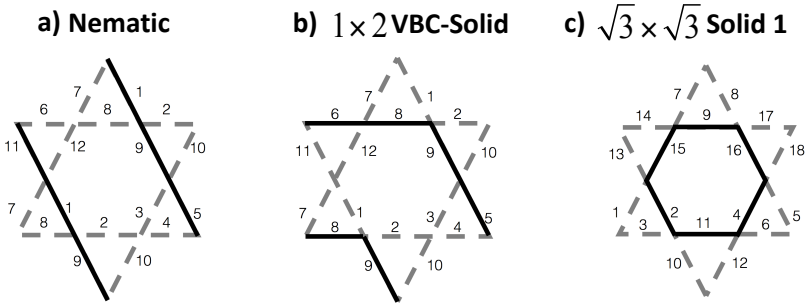

Figure 5.14: Different types of order in the kagome lattice, following the classification from Table 5.2: (a) Nematic, which breaks C_6-symmetry down to C_2 and is 3-fold degenerate; (b) 1×2 VBC-Solid, which breaks (i) C_6 symmetry completely, reflection-symmetry about one axis, and (ii) translation symmetry down to a 1×2 unit cell; (c) $\sqrt{3}\times\sqrt{3}$ Solid 1, which breaks translation symmetry down to a $\sqrt{3}\times\sqrt{3}$ unit cell. The first two structures in (a) and (b) can be accommodated in a 6-site unit cell, and (c) in a 9-site unit cell. To make this more evident, we show a possible labeling of the different links for such unit cells: 12 links for the 6-site, 18 for the 9-site.

the 6 and 12-site iPEPS approaches in favor of the Nematic order for XY anisotropy, in the vicinity of the Heisenberg point (with a typically relative energy difference of $\sim 0.1\%$ at the Heisenberg point) and for a small Ising anisotropy, and in favor of VBC-Solid order close to the Ising point. This is true even for the largest bond dimension we could reach. The stability of one phase with respect to the other is assessed when systematically obtaining the same one in different runs of our algorithms with different initial conditions. Thus, we see that there is no phase transition of the 1/3 magnetization plateaus as we go between different regimes of the XXZ model, rather we see a strong competition between Nematic and Solid orders both for the 9-site iPESS and the 6 and 12-site iPEPS algorithm for most values of the anisotropy angle. In order to have a clearer overview of how these phases look like for the different unit cells in the larger picture of the infinite kagome lattice, we give a representative diagram in Fig. 5.14. The numbering in the figure shows how the different links in the unit cell will get repeated in the entire kagome lattice. The first two structures in (a) and (b) can be accommodated in a 6-site unit cell and (c) in a 9-site unit cell. There are 12 different links for the 6-site and 18 for the 9-site.

Last but not the least, before concluding this chapter, we would like to discuss once again about the claim that the $m_z = 1/3$ plateau at the XY point could be a chiral spin liquid [198]. We have already seen using the two techniques that even the 1/3

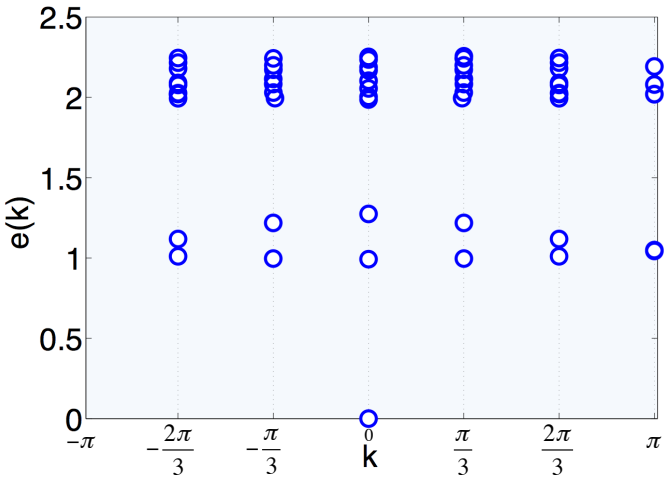

Figure 5.15: First 60 "entanglement energies" of the state at the $m_z = \frac{1}{3}$ plateau for the XY point, obtained by the 6-site iPEPS approach with $D = 3$. The partition corresponds to half an infinite cylinder with a width of 12 sites, and the cylinder contraction uses a 2-site periodicity as in Ref. [199]. The spectrum is symmetric in the momentum k in the transverse cylinder direction, and therefore the computed state is non-chiral.

plateau at the XY point is degenerate between the Nematic and Solid orders. Another check, that will add weight to our conclusion would be to compute the entanglement spectrum of the iPEPS wave function obtained from the 6-site iPEPS, for half an infinite cylinder of width 12, within the $m_z = 1/3$ plateau at the XY point. Details on how to compute the entanglement spectrum from the iPEPS wave function can be found in Ref. [199, 200]. For a chiral state, the entanglement spectrum should not be symmetric under time-reversal. However, we find that it is perfectly symmetric under time-reversal and therefore we do not find any further evidence for this state to be chiral. This is shown in Fig. 5.15. However, we would like to be careful about making any definitive conclusion on the chiral nature of this state. Indeed, it is possible that the state itself is not chiral but it is also possible that our iPEPS wave function need much higher bond dimension to see the chiral nature of this phase.

5.2.3 Comparing the two different techniques

Having plotted the phase diagram of our model and having found the exact nature of the ground state of the 1/3 plateaus using the different numerical techniques in different regimes of the model, we would like to see how the two techniques compare with each other from the energy point of view, for example. We have already seen

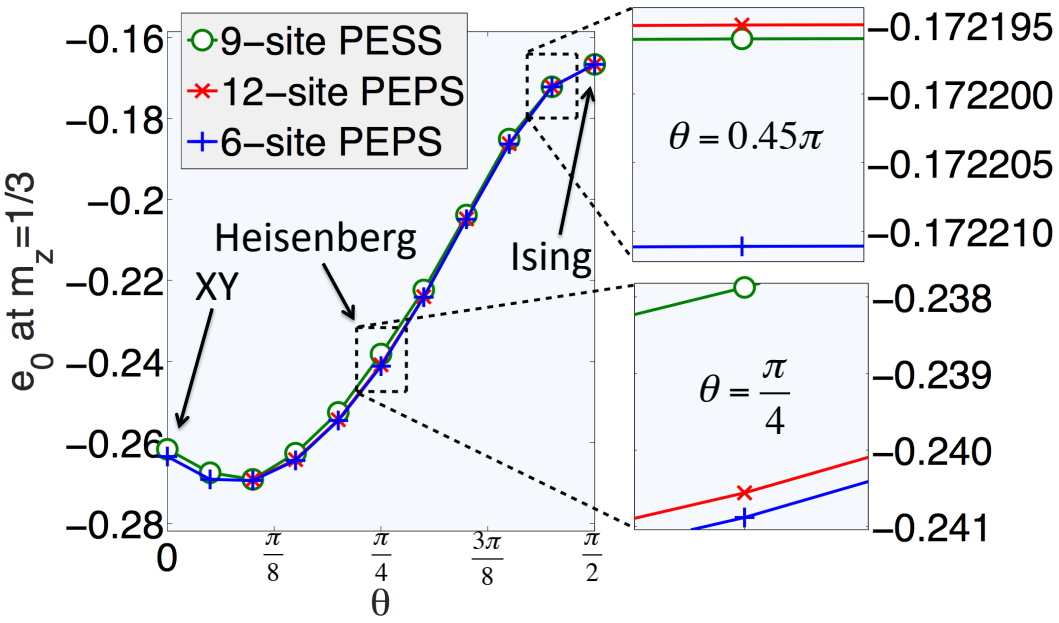

Figure 5.16: Comparison of the ground state energy per site e_0 without the Zeeman term at the $m_z = \frac{1}{3}$ plateau for different values of the anisotropy angle $\theta \in [0, \pi/2]$, for different approaches: (i) iPESS with 9-site unit cell, (ii) coarse-grained iPEPS with 6-site unit cell, and (iii) coarse-grained iPEPS with 12-site unit cell. The simulations are for $D = 3$ in all cases. The lowest variational energy is given by the coarse-grained iPEPS with 6-site unit cell. Higher bond dimensions in the iPEPS/iPESS lead to the same conclusions when compared on equal footing. The insets show zooms at the Heisenberg point $\theta = \pi/4$, for which the difference is relatively big, and for $\theta = 0.45\pi$ close to the Ising point, where the ground state is close to classical (in fact separable at the Ising point $\theta = \pi/2$) and therefore the energy differences are relatively small.

that the 9-site iPESS technique can find additional plateaus like 1/9, 5/9 and 7/9 while the 6 and 12-site iPEPS cannot because of the incommensurability of the unit cell with the expected magnetic structure. In order to compare the energies of the two techniques, we will compute the ground state energy per site. In order to compute the energy, we will use environment tensors which can be computed using the Corner Transfer Matrix (CTM) algorithm. It is worth noting that because the number of unit cells in each technique is different, one needs different CTM algorithms based on the periodicity of the ground state wave function. The comparison between the different techniques is shown in Fig. 5.16. In this figure, we show the ground state energy per site (excluding the magnetic field term) in the $m_z = \frac{1}{3}$ plateau phase as a function of the anisotropy angle θ, as computed with our three methods. We see that the 6-site approach is the one that produces the lowest variational energy. The

difference with the 9-site iPESS is around the third digit, roughly 1%, whereas the difference with the 12-site iPEPS is even smaller, around 0.1%. However, these small differences should be taken with caution, given the different approximations involved in the methods used. The fact that the 9-site iPESS approach produces higher energy may be a consequence of the smaller number of variational parameters in this ansatz. The quasi-degeneracy between the 6-site and the 12-site PEPS energies shows that a doubling of the unit cell is preferred over a quadrupling. From this, we learn that having lower energy is not enough while investigating such phases of matter but one also needs the right kind of unit cells that is commensurate with the expected magnetic structures of these phases.

5.3 Conclusions and outlook

In this chapter, we have introduced the concept of frustration in quantum systems. A system is said to be frustrated if the minimum of the total energy does not correspond to the minimum energy of each bond. A very popular example of such a system is the nearest-neighbor antiferromagnetic Ising model on a triangular lattice. Frustration is usually caused by the presence of different kinds of competing interactions in the system or the lattice geometry of the model. The kagome lattice is a highly frustrated system found in nature due to the presence of corner-sharing triangles. In this context, the spin-1/2 Kagome Heisenberg Antiferromagnet is one of the hardest problems in condensed matter physics because of its frustration and hence the large amounts of quantum fluctuations present in the system. Therefore, this system is very hard to study either numerically or analytically. The ground state of the KHAF is still a controversial issue in the field with some claiming it to be a Valence Bond Crystal and others claiming it to be a Quantum Spin Liquid. Such a quantum spin liquid has been proposed as a potential mechanism to explain high T_c superconductors. The main results of our investigation in this chapter are summarized below.

- We have studied the ground state of the Kagome Heisenberg Antiferromagnet using our Tensor Network techniques i.e. iPEPS specifically. We did this by mapping three spins in the kagome lattice to a single site in the square lattice and using the usual iPEPS algorithm with a 2-site unit cell, thus in turn, allowing a 6-site unit cell in the original kagome lattice.

- We have seen that our technique offers a good competition to the existing numerical techniques based on the ground state energy per site of this model.

Using our technique, we do not find evidence of a quantum spin liquid as the ground state, rather what we find is a valence bond crystal. However, there is so much scope in pushing our computational efforts and this is something we would like to do in the future.

- Introducing an external magnetic field to such a model can give rise to magnetization plateaus at specific values of the magnetization. We have also investigated the existence and presence of such magnetization plateaus for the general antiferromagnetic XXZ model in the kagome lattice of which the KHAF is just a point in the phase diagram. This was done using two techniques: (i) a 9-site iPESS technique (which is a variation of the usual iPEPS technique) and (ii) a 6 and 12-site iPEPS technique (which was obtained by coarse-graining three spins in the kagome lattice to a single site in the square lattice with a 2 and 4-site unit cell).

- Using these two techniques, we confirmed the existence of the controversial $m_z = 1/3$ plateau and found no evidence of it to be a chiral spin liquid using our iPEPS approximation at the XY point. We also found additional plateaus such as 1/9, 5/9 and 7/9 using the 9-site iPESS but did not find them using the 6 and 12-site iPEPS.

- Specifically, we studied the 1/3 plateau in different regimes of the XXZ model such as the XY, Heisenberg and the Ising point. We found that these plateaus do not undergo any phase transition as we move between different regimes of our model. Rather, what we find is that these plateaus are degenerate in Nematic and Solid 1 order with the 9-site iPESS technique and Nematic and Valence Bond Crystal Solid with the 6 and 12-site iPEPS technique. This degeneracy seems to be slightly lifted in the 6 and 12-site iPEPS technique in favor of the Nematic order for XY anisotropy, in the vicinity of Heisenberg point and for a small Ising anisotropy and in favor of a Valence Bond Crystal Solid close to the Ising point.

- We also compared the two techniques by computing the ground state energies of the 1/3 plateaus. We found that the 6-site technique gives us lower energy (around 1%) than the 9-site technique because it has a higher effective bond dimension and hence able to handle more entanglement in the system. The 12-site unit cell has a slightly higher energy then the 6-site unit cell (around 0.1%).

Indeed, it remains to be seen what happens to the phase diagram of the model for higher spins such as $S = 1, 3/2, 2$, etc and the emergence of the different plateaus therein. It also remains to be seen if the non-chiral nature of the 1/3 plateau in the XY point is due to low bond dimension of the iPEPS or indeed if the state is not chiral anyways. For this, one needs to use iPEPS with a very large bond dimension. This computational bottleneck can be improved by implementing symmetries for example in our TN algorithms. One can also think of using faster and more efficient matrix decomposition techniques and GPUs for computations. Recently, it has been shown that PEPS can be used to realize chiral topological order by explicitly constructing chiral PEPS [201] but it still remains to be seen if such a state can be realized numerically from a chiral Hamiltonian.

Chapter 6

Open Dissipative Quantum Systems

In the previous chapters, we discussed Symmetry Protected Topological (trivial) and other exotic phases of matter arising out of frustration in a quantum system. We mainly studied their ground state properties while assuming that the system is perfectly isolated from the rest of the environment. In reality, no system can be completely isolated from its environment. By 'system', we mean anything that is under our observation and by 'environment', we mean anything that is not a part of our system. The environment could, thus, be the rest of the laboratory, the rest of the universe or even beyond. Because it is often so difficult to study the entire 'system + environment', usually we neglect the effects of the environment and consider only the system. We then have what is known as a 'closed system'. However, all systems in nature, as expected, are not isolated and cannot be described by a pure state. We therefore need to include the environment for a complete description of the system. The system is then said to be open. In this case, the mixed states are denoted by a density matrix ρ instead of a wave function $|\psi\rangle$ which are used for pure states. We have already discussed in detail the notion of pure and mixed states in Chapter 2 of the thesis. Examples of systems interacting with environment include heat transfer, quantum decoherence, etc. The process of exchange of information (i.e. energy, particles, etc) between system and environment usually leads to dissipation. Dissipation can lead to different kinds of dynamics in open quantum system. One such dynamics is the Markovian evolution. In this, we assume that the evolution has no memory i.e. it does not depend on the history of the system. One can give a formal definition of Markovian evolution as follows: A dynamics is said to be of Markovian nature if the state $\rho(t + \delta t)$ only depends on the state of the system immediately before i.e. $\rho(t)$ for an infinitesimal δt. In other words, the evolution of a system cannot depend on

(a) the state of the environment and (b) the state $\rho(t')$ for some $t' < t$. An example of such an evolution would be the spontaneous emission of a photon from an atomic system where the photons are not reabsorbed by the atom (i.e. information does not flow back into the system). On the other hand, there can be non-Markovian evolution where the system possesses some sort of memory during the evolution. Let us not go too much into the details of non-Markovian dynamics as we are only interested in the former kind in this thesis. Aspects on non-Markovian dynamics using Tensor Network States would be an interesting field in the future though.

In the context of quantum many-body systems, dissipation often leads to many interesting physics such as decoherence of complex wave functions [202], quantum thermodynamics [203], engineering topological order [18], driven dissipative universal quantum computation and dissipative phase transitions [19], etc all of which are being intensely studied at the moment. Despite their obvious importance, understanding the effects of dissipation in quantum many-body systems continues to be a very difficult problem. This is mainly because of two reasons. First, open quantum systems exhibit the same complexity class as equilibrium systems i.e. the number of parameters required to describe such systems scales exponentially with the system size [1]. Second, there are physical constraints on the density matrix which can be used to represent them such as positivity, hermiticity and trace one. For example, it has been shown that checking the positivity of a Matrix Product Operator (which can be used to represent a density matrix) in the thermodynamic limit is a computationally intractable problem [204]. Because of these reasons, efficient numerical tools for the study of open quantum many-body systems are quite rare and continue to remain a challenge.

In this chapter, we present a numerical method which can be used to study such open dissipative quantum systems in 2D lattices of infinite size (i.e. in the thermodynamic limit). The method that we propose here is based on Tensor Networks and is, in fact, particularly simple and efficient, as well as the first approach that uses TNs to target 2D dissipation. To probe the validity of our algorithm, we investigate the dissipative 2D quantum Ising model for spin-1/2, which is of relevance for controversies concerning dissipation for interacting Rydberg atoms [205]. We will compare our results with those obtained by a variational algorithm based on a product and a correlated ansatz [206]. We will also investigate a spin-1/2 XYZ model to address some controversies regarding its phase diagram. Before getting into the details of our

[1] As a matter of fact, it scales as $O(d^{2N})$ where d is the physical dimension of a particle and N is the number of particles. So it is even worse then systems in equilibrium which scales as $O(d^N)$.

technique, let us go through some of the recent developments in TN algorithms for studying open quantum systems in 1D. This chapter is based on the paper [207] by the author which has been accepted for publication.

6.1 Recent developments in TN for open systems

As we have seen, open quantum systems are described by mixed states $\rho(t)$. For Markovian systems, the evolution is generated by a Liouvillian operator $\mathcal{L}$, and can be cast in the form of a master equation for the reduced density matrix of the quantum system. The master equation has the following form

$$\begin{aligned}\frac{d}{dt}\rho &= \mathcal{L}[\rho] \\ &= -i\,[H,\rho] + \sum_{\mu}\left(L_\mu \rho L_\mu^\dagger - \frac{1}{2}L_\mu^\dagger L_\mu \rho - \frac{1}{2}\rho L_\mu^\dagger L_\mu\right),\end{aligned} \tag{6.1}$$

where ρ is the density matrix of the system, $\mathcal{L}$ is the Liouvillian superoperator, H the Hamiltonian of the system, and $\{L_\mu, L_\mu^\dagger\}$ are the Lindblad operators responsible for the dissipation, also known as the jump operators.

In 2004, Verstraete *et al* [67] introduced the concept of Matrix Product Density Operator (MPDO) which extended the Matrix Product States (MPS) formalism from pure to mixed states. Let us recall that an MPS can be written in the following form

$$|\psi\rangle = \sum_{s_1,\ldots,s_N=1}^{d} A_1^{s_1}\ldots A_N^{s_N}|s_1,\ldots,s_N\rangle \tag{6.2}$$

where the A's are matrices whose dimension is bounded by some fixed number D and d is the physical dimension of the Hilbert space. An MPDO ρ of N d-level particles with $(D_1, D_2, \ldots, D_N)$-dimensional bonds were then defined as

$$\rho = \sum_{s_1,s_1',\ldots,s_N,s_N'=1}^{d} (M_1^{s_1,s_1'}\ldots M_N^{s_N,s_N'})|s_1,\ldots,s_N\rangle \times \langle s_1',\ldots,s_N'|, \tag{6.3}$$

where $M_k^{s_k,s_k'}$ are $D_k^2 \times D_{k+1}^2$ matrices that can be decomposed as

$$M_k^{s,s'} = \sum_{a=1}^{d_k} A_k^{s,a} \otimes (A_k^{s',a})^*. \tag{6.4}$$

where d_k is at most dD_kD_{k+1} and the matrices $A_k^{s,k}$ are of size $D_k \times D_{k+1}$. Such construction of MPDOs automatically ensures the positivity of the reduced density

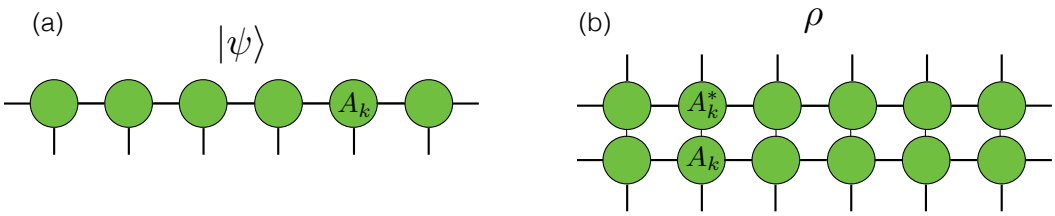

Figure 6.1: (a) Writing a wave function $|\psi\rangle$ as an MPS for 6 sites. Each site has a physical dimension d. (b) A density matrix ρ can be written as an MPDO, an extension of the MPS formalism. Such a construction automatically ensures positivity of the density matrix.

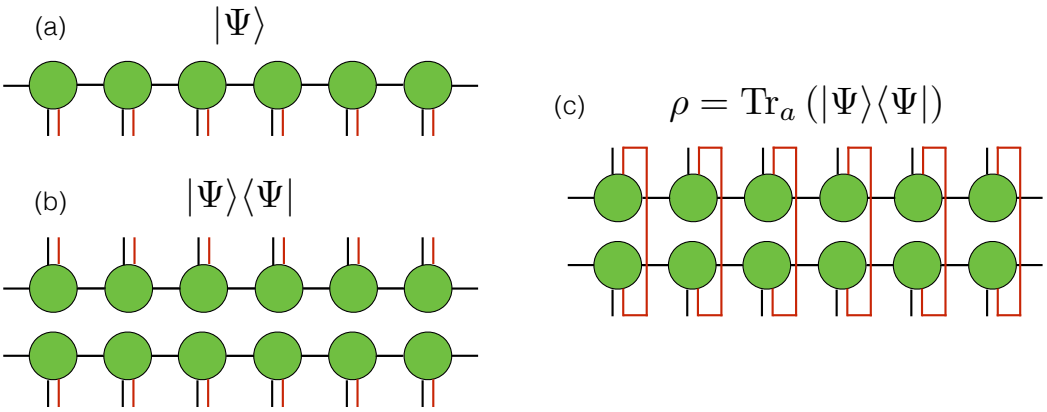

Figure 6.2: (a) Defining an MPS $|\Psi\rangle$ over the enlarged Hilbert space using ancilas (in red) (b) Taking the projector of the MPS with ancillas (c) Tracing out the ancillas from the projector to obtain the MPDO ρ.

matrix ρ. This is shown in Fig. 6.1. This MPDO can be expressed in terms of a pure state MPS by defining it over a larger Hilbert space and using the concept of purification [208]. This can be done by associating an ancilla with a Hilbert space of dimension d_k with each physical system. One can then choose an orthonormal basis $|s_k, a_k\rangle$ for these physical and ancilla indices. The corresponding MPS for this system can be written as

$$|\Psi\rangle = \sum_{s_1,\ldots,s_N} \sum_{a_1,\ldots,a_N} A_1^{s_1,a_1} \ldots A_N^{s_N,a_N} |s_1 a_1, \ldots, s_N a_N\rangle \tag{6.5}$$

The MPDO ρ can be obtained by tracing over the ancillas i.e. $\rho = \mathrm{Tr}_a\left(|\Psi\rangle\langle\Psi|\right)$. This process is illustrated in Fig. 6.2. The original A_k matrices can be recovered from M_k by doing some eigenvalue decomposition. To determine the evolution of a

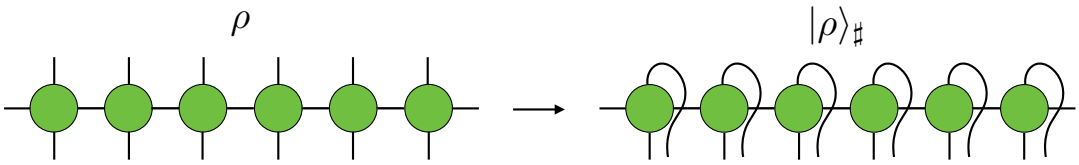

Figure 6.3: Choi isomorphism: vectorizing a density matrix written in terms of an MPO. In TN diagram, it is simply reshaping one of the indices and gluing it with the other thereby giving us an MPS.

Hamiltonian of a mixed state in real and imaginary time, they simply simulated the evolution of the purification by updating the A_k matrices using an iterative procedure similar to the standard DMRG in this technique. The purification could then be used to reconstruct the density operator at any time and compute the expectation values of the observables. Although the MPDOs in Ref. [67] are positive by construction, it was shown in Ref. [209] that such MPDO description of the mixed states are not exactly equivalent to the one obtained using local purification schemes. In particular, it was shown that the bond dimension of the locally purified MPS D' is not upper bounded by the bond dimension of the MPDO D. In fact, the local purification techniques can be much more costly than the MPDO form itself. Thus, they concluded that a description of mixed states which is both efficient and locally positive semi definite does not exist and that one can only make approximations.

Around the same time, Zwolak and Vidal [68] proposed another technique to study the mixed state dynamics in one dimensional lattice systems. Their technique, which is also based on TNs, used the Time Evolving Block Decimation (TEBD) to simulate the real time Markovian dynamics given by a master equation with nearest-neighbor couplings. At the heart of this algorithm, lies the concept of 'Choi isomorphism'. It is more of a mathematical trick and it states that one can rewrite the coefficients of a matrix as those of a vector. In other words, this is simply turning a bra index into a ket index for a density matrix (understanding the coefficients of ρ as those of a vectorized density matrix denoted by $|\rho\rangle_\sharp$). And in the language of TN diagrams, it can be regarded as reshaping one of the legs and gluing it with the other (Fig. 6.3). Once vectorized, $|\rho\rangle_\sharp$ now lives in the n-fold tensor product of $\mathbb{C}_{d^2}$ and the master equation can be written in the vector form. The mixed state will now look like as

follows

$$|\rho\rangle_\sharp = \sum_{i_1=0}^{d^2-1} \cdots \sum_{i_N=0}^{d^2-1} c_{i_1 \cdots i_N} |i_1\rangle_\sharp \otimes \cdots \otimes |i_N\rangle_\sharp. \tag{6.6}$$

where $|i_l\rangle_\sharp$ is an orthonormal basis of $\mathbb{C}_{d^2}$ for site l. Further assuming that the Liouvillian superoperator $\mathcal{L}$ can be decomposed into terms involving at most nearest-neighbors i.e. $\mathcal{L}[\rho] = \sum_l \mathcal{L}_{l,l+1}[\rho]$, one could in principle use the usual TEBD algorithm to solve Eq. 6.1 by starting from some initial Matrix Product Operator (MPO) (shown in in the left side of Fig. 6.3). This was the basic idea behind the technique in Ref. [68]. Although the technique proved to be extremely simple and efficient, the issue of positivity still remained at large. In fact, checking the positivity of a reduced density matrix is known to be a very hard problem in physics [204].

Another approach was taken in Ref. [210] to solve the problem of positivity. In this approach, instead of expressing ρ directly as an MPO, at every stage of the algorithm, ρ was kept in its locally purified $\rho = XX^\dagger$, where the purification operator X is decomposed as a variational tensor network.

$$[X]^{s_1,\ldots,s_N}_{r_1,\ldots,r_N} = \sum_{m_1,\ldots,m_{N-1}} A^{[1]s_1,r_1}_{m_1} A^{[2]s_2,r_2}_{m_1,m_2} \ldots A^{[N]s_N,r_N}_{m_{N-1}} \tag{6.7}$$

where $1 \leq s_l \leq d$, $1 \leq r_l \leq K$ and $1 \leq m_l \leq D$. $A^{[l]}$ are rank-four tensors with physical dimension d, bond dimension D and Kraus dimension K. Then, a technique similar to the usual TEBD was used to update the tensors. Such an approach never required to contract the two TN layers (X and $X^\dagger$) together, thereby ensuring positivity at all times.

In Ref. [211], a very interesting approach based on MPO was taken for finding the steady states of dissipative 1D systems governed by the master equation of the Lindbladian form, $\frac{d\rho}{dt} = \mathcal{L}[\rho]$, where $\mathcal{L}$ is the Liouvillian superoperator. In this technique, instead of doing the full real time evolution of the Liouvillian, they proposed a variational method that searches for the null eigenvector of $\mathcal{L}$ which is, by definition, the steady state of the master equation in the Lindbladian form. Their results were based on the principle that if ρ_s is the steady state of the Lindbladian master equation satisfying $\hat{\mathcal{L}}|\rho_s\rangle_\sharp = 0$, then $|\rho_s\rangle_\sharp$ will also be the ground state of the non-local Hamiltonian $\hat{\mathcal{L}}^\dagger\hat{\mathcal{L}}$ (since it is Hermitian and positive semi-definite) where $|\rho_s\rangle_\sharp$ is the vectorized form of the steady state density matrix. Then using a variational algorithm, they directly targeted the ground state of $\hat{\mathcal{L}}^\dagger\hat{\mathcal{L}}$ to find the steady state of the Lindbladian master equation for a finite chain. One of the reasons why directly targeting the ground state of $\hat{\mathcal{L}}^\dagger\hat{\mathcal{L}}$ might be advantageous is that unlike imaginary

time evolution, where the sequence of states visited by the algorithm is unimportant, the simulation of a master equation requires us to follow real time evolution. Therefore, if there are errors in the intermediate states visited by the algorithm, it may lead to problems in the convergence of our steady state. For example, some of the intermediate states may require large bond dimensions of the MPO although it is known that the final steady state can be well-represented by an MPO of small bond dimensions [212, 213]. A very similar approach was taken in Ref. [214] where the algorithm instead of doing a time-evolution, searched for the null eigenvalue of the Liouvillian superoperator $\mathcal{L}$ by sweeping along the system. Their method claimed to work even in the weakly dissipative regime by slowly tuning the dissipation rates along the sweeps. In another paper [215], this idea was applied to infinite 1D systems (i.e. the thermodynamic limit) using a hybrid technique of both imaginary and real time evolution. They took a local auxiliary Hamiltonian $\mathcal{H}$ whose ground state is a good approximation to the ground state of the nonlocal Hamiltonian $\hat{\mathcal{L}}^\dagger\hat{\mathcal{L}}$ by taking its k^{th} root as

$$\mathcal{H} = \sum_{r\in\mathbb{Z}} (\hat{\mathcal{L}}_r^\dagger \hat{\mathcal{L}}_r)^{1/k} \tag{6.8}$$

where $\hat{\mathcal{L}} = \sum_{r\in\mathbb{Z}} \hat{\mathcal{L}}_r$ since $\hat{\mathcal{L}}$ is a translationally invariant local operator. The k^{th} root was taken in order to yield faster convergence. The idea is that if the gap between the two lowest eigenvalues of $\hat{\mathcal{L}}_r^\dagger\hat{\mathcal{L}}_r$ is less than one, then $k > 1$ will increase the gap since $\hat{\mathcal{L}}_r^\dagger\hat{\mathcal{L}}_r$ is positive semi definite, thereby achieving faster convergence to the ground state.

In the next section, we will discuss how to extend the above ideas for the case of 2D lattice systems in the thermodynamic limit. We will propose a simple TN algorithm based on iPEPS to target the steady state of a dissipative Markovian system governed by the Lindbladian master equation. So far, to the best of our knowledge, our technique is the first TN application of 2D steady states. There are some other techniques which are not based on TNs such as the variational ansatz technique [206] which approximates the steady state by minimizing a suitable norm of the full quantum master equation. Besides, there are other techniques based on Mean Field [216] and Cluster Mean Field [217] approaches. However, these approaches do not take into account the correlations present in the system. There is also this Corner Space Renormalization method [218] that solves the master equation in a corner of the Hilbert space through an iterative procedure. This technique also does not take into account the true 2D correlations present in the system. We will not go into the details of these techniques and instead jump directly into our problem.

6.2 Application in 2D dissipative systems

As we have seen, the vectorized form of the Lindbladian Eq. 6.1 can be written as

$$\frac{d}{dt}|\rho\rangle_\sharp = \mathcal{L}_\sharp|\rho\rangle_\sharp \tag{6.9}$$

where the vectorized Liouvillian operator is given by

$$\begin{aligned}\mathcal{L}_\sharp \equiv & -i\left(H\otimes\mathbb{1}-\mathbb{1}\otimes H^T\right)\\ & +\sum_\mu\left(L_\mu\otimes L_\mu^*-\frac{1}{2}L_\mu^\dagger L_\mu\otimes\mathbb{1}-\frac{1}{2}\mathbb{1}\otimes L_\mu^* L_\mu^T\right).\end{aligned} \tag{6.10}$$

In the above equation, the symbol of tensor product $\otimes$ separates operators acting on either the l.h.s. (ket) or the r.h.s. (bra) of ρ in its matrix form. Whenever $\mathcal{L}_\sharp$ is independent of time, Eq. 6.9 can be formally integrated as

$$|\rho(T)\rangle_\sharp = e^{T\mathcal{L}_\sharp}|\rho(0)\rangle_\sharp, \tag{6.11}$$

which for very large times T may yield a steady state

$$|\rho_s\rangle_\sharp \equiv \lim_{T\to\infty}|\rho(T)\rangle_\sharp. \tag{6.12}$$

From the above equations, is easy to see that the state $|\rho_s\rangle_\sharp$ is the right eigenvector of $\mathcal{L}_\sharp$ corresponding to zero eigenvalue, so that

$$\mathcal{L}_\sharp|\rho_s\rangle_\sharp = 0. \tag{6.13}$$

Next, let us consider the special but quite common case in which the Liouvillian $\mathcal{L}$ can be decomposed as a sum of local operators. For nearest-neighbor terms, one has the generic form $\mathcal{L}[\rho] = \sum_{\langle i,j\rangle}\mathcal{L}^{[i,j]}[\rho]$, where the sum $\langle i,j\rangle$ runs over nearest-neighbors. In the "vectorized" notation ($\sharp$), this means that $\mathcal{L}_\sharp = \sum_{\langle i,j\rangle}\mathcal{L}_\sharp^{[i,j]}$.

The combination of the expressions above yields a parallelism with the calculation of ground states of local Hamiltonians by imaginary time evolution, which we detail in Table 6.1. Given this parallelism, it is clear that one can adapt, at least in principle, the methods to compute imaginary time evolution of a pure state as generated by local Hamiltonians, to compute also the real time evolution of a mixed state as generated by local Liouvillians. This was, in fact, the approach taken in Ref. [68] for finite-size 1D systems, using Matrix Product Operators (MPO) to describe the 1D reduced density matrix, and proceeding as in the Time Evolving Block Decimation (TEBD) algorithm for ground states of 1D local Hamiltonians [77, 78] as we have discussed previously. Inspired by this, our method for 2D systems proceeds by representing the reduced

Ground states	Steady states
$H = \sum_{\langle i,j \rangle} h^{[i,j]}$	$\mathcal{L}_\sharp = \sum_{\langle i,j \rangle} \mathcal{L}_\sharp^{[i,j]}$
e^{-TH}	$e^{T\mathcal{L}_\sharp}$
$\|e_0\rangle$	$\|\rho_s\rangle_\sharp$
$\langle e_0\|H\|e_0\rangle = e_0$	${}_\sharp\langle\rho_s\|\mathcal{L}_\sharp\|\rho_s\rangle_\sharp = 0$
Imaginary time	Real time

Table 6.1: Parallelism between the calculation of ground states by imaginary time evolution, and the calculation of steady states by real time evolution. On the left hand side, H is a Hamiltonian that decomposes as a sum of local terms $h^{[i,j]}$, $|e_0\rangle$ is the ground state of H with eigenvalue e_0, and T is the imaginary time. The terms on the right hand side have been explained in the text.

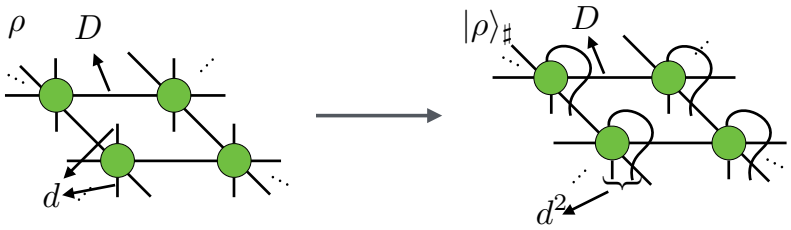

Figure 6.4: TN diagram for the PEPO for ρ on a 2D square lattice, with bond dimension D and physical dimension d. When vectorized, it can be understood as a PEPS for $|\rho\rangle_\sharp$ with physical dimension d^2.

density operator ρ by a Projected Entangled Pair Operator (PEPO) [2] with physical dimension d and bond dimension D, see Fig. 6.4 (left). Such a construction does not guarantee the positivity of the reduced density matrix. However, we shall see later that this lack of exact positivity is not too problematic in our numerical simulations. Once vectorized, the PEPO can be understood as a Projected Entangled Pair State (PEPS) of physical dimension d^2 and bond dimension D, as shown also in Fig. 6.4 (right). Next, we notice that for the case of an infinite size 2D system, this setting is actually equivalent to that of the iPEPS algorithm to compute ground states of local Hamiltonians in 2D in the thermodynamic limit. Thus, in principle, we can use the full machinery of iPEPS to tackle as well the problem of 2D dissipation and steady states. There seems to be, however, one problem with this idea: unlike in imaginary time evolution, we are now dealing with real time. In the master equation, part of the evolution is generated by a Hamiltonian H, and part by the Lindblad operators L_μ.

[2] Projected Entangled Pair Operators are simply the operator version of Projected Entangled Pair States (PEPS), in the same way that Matrix Product Operator (MPO) are the operator version of Matrix Product States (MPS) for the 1D case.

The Hamiltonian part corresponds actually to a unitary "Schrödinger-like" evolution in real time, which typically increases the "operator-entanglement" in $|\rho\rangle_\sharp$, up to a point where it may be too large to handle for a TN representation (e.g., 1D MPO or 2D PEPO) with a reasonable bond dimension. Luckily, this is not a dead-end: if the dissipation is strong compared to the rate of entanglement growth, then the evolution drives the system into the steady state before hitting a large entanglement region. Here we show that, quite surprisingly, this is indeed the case for 2D dissipative systems. Thus, in principle, the stronger the dissipation, the better our algorithm should be. We will show this by computing what we call the operator-entanglement entropy which is defined as follows

$$S_{op}(\rho) \equiv -\mathrm{tr}_E\left(\sigma_\sharp \log \sigma_\sharp\right), \tag{6.14}$$

where $\sigma_\sharp \equiv \mathrm{tr}_E\left(|\rho\rangle_\sharp\ {}_\sharp\langle\rho|\right)$, $|\rho\rangle_\sharp$ is the vectorized reduced density matrix and tr_E is the partial trace over the sites for which we wish to compute the entropy. In a nutshell: this is the entanglement entropy of $|\rho\rangle_\sharp$, the vectorized density matrix, understood as a pure state. This is the relevant measure of correlations for our purposes, since it is upper-bounded directly by the bond dimension of the PEPO. Namely, if the PEPO has bond dimension D, then for a block of $L \times L$ sites one has

$$S_{op}(\rho) \leq 4L \log D, \tag{6.15}$$

which means that we can use it to quantify how large needs to be our bond dimension D for the PEPO, being this directly connected to the computational cost and the accuracy of the method [219]. Details on how to compute this quantity is shown in Appendix C of the thesis. In the next section, we have shown a figure showing how increasing the dissipation strength in the spin-1/2 Ising model lowers the operator-entanglement entropy (which never exceeds the support of the PEPO) and therefore improves the performance of our algorithm. Regarding settings where dissipation is not so strong, our algorithm could be a good starting point to compute steady states in the strong-dissipation regime. The strength of the dissipation can then be lowered down adiabatically, and using as initial state the one pre-computed for slightly-stronger dissipation. In this way one may get rid of local minima and obtain good results also in the weak dissipation regime. However, this is only an intuitive guess and we have not tested it explicitly.

With this in mind, our algorithm just applies the iPEPS machinery to compute the time evolution in 2D with a local Liouvillian $\mathcal{L}$ and some initial state. For the examples shown in this thesis, we use the so-called simple update scheme [181]

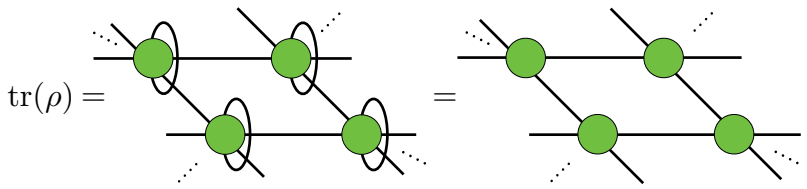

Figure 6.5: The trace of ρ maps to the contraction of a 2D TN.

for the time evolution of the PEPO, Corner Transfer Matrices (CTM) [51] for the calculation of observables and random initial states. To check whether we have a good approximation of a steady state or not, we compute the parameter

$$\Delta \equiv {}_\sharp\langle \rho_s | \mathcal{L}_\sharp | \rho_s \rangle_\sharp \tag{6.16}$$

For a good steady state approximation, this parameter should be close enough to zero, since we have $\Delta = 0$ in the exact case. Another quantity that we used to check the validity of the simulations is the sum of negative eigenvalues of the (numerical) reduced density matrices of the system. More precisely, we define

$$\epsilon_n \equiv \sum_{i|\nu_i<0} \nu_i \left(\rho_n\right) \tag{6.17}$$

where ρ_n is the reduced density matrix of n contiguous spins in the steady state and $\nu_i(\rho_n)$ its eigenvalues, with only the negative ones entering the sum. In an exact case, this quantity should be equal to zero. However, the different approximations in the method may produce a small negative part in ρ_s, which can be easily quantified in this way. It is worth mentioning as a word of caution: notice that Δ and ϵ_n can be used to benchmark our calculations, but they do not characterize the distance to the steady state.

The computational cost of this algorithm is the one of the chosen iPEPS strategy. In our case, we work with a simple update for the evolution with a 2-site unit cell, which has a cost of $O(d^4D^5 + d^{12}D^3)$, and Trotter time steps $\delta t = 0.1 - 0.01$. Moreover, the CTM method for expectation values is essentially the one used to approximate classical partition functions on a 2D lattice (see Fig. 6.5), which has a cost of $O(dD^4 + \chi^2 D^4 + \chi^3 D^3)$, χ being the CTM bond dimension. The overall approach is remarkably efficient. To have an idea of how efficient this is, let us imagine the following alternative strategy: we consider the Hermitian and positive semi definite operator $\mathcal{L}_\sharp^\dagger \mathcal{L}_\sharp$, and target $|\rho\rangle_\sharp$ as its ground state. This ground state could be

computed, e.g., by an imaginary time evolution. The problem, however, is that the crossed products in $\mathcal{L}_\sharp^\dagger \mathcal{L}_\sharp$ are nonlocal, and therefore the usual algorithms for time evolution are difficult to implement unless one introduces extra approximations in the range of the crossed terms [215]. Another option is to approximate the ground state variationally, e.g., via the Density Matrix Renormalization Group [45, 46] or similar approaches [220, 211] in 1D, or variational PEPS in 2D [80]. In the thermodynamic limit, however, this approach does not look very promising because of the nonlocality of $\mathcal{L}_\sharp^\dagger \mathcal{L}_\sharp$ mentioned before. In any case, one could always represent this operator as a PEPO (in 2D), which would simplify some of the calculations, but at the cost of introducing a very large bond dimension in the representation of $\mathcal{L}_\sharp^\dagger \mathcal{L}_\sharp$. For instance, if a typical PEPO bond dimension for $\mathcal{L}_\sharp$ is ~ 4, then for $\mathcal{L}_\sharp^\dagger \mathcal{L}_\sharp$ it is ~ 16, which in 2D implies extremely slow calculations. Another option would be to target the variational minimization of the real part for the expectation value of $\mathcal{L}$ [220]. This option, however, is also dangerous in 2D because of the presence of many local minima. Additionally, the correct norm to perform all these optimizations is the one-norm of $\mathcal{L}(\rho)$ which, in contrast to the more usual 2-norm, is a hard figure of merit to optimize with variational TN methods. The use of real-time evolution is thus a safer choice in the context of the approximation of 2D steady states. We will now demonstrate our algorithm by applying it to a spin-1/2 dissipative Ising model and later to the XYZ model in a square lattice.

6.2.1 The Ising model

Having described our algorithm in detail, let us now use it to benchmark against some existing methods and results. For this, we will first simulate a dissipative spin-1/2 quantum Ising model on an infinite 2D square lattice where dissipation pumps one of the spin states into the other. This model has also received considerable interest lately because it can be realized experimentally using ultracold Rydberg atoms [221, 222]. Moreover, the phase diagram of its non-equilibrium steady state is still a matter of controversy. Initially, it was predicted that the model exhibits a bistable phase [223, 224], but several numerical and analytical calculations have cast doubts on this claim and predict instead a first order transition. In particular, a variational approach [205, 206] predict that the bistable phase is replaced by a first order transition which is also supported by arguments derived from a field-theoretical treatment of related models within the Keldysh formalism [225]. Furthermore, it is an open question whether the model supports an antiferromagnetic phase [223, 226,

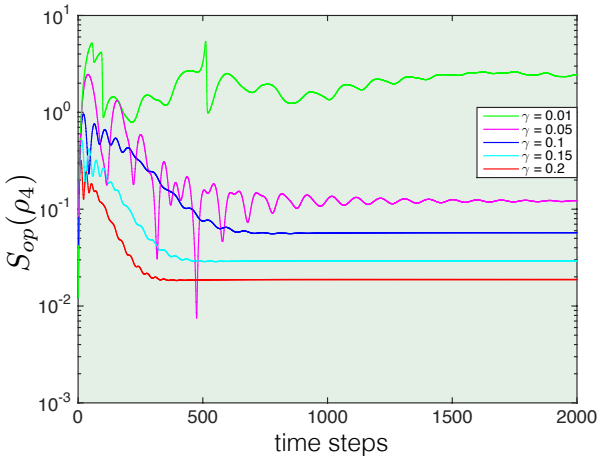

Figure 6.6: Operator-entanglement entropy throughout the evolution for a block of 2×2 unit cell with $D = 2$, $V = 0.5$, $h_x/\gamma = 10$, and different values of γ. The stronger the dissipation, the weaker the entanglement. A similar behavior is observed for larger D.

227, 205, 206]. The master equation of this model follows the one in Eq. 6.1, where the Hamiltonian part is given by

$$H = \frac{V}{4} \sum_{\langle i,j \rangle} \sigma_z^{[i]} \sigma_z^{[j]} + \frac{h_x}{2} \sum_i \sigma_x^{[i]} + \frac{h_z}{2} \sum_i \sigma_z^{[i]} \tag{6.18}$$

with $\sigma_\alpha^{[i]}$ the α-Pauli matrix at site i, V the interaction strength, h_x, h_z the transverse and parallel fields respectively, and where the sum over $\langle i,j \rangle$ runs over nearest-neighbors. The dissipative part is given by the operators $L_\mu = \sqrt{\gamma}\sigma_-^{[\mu]}$, so that in this particular case μ is a site index, and where σ_- is the usual spin-lowering operator.

In our simulations, we first set $V = 5\gamma, \gamma = 0.1, h_z = 0$ in order to compare with the results in Ref. [206], which uses a correlated variational ansatz with states of the form $\rho = \prod_i \rho_i + \sum_{\langle ij \rangle} C_{ij} \prod_{k \neq ij} \rho_k$, where ρ_i are single site density matrices and C_{ij} account for correlations. Before going to the phase diagram of the model, let us first probe the growth of the operator-entanglement entropy S_{op} as we discussed in the previous section for the given dissipation strength. This is shown in Fig. 6.6. Thus, one can see that the growth of entanglement gets killed in the presence of strong dissipation and drives the evolution to its steady state. We will study the phase diagram of the parameters for the blue plot in Fig. 6.6 i.e. when $\gamma = 0.1$. We now compute the density of spins-up $n_\uparrow \equiv \sum_{i=1}^N \langle (1 + \sigma_z^{[i]}) \rangle / 2N$ (N is the system's size) as a function of h_x/γ, for which it is believed to exist a first order transition in the steady state from a "lattice gas" to a "lattice liquid". This transition is clearly

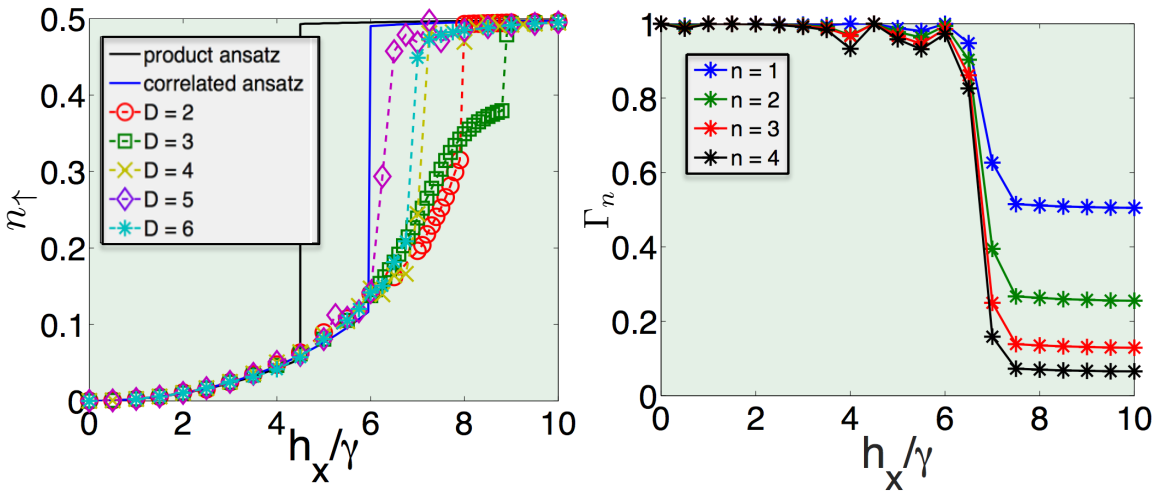

Figure 6.7: Non-equilibrium steady state phase diagram of the quantum dissipative spin-1/2 Ising model. (Left), we compute the density of spins-up $n_\uparrow \equiv \sum_{i=1}^{N} \langle (1 + \sigma_z^{[i]}) \rangle / 2N$ (N is the system's size). The solid lines are based on the results obtained from a variational technique based on a correlated and a product ansatz [205]. On the right panel, we compute the purity of n-site reduced density matrix given by $\Gamma_n \equiv \mathrm{tr}(\rho_n)$ for $D = 6$ for several values of n.

observed in our simulations in the left panel of Fig. 6.7, where simulations for $D = 5, 6$ agree with the correlated variational ansatz in the location of the transition point at $h_x/\gamma \sim 6$. In fact, as the bond dimension D increases, we observe that there is more tendency towards agreeing with the correlated variational ansatz. We also observe a non-monotonic convergence in D, which may be due to a stronger effect of the approximations in the transition region, and which remains to be fully understood. Other quantities can also assess this transition, e.g., the purity of the n-site reduced density matrix $\Gamma_n \equiv \mathrm{tr}(\rho_n)$, which we plot in the right panel of Fig. 6.7 for $D = 6$. We can also see from this plot that the steady states ρ_s for low h_x/γ are quite close to a pure state (for which $\Gamma_n = 1 \forall n$). Results with other bond dimensions do not give a significant difference. From these plots, we do not see any region with bistable behavior for large bond dimensions. It is worth mentioning that for bond dimension $D = 1$ (which is equivalent to the mean field approximation) and $D = 2$, we do find the bistable region (shown in Fig. 6.8). However, we also find that the size of the bistable region shrinks as we increase the bond dimension of our TN and it disappears for $D \geq 3$. Similar behavior has been observed for the case of 1D dissipative XY model [228].

Now coming back to the phase diagram in Fig. 6.7, we can validate our simulations

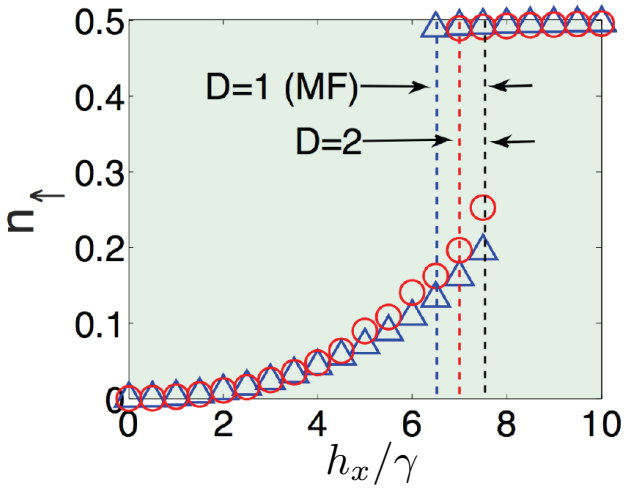

Figure 6.8: Bistable region for $D = 1$ (mean field) and $D = 2$. The region disappears for larger bond dimensions.

by computing the parameters Δ and ϵ_n introduced previously, which we show in the left and right panel of Fig. 6.9 respectively. From this plot, one can see that Δ is always quite close to zero in our simulations, being at most $|\Delta| \sim 0.03$, so that the approximated ρ_s is close to the exact steady state. Moreover, one can also see that ϵ_n is always rather small, e.g., for $D = 6$ it is at most $\epsilon_n \sim -0.017$ for the 4-site density matrix close to the transition region (similar conclusions hold for other bond dimensions). This implies that the negative contribution to the numerical reduced density matrix is quite small, and therefore, does not lead to large errors. In practice, we see that ϵ_n seems to be extensive in n away from the transition region, more specifically, $\epsilon_n \sim n\epsilon_0 + O(1/n)$, with ϵ_0 very close to zero.

Next, we introduce non-zero values of the parallel field h_z. In some regions of the phase diagram, mean field and correlated state variational methods predict the existence of an "antiferromagnetic" (AF) phase, where $n_\uparrow$ attains different values between nearest-neighbors in the square lattice [205]. In our simulations we have also found this antiferromagnetic region up to $D = 5$, see Fig. 6.10 for $V = 5\gamma, \gamma = 0.1$, where for comparison we also show the data from Ref. [205] for the variational ansatz with product states. Quite surprisingly, however, we find no AF phase for $D = 6, 7, 8$ and 9 around this region. The AF phase thus disappears for larger bond dimensions and for these values of the parameters.

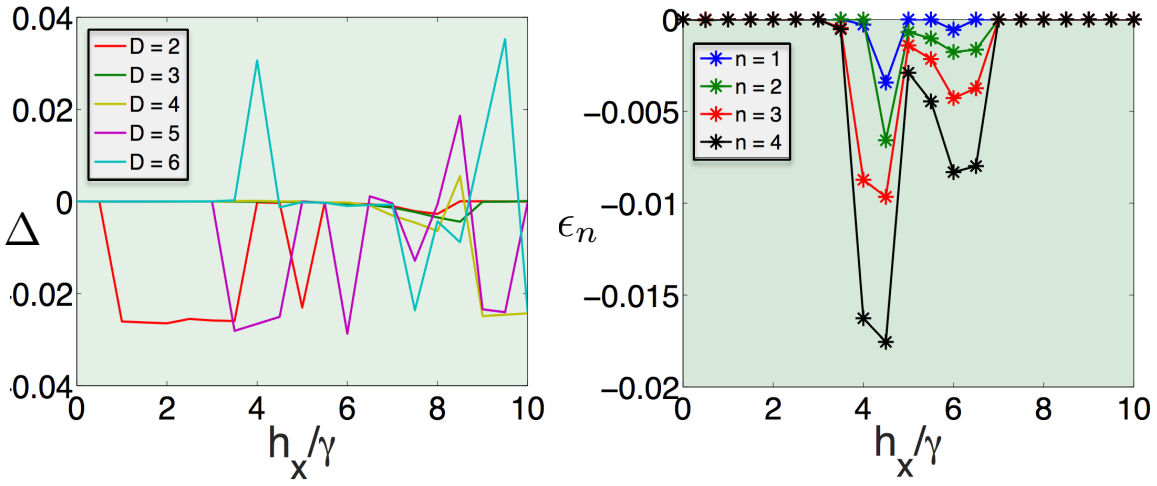

Figure 6.9: (Left) we compute the parameter $\Delta \equiv {}_\sharp\langle\rho_s|\mathcal{L}_\sharp|\rho_s\rangle_\sharp$ up to $D = 6$. The value should be zero in the exact case but we see that in our simulations, the approximations are quiet good. (Right) we also compute the sum of negative eigenvalues of different n-site density matrices given by $\epsilon_n \equiv \sum_{i|\nu_i<0} \nu_i(\rho_n)$. We see that the sum of the negative eigenvalues are also not too large here.

6.2.2 The XYZ model

To show that the success of our algorithm is not just limited to the dissipative spin-1/2 Ising model, we also simulated the dissipative spin-1/2 XYZ model on an infinite 2D square lattice. The Hamiltonian of this model can be written as follows

$$H = \sum_{\langle i,j\rangle} \left(J_x \sigma_x^i \sigma_x^j + J_y \sigma_y^i \sigma_y^j + J_z \sigma_z^i \sigma_z^j\right) \tag{6.19}$$

where the sum is over nearest-neighbor terms, $\sigma_{x,y,z}$ are the different Pauli operators along different directions at a particular site and $J_{x,y,z}$ are the coefficients of their interactions respectively. The Lindbladian of this dissipative model is given by the same jump operators as described in the previous spin-1/2 Ising model i.e. $L_\mu = \sqrt{\gamma}\sigma_-^\mu$. The steady state phase diagram of this model is highly non-trivial compared to the XXZ model. It can be shown that the XXZ model does not experience a phase transition in its steady state phase diagram. However, new types of magnetic orders may emerge for the XYZ case due to competition between *precessional* and dissipative dynamics. Such a model can also be implemented in systems of ultracold atoms with anisotropic superexchange or dipolar interactions. This model has been analyzed recently by Mean Field (MF) [216], Cluster Mean Field (CMF) [217] and Corner Space Renormalization methods [229]. In particular, in Ref. [217], a possible

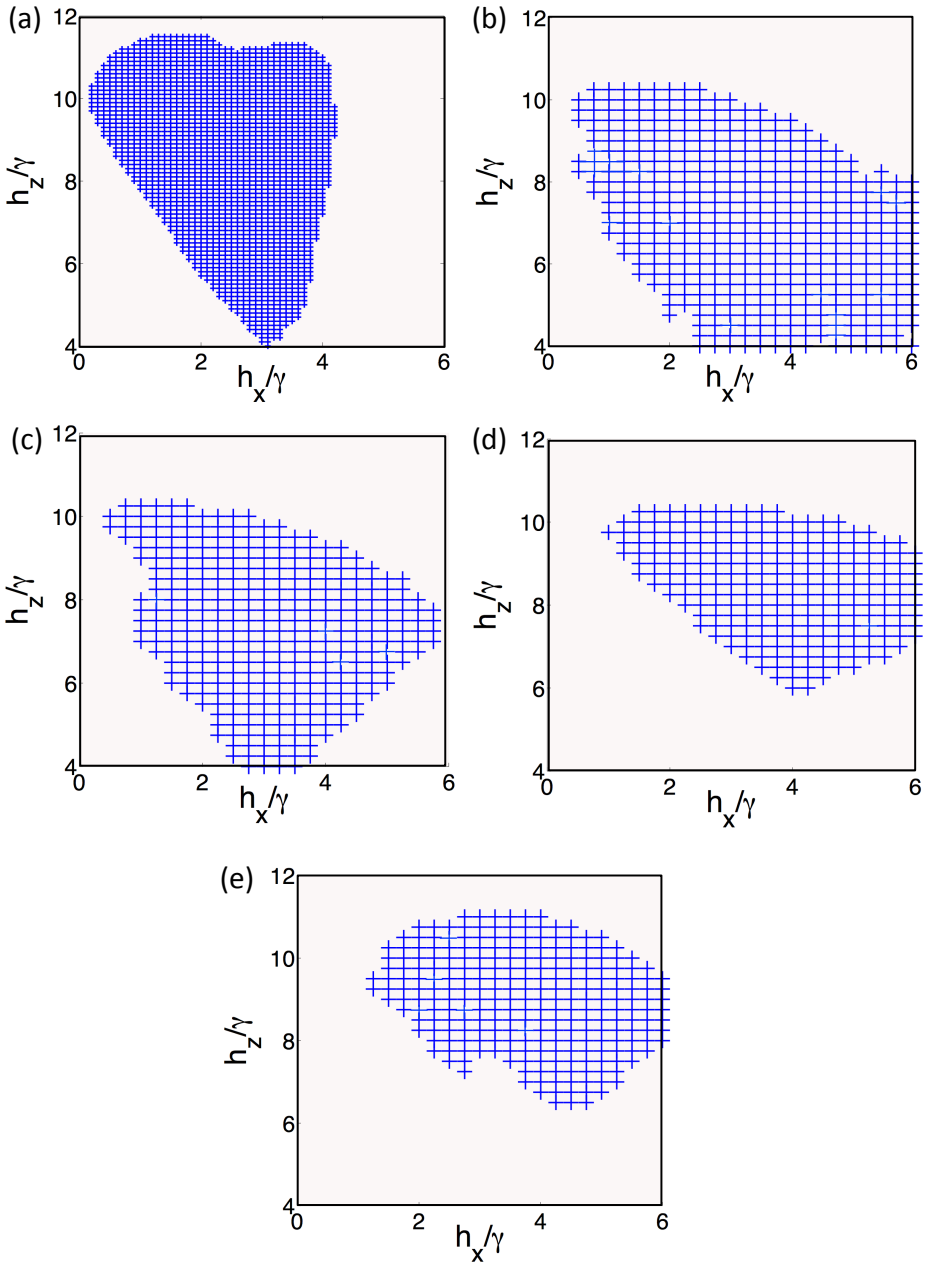

Figure 6.10: AF region found using (a) variational ansatz based on [205] (b) $D = 2$ (c) $D = 3$ (d) $D = 4$ and (e) $D = 5$ iPEPS technique. The AF region disappears for higher bond dimensions (6, 7, 8 and 9) in our simulations.

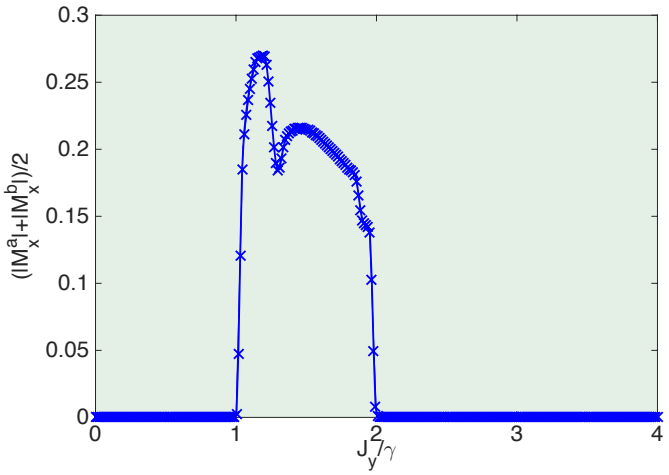

Figure 6.11: Ferromagnetic order parameter for the dissipative XYZ model, for $J_x = 0.5$, $J_z = 1$ and $D = 4$, as an average of $|M_x| = |\langle\sigma_x\rangle|$ over the two sites a and b in our 2D PEPO construction of ρ. As we can see, there is no re-entrance of the ferromagnetic order at large values of J_y/γ.

re-entrance of the ferromagnetic phase at large coupling was discussed. The authors claimed that the phenomenon of re-entrance could be an artifact of the CMF approach used and would disappear for large cluster sizes.

We investigated this model using our dissipative iPEPS algorithm and we did not find the re-entrance phenomenon that was seen in previous studies. This is shown in Fig. 6.11 for $J_x = 0.5$, $J_z = 1$ and $D = 4$. The ferromagnetic order parameter is plotted then as a function of J_y/γ. Thus, we did not observe the phenomenon of re-entrance for large values of J_y/γ for these parameters. The plots for higher bond dimensions do not differ significantly. We also computed the parameters ϵ_n and Δ as described in the previous section for these points. They are shown in Fig. 6.12. In these plots, one can see larger errors around the regions of phase transitions. Higher bond dimensions did not change the conclusion. Thus, we can conclude that our algorithm provides a good approximation of the steady states for the dissipative XYZ model as well. An investigation into the full phase diagram of the model remains pending and is something we would like to do in the future.

6.3 Conclusions and outlook

In this chapter, we have discussed dissipative open quantum systems. Such a system obeys the Lindbladian master equation if we assume the evolution to be Markovian.

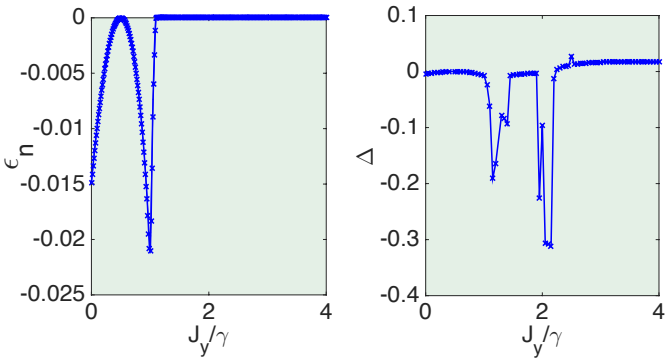

Figure 6.12: (Left) ϵ_n which is the sum of the negative eigenvalues of a four-site reduced density matrix is shown for the points in the phase diagram for $D = 4$. (Right) Δ which is the expectation value of $\mathcal{L}$ is also shown for the same parameter and bond dimensions. Larger bond dimensions did not change the conclusion.

One can find the steady state of this system using this equation. However, solving this master equation for a many-body system is extremely hard as the number of parameters required to describe such a system scales exponentially with its size. The physical constraints of the reduced density matrix such as positivity, hermiticity and trace one are also a problem in their numerical investigation. Recently, there have been some advances using TN approaches to solve these systems for 1D systems. The numerical techniques for 2D systems are much more rare. This was the main motivation of our work. The important highlights of our work in this chapter can be listed as follows

- We have proposed a TN algorithm to study the steady states of 2D open dissipative quantum systems in the thermodynamic limit. At the heart of our technique lies the concept of 'Choi' isomorphism where we rewrite the coefficients of a matrix as those of a vector. Based on the strong parallelism between finding the ground state of a Hamiltonian and the steady state of a Liouvillian, we make use of the existing iPEPS techniques for finding the ground state. The implementation of our technique is extremely simple and efficient.

- We benchmark our algorithm by investigating a dissipative spin-1/2 quantum Ising model which is relevant for the on-going experiments with ultracold Rydberg atoms. The phase diagram of this model is also still not very clear. Our results were compared with another technique based on a variational technique using a correlated and a product ansatz.

- Our results support the existence of a first order transition in this model, while we find no evidence for a bistable region for large bond dimensions. We also do not find the existence of antiferromagnetic region in the phase diagram studied previously for large bond dimensions.

- We also investigated the dissipative spin-1/2 XYZ model using our technique. Our results do not support the reappearance of ferromagnetic phase as claimed previously. An investigation into the full phase diagram of the model remains to be done in the future.

Our method is the first TN implementation to compute steady states in 2D quantum lattices. This method for studying open 2D dissipative systems has opened up a lot of new interesting windows which we would like to study in the future such as engineering of topologically ordered states by dissipation in 2D quantum lattice systems. It could also be applied to finite temperature states, provided that a microscopic model for the coupling to the heath bath is included. Finally, it would be interesting to understand these results in the context of area laws for rapidly mixing dissipative quantum systems [230].

Chapter 7

General conclusions and outlook

7.1 Thesis overview

This thesis was comprised of four important sections. The first section contained the first three chapters where we discussed the concept of entanglement and introduced Tensor Network techniques. To be more specific, the first chapter provided the context of our work and the thesis in a very general setting. We discussed the importance of investigating new, exotic phases of matter and phenomena in the context of our ever increasing demand for energy and resources. We also reasoned why it is so difficult to study such quantum many-body systems. In Chapter 2, we discussed briefly the history of quantum entanglement and its formal definition and how we can quantify it. We also described some important topics such as the Schmidt decomposition, the variational principle and quantum phase transitions in the context of entanglement. It was realized that entanglement could be key to understanding the properties of quantum many-body physics. In Chapter 3, we introduced Tensor Network States to study such systems. We explained their importance and advantages compared with the existing numerical techniques. We also described some important examples of TN states such as Matrix Product States and Projected Entangled Pair States which were used in the rest of the chapters.

The remaining sections contained important results on Symmetry Protected Topological (trivial) phases, frustrated quantum systems and open dissipative quantum systems. In Chapter 4, we discussed Symmetry Protected Topological and trivial phases in a spin-2 quantum chain with a Heisenberg-like nearest-neighbor Hamiltonian. We simulated the ground state of this model using MPS and iTEBD and studied its phase diagram based on several properties such as the entanglement spectrum, entanglement entropy, string order parameters, projective representation of the symmetries protecting the phases, etc. We found several spin-1 SPT phases and

studied the phase transition between them using Conformal Field Theories. We also found a candidate that could be a gapless SPT phase. Moreover, we learned that unlike SPT, SPt phases are adiabatically connected to product states by some path that preserves the protecting symmetry. In the process, we found three such phases separated by quantum phase transitions and also described them using CFT.

In the next section in Chapter 5, we discussed frustrated quantum systems and how the iPEPS can be used to study such systems in a kagome lattice. We made some comparisons of the ground state energy of the kagome Heisenberg antiferromagnet with other existing numerical techniques. We also found that our ground state for this model using our technique gives us a Valence Bond Crystal. We then studied the XXZ model in a kagome lattice in the presence of an external field. We found several magnetization plateaus of which we took a particular interest in the 1/3 plateau. Based on our numerics, we found that such a state is not a chiral spin liquid. We also found that in all regimes of our phase diagram, the 1/3 plateau is degenerate between the Nematic state and Valence Bond Crystal Solid. Our studies were based on two independent iPEPS approach: a 6 and 12-site usual iPEPS coarse graining three sites in the kagome lattice to one site in the square lattice and a 9-site iPESS approach. We found that the 6-site approach gives us lower energy because it has more variational parameters. On the other hand, the 9-site approach gives us additional plateaus such as 1/9, 5/9 and 7/9 because the magnetic structure of these plateaus is commensurate with the number of unit cells.

Chapter 6 of this thesis dealt with open quantum systems in 2D. We proposed a simple TN algorithm that can be used to simulate the steady state of 2D dissipative quantum system in the thermodynamic limit. We demonstrated our algorithm by investigating a spin-1/2 dissipative quantum Ising model that has experimental relevance with ultracold Rydberg atoms. We found a first order phase transition in the phase diagram of this model and found no bistability issues. We also did not find antiferromagnetic regions for higher bond dimensions in the phase diagram as suggested by previous studies. We also investigated the dissipative spin-1/2 XYZ model briefly and found no re-entrance of the ferromagnetic region as claimed previously.

7.2 Perspectives and outlook

To sum things up, this thesis has demonstrated that Tensor Network algorithms are extremely useful for studying exotic quantum many-body systems based on their

entanglement properties: be it one dimensional gapped phases of matter or two dimensional quantum systems. It can even be used to describe mixed states. Our studies have opened up a lot of interesting and exciting questions which we are willing to investigate in the future. For example, in Chapter 4, we found a certain T_y phase which is SPT and seems to exhibit gapless degrees of freedom. Recently, there has been some investigation on such gapless SPT phases [147]. It would be certainly interesting to find the exact nature of this phase. The full phase diagram of our spin-2 Hamiltonian also remains to be explored. In our study of frustrated quantum systems, we found that our numerical simulations do not support the existence of a chiral spin liquid at the 1/3 plateau of the XY point of the XXZ model. However, it is not definitely clear if this is so because the state itself is not chiral or if PEPS cannot capture such a chiral state. In Ref. [201], it was shown that, in principle, PEPS can be used to describe chiral topological order but a numerical realization starting from a chiral Hamiltonian has not been achieved so far. It remains to be seen if this can be done if we push our computational limit.

The study on our dissipative open quantum system has also opened up a lot of new windows for the future. Effects of dissipation could be used to engineer exotic phases of matter displaying Topological order, etc. For example, in Ref. [18], dissipation was used to engineer topological phases in atomic quantum wires of spinless atomic fermions in an optical lattice coupled to a bath. And in Ref. [231], a scheme was proposed to generate Pfaffian states using cold bosonic atoms using strong three-body dissipation. Thus, in principle, well-engineered dissipation can be useful. Furthermore, it would be interesting to study the effects of dissipation on 2D topological phases such as the Toric code or find ways to stabilize them at finite temperature. This will have potential applications in quantum computing. The other interesting aspect of this problem includes dissipative quantum phase transitions, non-Markovian dynamics of open quantum system using TN, area laws for mixed states in the context of rapidly mixing systems, etc.

Efforts towards advancing the existing TN algorithms, for example, to make them more efficient, user-friendly and providing access to larger users are also worth making. Recently, we started running our algorithms in GPUs instead of CPUs and found much improvement in the efficiency especially for simulations involving higher bond dimensions. There are other ways to improve the existing techniques such as using more efficient matrix decomposition methods, implementing symmetries in the tensors, etc. Of course, we expect a lot of numerical studies of quantum many-body

systems using TN algorithms with increased computational effort and new implementation techniques in the years to come. This will eventually overcome some of the existing limitations of TN algorithms such as the high computational cost of running an iPEPS full update simulation with large bond dimensions. The rapid development of TN algorithms should not, however, be seen in the context of competition with the existing numerical techniques. There is no ultimate technique available to study nature. In fact, their strength lies only when they are used in complement with one another. Since nature obeys the laws of quantum mechanics, and so far we are mostly performing simulations using classical computers, the basic philosophical question of *how close can we simulate nature?* is something that may be answered eventually with the help of quantum computers. This is a quest I would like to keep pursuing and provides enough motivation to continue working beyond this PhD thesis!

Appendix A

Field Theory description of the spin-2 QPT

Having discussed the concept of entanglement entropy (von Neumann entropy) as a measure of bipartite entanglement in Chapter 2, we will now see how this can be used for understanding critical systems, for example, in a spin chain. For such a critical system, the entanglement entropy is known to diverge and as such, the entropy grows proportional to $\log l$ for large lengths of the subsystem l in an infinitely long chain. At the critical point where the correlation length diverges, the field theory is massless, and is a Conformal Field Theory (CFT). At this point, the von Neumann entropy of a subsystem of length l was calculated by Holzhey *et al.* [232]. In that paper and in Ref. [233] and [234], it was shown that the entropy of a subsystem A of length l is given by

$$S_A \sim (c/3)\log(l/a), \tag{A.1}$$

where c is the central charge[1] of the CFT and a is the lattice spacing of the spin chain. We will not go into the details of the derivation here. Further generalizations of the above formula can be made based on the boundary conditions and finite length L of the system. For our purpose, Eq. A.1 is the relevant formula to be used. For the model in Eq. 4.1 of Chapter 4, the phase transitions between $SO(5)$ Haldane/IH and IH/large-D were studied in Ref. [139] where it was shown that the system can be described at low energies using an effective field theory of five Majorana fermions $\xi^a (a = 1, \ldots, 5)$:

$$\mathcal{H}_{\text{eff}} = -iv\sum_{a=1}^{5}(\xi_R^a \partial_x \xi_R^a - \xi_L^a \partial_x \xi_L^a) - im_1\sum_{a=1}^{2}\xi_R^a \xi_L^a - im_2\sum_{a=3}^{4}\xi_R^a \xi_L^a - im_3 \xi_R^5 \xi_L^5 \tag{A.2}$$

[1]The central charge is the Casimir operator that commutes with all other symmetry operators of the theory.

where v and m_a are velocity and masses of the Majoranas. For the IH (or T_0) phase, three fermions have negative masses m_2 and m_3, and two have positive mass m_1, producing three Majorana edge modes forming spin-1/2 edge states. The phase transitions happen whenever $m_1 = 0$ (SO(5)/IH), or $m_2 = 0$ (IH/large-D). In both cases, two Majorana fermions become massless, and hence these transitions correspond to a CFT with central charge $c = 2 \times 1/2 = 1$. For the transitions between the different effective spin-1 SPT phases, we see from the numerics that T_x, T_y and T_z also have spin-1/2 edge modes because of the two-fold degeneracy in the entanglement spectrum. If we try to describe them using the Majorana field theory, then three Majorana masses must be negative and two positive. If this is the case, then the only possibility is that the three Majoranas with negative mass are *different* from those in the T_0 phase (otherwise the phases could be deformed into each other without closing the gap). Thus, if the field theory is correct in this regime, then phase transitions amongst the T_0, T_x, T_y and T_z phases can be viewed as processes of *sign exchange amongst Majorana masses*. To change their sign, some of these masses must be zero at some point, which implies a quantum phase transition described by a CFT. To check the plausible validity of this picture we compute the central charge of the $T_y - T_0$ transition in Fig. 4.9(b) for $D = 1.5$ using the scaling of the entanglement entropy of a block of length L. Our result in Fig. 4.11 agrees with $c = 3 \times 0.6528 \approx 2$ which means that 4 out of the 5 Majoranas would become massless at criticality and interchange the signs of their masses. A similar behavior is found for the other transitions between the effective spin-1 SPT phases in Fig. 4.9.

For the model in Eq. 4.32, we have two critical points at D_{c1} and D_{c2} as shown in Fig. 4.12. Doing a similar scaling of the entanglement entropy as a function of $\log L$ where L is the length of our MPS, we obtain a central charge of $c = 1$ at both the points. We provide the field theory description of this as follows. The model in Eq. 4.32 admits a simple field theory description in terms of two bosonic sine-Gordon fields and one massive Majorana fermion field. This description is a generalization of the one in Ref. [135], and equivalent under refermionization, for Luttinger parameters $K_1 = K_2 = 1$, to the five Majorana field theory introduced above for the case of the SPT phases. The Hamiltonian density reads

$$\mathcal{H}_{\text{eff}} = \mathcal{H}_{b_1} + \mathcal{H}_{b_2} + \mathcal{H}_f, \tag{A.3}$$

with

$$\mathcal{H}_{b_i} = \frac{v_i}{2\pi}\left(K_i(\partial_x\theta_i)^2 + \frac{1}{K_i}(\partial_x\phi_i)^2\right) + g_i\cos(2\phi_i), \tag{A.4}$$

the two bosonic sectors for $i = 1, 2$, and

$$\mathcal{H}_f = -iv\left(\xi_R \partial_x \xi_R - \xi_L \partial_x \xi_L\right) - im\xi_R \xi_L \tag{A.5}$$

the Majorana fermionic sector. In these equations, θ_i and ϕ_i are dual fields satisfying $[\phi_i(x), \theta_i(x')] = i(\pi/2)(\mathrm{sgn}(x - x') + 1)$, and $\xi_{R/L}(x)$ is a right/left moving Majorana fermion field. The strategy to derive Eq. A.3 is essentially the same as in Refs. [139, 135], so we refer the reader to those references for further details. The description of the quantum phase transitions is thus quite easy thanks to the field theory above. In particular, the Majorana field remains always gapped and therefore plays no role in the description of the quantum phase transitions. However, we include it so that the connection to the five Majorana field theory in Ref. [141] is more transparent. We thus expect critical behaviors corresponding to the two massless bosons with $K_1, K_2 < 2$, and (i) $g_1 = 0$, and (ii) $g_2 = 0$. Both regions correspond, independently, to two different quantum critical lines with the central charge $c = 1$ of a free massless boson. As we have seen, this is what we got in our numerical results.

Appendix B

TN algorithms in 1D

B.1 Finding ground states: iTEBD algorithm

There are several techniques available to find the ground state of a 1D Hamiltonian based on Matrix Product States such as Density Matrix Renormalization Group (DMRG) [45, 46], Time Evolving Block Decimation (TEBD) [77, 78], etc. In this appendix, we will describe in detail how the TEBD can be used to find the ground states of 1D Hamiltonians for the case of infinite systems, also known as iTEBD. This is the algorithm we used for our simulations in Chapter 4 of the thesis. This technique can also be used for the case of finite, open and even periodic boundary condition after some modifications. Let us now consider a 1D Hamiltonian of the following form

$$H = \sum_j h_{j,j+1}, \tag{B.1}$$

i.e. we assume that our Hamiltonian is translationally invariant and can be decomposed as a sum of nearest-neighbor terms. One can also consider other kinds of interactions depending on the problem.

Let us now start from some initial state $|\psi_0\rangle$ written in the form of an infinite Matrix Product States (iMPS) with some bond dimension χ. To do this, we assume some translational invariance and define some unit cells. In our case, we assume a translational invariance with a 2-site unit cell. If we want to evolve our state with some Hamiltonian H for some time t, we need to compute

$$|\psi(t)\rangle = e^{-iHt}|\psi_0\rangle. \tag{B.2}$$

We now divide our Hamiltonian into odd and even parts i.e $H = H_{\text{odd}} + H_{\text{even}}$ where $H_{\text{odd}} = \sum_{j \text{ odd}} h_{j,j+1}$ and $H_{\text{even}} = \sum_{j \text{ even}} h_{j,j+1}$. We assume that the operators $h_{j,j+1}$ do not commute with each other for the odd and the even j. We can therefore make

use of the Suzuki Trotter approximation to decompose our evolution operator e^{-iHt} as

$$e^{-i\delta t(H_{\text{odd}}+H_{\text{even}})} = e^{-iH_{\text{odd}}\delta t}e^{-iH_{\text{even}}\delta t} + \mathcal{O}(\delta t^2) \tag{B.3}$$

where δt is a small time step and $\mathcal{O}(\delta t^2)$ is the error associated with the approximation. Since all the terms in H_{odd} commute (and also H_{even}), we can now write it as

$$e^{-iH_{\text{odd}}\delta t}e^{-iH_{\text{even}}\delta t} = \prod_{j \text{ odd}} e^{-ih_{j,j+1}\delta t} \prod_{j \text{ even}} e^{-ih_{j,j+1}\delta t}. \tag{B.4}$$

Thus, in order to find our state in time t, we need to apply the above operator to our state $t/\delta t$ times. In the above decomposition of our Hamiltonian, we have used the first order Suzuki-Trotter approximation. One can also use the second order approximation which is very easy to implement. It is worth noting that during the evolution of the state, the bond dimension of our iMPS grows with the number of steps and therefore it is necessary to truncate it with some effective bond dimension χ'. This can be done while performing the Singular Value Decomposition (discussed also in Chapter 2) by keeping only the χ most relevant singular values. The above algorithm is used for performing a real time evolution of our state. In order to obtain the ground state, we use the imaginary time evolution which corresponds to simply substituting the it in the evolution operator e^{-itH} with τ i.e. $e^{-\tau H}$. In the limit $\tau \to \infty$, such an evolution will give us the ground state of our Hamiltonian H.

$$|\psi_G\rangle = \lim_{\tau\to\infty} \frac{e^{-\tau H}|\psi_0\rangle}{||e^{-\tau H}|\psi_0\rangle||} \tag{B.5}$$

where $|\psi_G\rangle$ is the ground state of the Hamiltonian and $|\psi_0\rangle$ is some initial state which is not orthogonal to the ground state. The whole algorithm for finding the ground state can be summarized as follows:

(a) Start from some initial iMPS with a unit cell with a fixed number of sites say 2. This can be done by starting from some initial tensors Γ_A, Γ_B, λ_A, and λ_B. The TN constructed from these tensors is shown in Fig. B.1(a).

(b) Apply the evolution operator defined as $g = e^{-\delta\tau h_{j,j+1}}$ to the even links. This can be done by simply applying this operator on the link between Γ_A and Γ_B. This process will give us the tensor C. This is shown in Fig. B.1(b).

(c) Perform a Singular Value Decomposition on C and retain only the χ largest singular value. This process of truncation is important or the bond dimension of our iMPS will grow. χ is the truncation parameter here. Now, reshape it to obtain new tensors defined as Γ'_A, Γ'_B and λ'_A as shown in Fig. B.1(c).

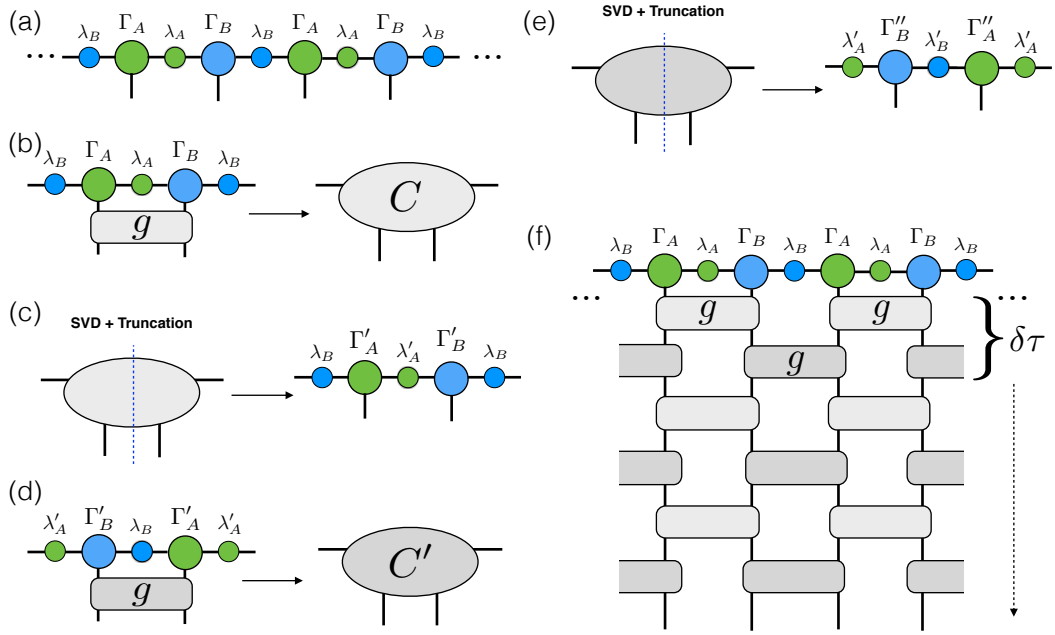

Figure B.1: (a) Initial iMPS defined by tensors Γ_A, Γ_B, λ_A and λ_B; (b) The evolution operator $g = e^{-\delta\tau h_{j,j+1}}$ acts on the even links of the iMPS and gives tensor C; (c) SVD is performed on C and new tensors Γ'_A, Γ'_B and λ'_A are obtained with truncated bond dimension χ after reshaping them; (d) the same evolution operator is now applied to the odd links to obtain C'; (e) SVD is performed on C' and new tensors Γ''_A, Γ''_B and λ'_B are obtained with bond dimension χ; (f) steps (a)-(e) are repeated until convergence to obtain the ground state of the Hamiltonian.

(d) Repeat step (b), but this time by applying the evolution operator to the odd links of the iMPS. This can be done by applying it to the link between Γ'_B and Γ'_A. This will give us tensor C'. See Fig. B.1(d).

(e) Repeat step (c), but this time on the tensor C'. This will give us new tensors Γ''_A, Γ''_B and λ'_B. Along with λ'_A from step (c), we have a new updated iMPS. This completes one Trotter step. See Fig. B.1(e).

(f) Repeat steps (a)-(e) until convergence. This will give us the ground state of our Hamiltonian.

The different steps of the algorithm have been illustrated in Fig. B.1. Thus, we have the ground state of our Hamiltonian in the form of iMPS with bond dimension χ. The tensors in the ground state are said to be in the so-called canonical form which we have discussed in detail in Chapter 4 of the thesis. The SVD steps in the algorithm

automatically ensures the canonical form of the iMPS. Now, we can use the ground state iMPS to compute ground state observables. We discuss this in the next section.

B.2 Computing observables

To extract information from the ground state, one can compute the expectation value of local operators. This can be done exactly without any need for approximation for an MPS. For infinite MPS with open boundary conditions such as the ones we have been discussing, we show how this can be done. For an MPS with N sites, the calculation of the exact expectation values can be done in $O(Np\chi^3)$ time where χ is the bond dimension of the MPS. For an iMPS, the calculation can be done exactly in time $O(p\chi^3)$. We use the so-called transfer matrix technique for this.

Let us consider the problem of computing the expectation value of a local operator O of our ground state iMPS. We assume that our ground state is already in the canonical form here. The important steps of the algorithm are given below.

(a) Define the transfer matrix T using the tensors Γ_A, Γ_B, λ_A and λ_B from the ground state iMPS as shown in Fig. B.2(a).

(b) Perform an eigenvalue decomposition of the matrix T and extract the largest eigenvalue ω_1 and the corresponding left and right eigenvectors $\langle L_1|$ and $|R_1\rangle$. This is shown in Fig. B.2(b).

(c) The expectation value of the local operator O can be computed by contracting the tensors as shown in the right hand side of the equality of Fig. B.2(c). The logic of the last equality comes from the fact that if we multiply the transfer matrix T with itself N times, then for $N \to \infty$, only the largest eigenvalue and its corresponding eigenvector survives.

Thus, one can compute the observables from our iMPS tensors exactly using the transfer matrix technique as illustrated in Fig. B.2. One can use a similar process for computing two-point correlations, energy, etc. For finite MPS, one can contract the TN exactly without using the transfer matrix technique.

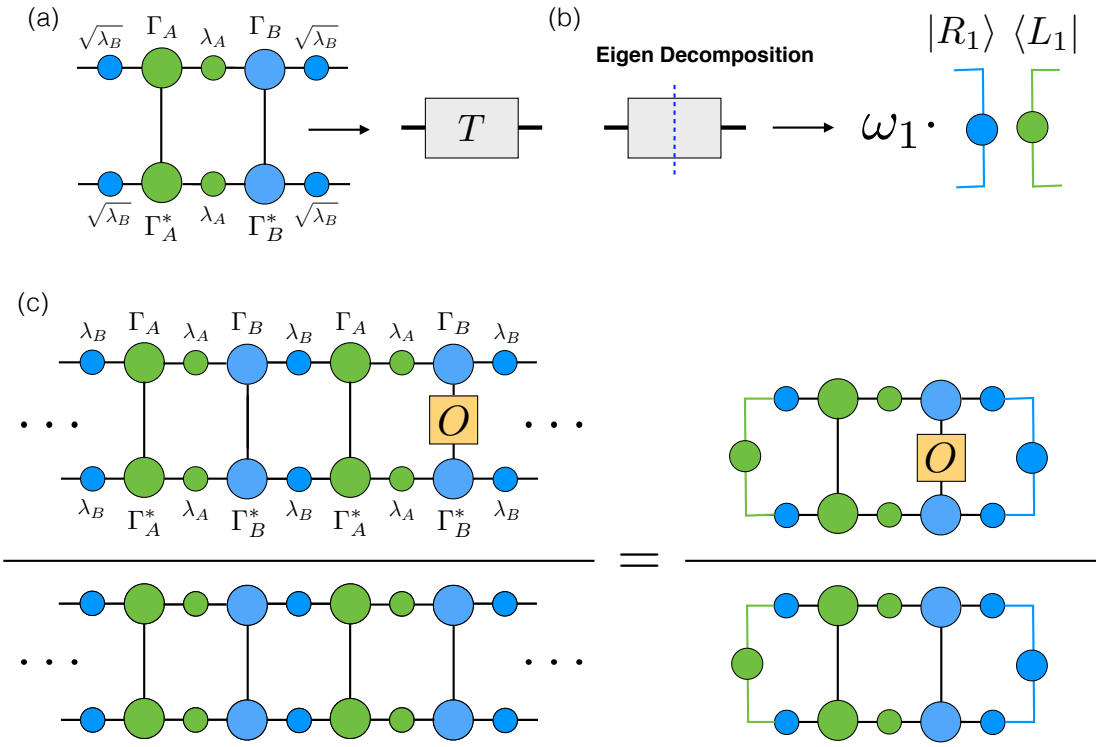

Figure B.2: (a) The transfer matrix T is defined using the tensors in the iMPS ground state. (b) We perform eigenvalue decomposition of T and extract the largest eigenvalue ω_1 and the corresponding left and right eigenvectors $\langle L_1|$ and $|R_1\rangle$. (c) The expectation value of the local operator O can be obtained by contracting the tensors as shown in the right hand side of the equality using $\langle L_1|$ and $|R_1\rangle$.

Appendix C

TN algorithms in 2D

In this section, we discuss some of the optimization schemes for computing the ground states of 2D Hamiltonians using infinite Projected Entangled Pair States (iPEPS). We limit ourselves only to the case of nearest-neighbor interacting Hamiltonians in this thesis, but the algorithm can be extended to include higher order interaction terms in general. We also show how to compute local observables once we have the ground state wave function. There are several update schemes available in the iPEPS formalism for computing the ground state of the 2D Hamiltonian such as the simple [181, 182], full [183], fast full [184] and the variational update [47]. In this thesis, we have made use of the first three update schemes. We also consider a system of infinite size so that we can assume translational invariance by taking a unit cell with a fixed number of sites. We discuss the different update schemes in the following sections.

C.1 Simple update

As the name suggests, the simple update scheme is by far the simplest and the most efficient update scheme for iPEPS. It updates the tensors only locally without taking into account the effect of the environment. Now, let us see how we can find the ground states of infinite, translationally invariant 2D systems using this scheme. Consider a 2D Hamiltonian that can be written as the sum of nearest-neighbor terms as follows:

$$H = \sum_{\langle i,j \rangle} h^{[i,j]}. \tag{C.1}$$

In order to compute the ground state of H, we will once again perform the imaginary time evolution as in Eq. B.5. We will discuss the case of a square lattice with two sites unit cell. This means that we will have two unique tensors Γ_A and Γ_B repeated all over the square lattice for an infinite system as shown in Fig. C.1. The λ's are the

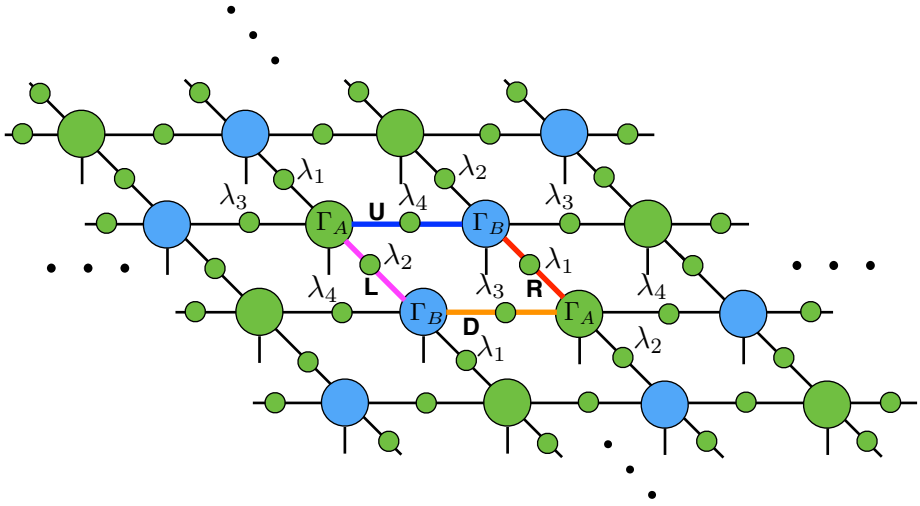

Figure C.1: iPEPS with a two-site unit cell. Four different links (up, right, down and left) are depicted with four different colors in the diagram.

matrices on every link. We can see that corresponding to the two-site unit cell, there are four different links in the network. We start our update process by dividing our Hamiltonian into four different parts corresponding to the four links as follows

$$H = H_{\mathrm{U}} + H_{\mathrm{R}} + H_{\mathrm{D}} + H_{\mathrm{L}} \tag{C.2}$$

In this case, one complete Trotter time step will consist of updating the four different links of the 2D tensor network with the corresponding part of the Hamiltonian (i.e. we apply H_{U} to link U and so on) as follows

$$e^{-\delta\tau H} \approx e^{-\delta\tau H_{\mathrm{U}}} e^{-\delta\tau H_{\mathrm{R}}} e^{-\delta\tau H_{\mathrm{D}}} e^{-\delta\tau H_{\mathrm{L}}} + O(\delta\tau^2) \tag{C.3}$$

Repeating this step a large number of times ($N \to \infty$) gives us the ground state of our Hamiltonian as in Eq. B.5. Details on how to apply the update for a single link is similar to what we described for the case of 1D chain in Appendix B. The computational complexity or the leading order for the cost of the tensor update depends on the contraction order we choose. A very naive tensor contraction for this update scheme has a complexity of $\mathcal{O}(d^4D^6)$ where d is the physical dimension and D is the bond dimension of the iPEPS for every iteration. It is worth reminding here that although the simple update approach works very well and efficiently in phases with a large gap and a small correlation length, it may not be very accurate for problems close to quantum critical points with large correlation lengths. We therefore need the full update to tackle these problems. We will discuss them briefly in the subsequent sections.

C.2 Computing observables

Once we have computed the ground state tensors of our 2D Hamiltonian, we need to be able to compute observables out of it. However, this is not an easy task given that we have to first compute the infinite-sized environment of the sites where we want to compute the observables. Because there is no such thing as the canonical form of the PEPS as in the case of 1D MPS, exact contraction of the PEPS for the purpose of computing the environment is extremely inefficient. In fact it was shown that this is a ♯P - Hard problem [112]. Luckily, there are several approximation schemes available to compute the environment of our tensors such as the boundary MPS technique [50], Higher Order Transfer Renormalization Group (HOTRG) [85], Corner Transfer Matrix Renormalization Group (CTMRG) [51], etc. In this section, we will discuss the CTMRG technique which is also what we used in all our simulations in this thesis. To keep things simple, we will only discuss the case of a one-site unit cell in the TN i.e we assume that the tensor A is repeated everywhere in the infinite lattice. The actual algorithm used in this thesis has a two-site unit cell structure. Now, let us consider the problem of computing an observable at a particular site for our infinite 2D system. The exact contraction required for this purpose is shown in the left panel of Fig. C.2(a). One can think of this as the 2D network of tensors shown in the right side of Fig. C.2(a). This network consist of the blue tensors a everywhere except at the point where we want to compute the observable. The tensors a can be easily obtained from the tensors A and $A^\dagger$ by simply contracting their physical indices. The orange tensor in the center can be obtained similarly if we include the observable while contracting A and $A^\dagger$. The target now is to find the environment of the tensor in the middle by finding a set of fixed point tensors $\{C1, C2, C3, C4, T1, T2, T3, T4\}$. $C1, C2, C3, C4$ correspond to the four corner transfer matrices while the two half-column and half-row matrices are given by $T1, T2, T3, T4$.

In order to find these fixed-point tensors, we perform iteratively coarse-graining moves in *up, down, right* and *left* directions until the environment converges. This technique is, therefore, also known as the directional corner transfer matrix algorithm [51]. This is illustrated in Fig. C.4 and described below in detail:

(1) Insertion: We insert a new set of tensors comprising of a, the half-column matrices $T1$ and $T3$.

(2) Absorption: We absorb this new column into our initial tensors on the left border i.e. $C1$, $T4$ and $C4$ to obtain the new tensors $nC1$, $nT4$ and $nC4$.

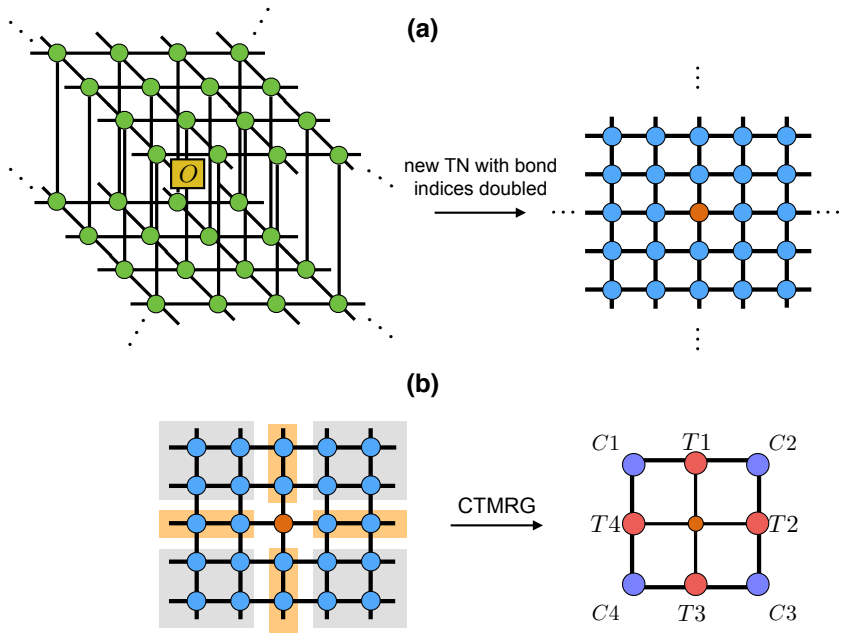

Figure C.2: (a) (left) Computing an observable at a particular site for the iPEPS; (right) the tensors can be contracted with its conjugate counterpart to obtain the new TN with their bond indices doubled. (b) The environment of the new TN is approximated using some fixed point tensors $\{C1, C2, C3, C4, T1, T2, T3, T4\}$.

(3) Renormalization: Because the new tensors $\{nC1, nT4, nC4\}$ has dimensions larger then the original ones $\{C1, T4, C4\}$, we need to renormalize them with isometry $Z (Z^\dagger Z = \mathbb{1})$ so that the dimensions do not grow excessively with the successive iterations.

There are different ways to define the isometry Z. One possibility is to use the eigenvalue decomposition of $nC1nC1^\dagger + nC4nC4^\dagger = nZ\Lambda nZ^\dagger$. This is shown in Fig. C.4. We can then obtain the isometry Z which we want to use from nZ by keeping the entries which correspond to the D largest eigenvalues of Λ. Note that the above process is for a move along one direction. One needs to repeat the process for the other three directional moves *up*, *right* and *down*. This forms one iteration and we repeat the process until the environment converges. The computational complexity, for example, for a naive absorption step would be $\mathcal{O}(\chi^2 D^8)$. The figure shown in C.4 is for a one-site unit cell. For a two-site unit cell (which is actually the one used in this thesis), the steps are similar but one needs to find additional isometries. This is shown in Fig. C.5. Once we have computed the fixed-point tensors, we can easily calculate the expectation value of our observable by contracting the TN shown in the right side of Fig. C.2(b).

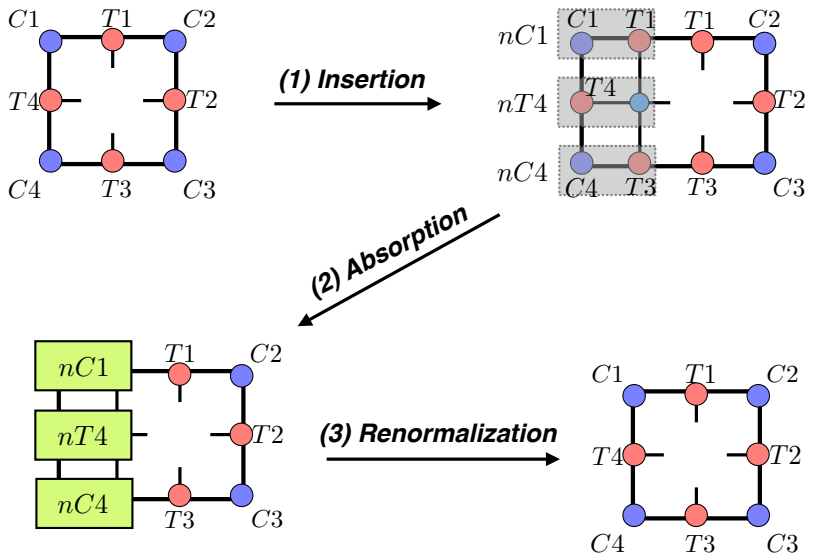

Figure C.3: A directional move of the CTM algorithm. It involves the three steps of *insertion*, *absorption* and *renormalization*. The process has to be done for all the directional moves i.e *up*, *right*, *down* and *left*.

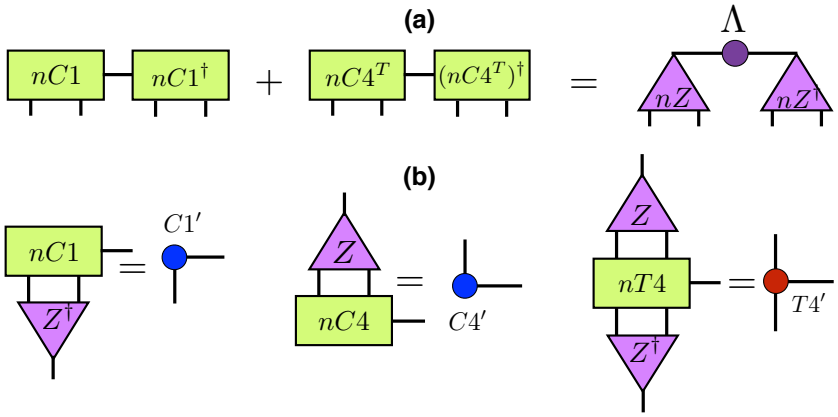

Figure C.4: Finding the isometries for the renormalization for one of the directional moves. They are then used to find the updated tensors of the environment.

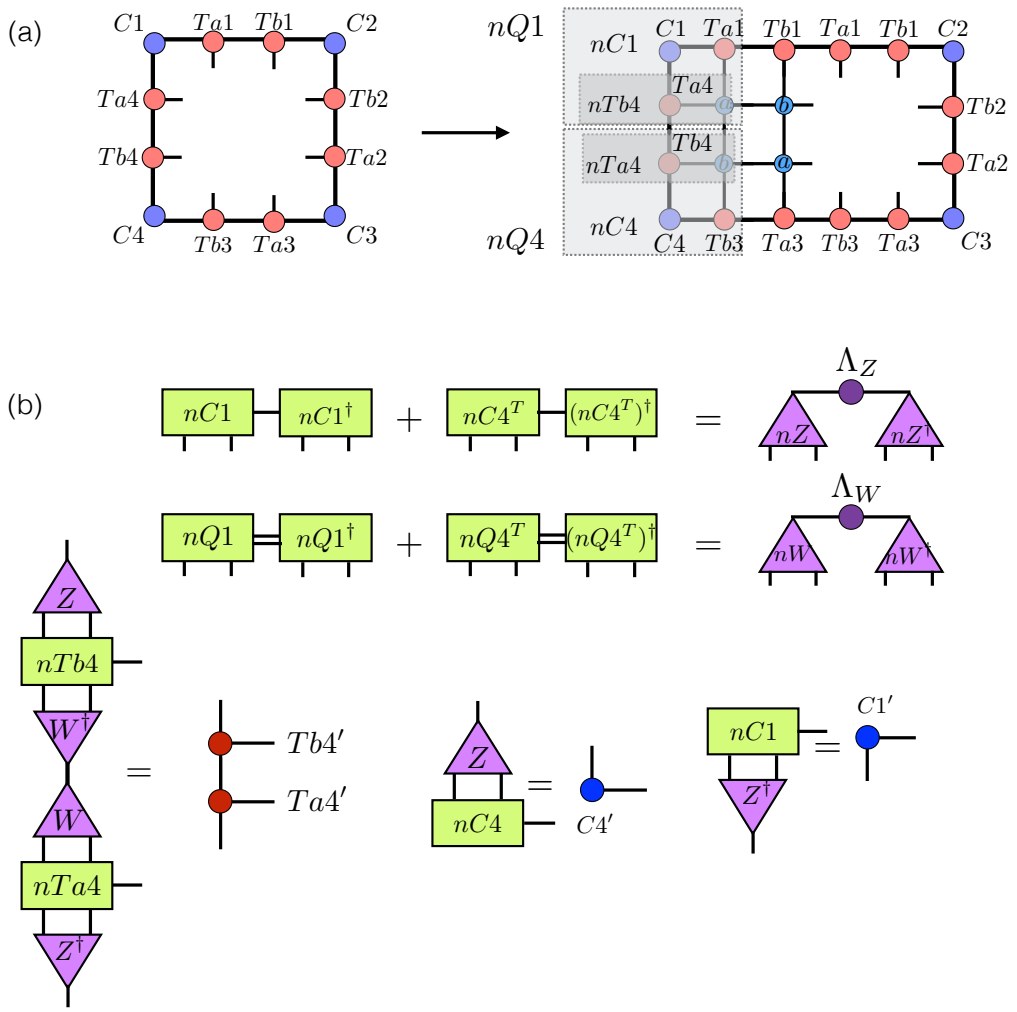

Figure C.5: (a) Inserting the tensors a and b for a two-site unit cell. (b) Defining the isometries nZ and nW which are then truncated afterwards and used for renormlization.

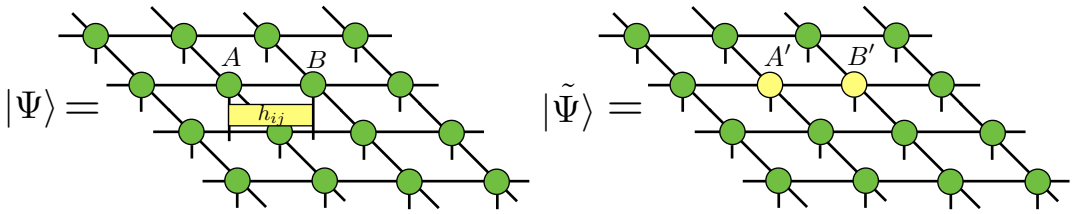

Figure C.6: $|\Psi\rangle$ is the state where we apply the two-body gate to the initial state. $|\tilde{\Psi}\rangle$ is the approximated state after absorbing the two-body gate.

C.3 Full and fast full update

Although the simple update scheme provides a very efficient mechanism for the simulations of several 2D quantum many-body systems, this method may be less accurate when it comes to studying critical systems close to quantum phase transitions that have large correlation lengths. This is because the simple update takes into account only the short range correlation between two tensors. It neglects the rest of the environment while making the update. The full update technique takes care of this by minimizing the distance between two states $|\Psi\rangle$ and $|\tilde{\Psi}\rangle$ defined in Fig. C.6 while taking into account the full environment of the tensors. $|\Psi\rangle$ is the original state where we apply the Hamiltonian link h_{ij} for one of the links and $|\tilde{\Psi}\rangle$ is the new approximated state after absorbing the two-body gate. We keep the bond dimensions of the two states to be equal. The target is to find new tensors for every update of a link that best approximates the original state by minimizing the distance δ defined as

$$\delta = \left\| |\Psi\rangle - |\tilde{\Psi}\rangle \right\|^2 = \langle\Psi|\Psi\rangle - \langle\Psi|\tilde{\Psi}\rangle - \langle\tilde{\Psi}|\Psi\rangle + \langle\tilde{\Psi}|\tilde{\Psi}\rangle. \tag{C.4}$$

This distance δ can be written in the form of a TN diagram as shown in Fig. C.7 where the blue tensors $\{E1, E2, E3, E4, E5, E6\}$ correspond to the environment of the tensors. We now start from some initial state $|\tilde{\Psi}_0\rangle$ where we fix all the tensors in the system except the tensor A' and find the minimum of δ with respect to A' i.e.

$$\min_{A'} \left\| |\Psi\rangle - |\tilde{\Psi}\rangle \right\|^2 = \min_{A'} \left(\vec{A'}^{\dagger} \mathcal{N} \vec{A'} - \vec{A'}^{\dagger} \vec{\mathcal{M}} - \vec{\mathcal{M}}^{\dagger} \vec{A'} + \mathcal{C} \right). \tag{C.5}$$

Here $\vec{A'}$ is a vector containing all the components of the tensor A'. $\mathcal{N}$ can be understood as a matrix after removing the tensors A' and A'^{*} from the last term of the right-hand side of Fig. C.7. Similarly, $\mathcal{M}$ and $\mathcal{C}$ can be obtained from this figure.

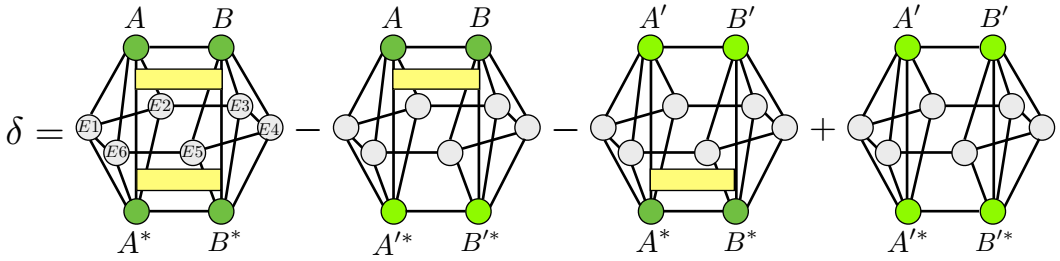

Figure C.7: The distance δ between the two states defined in Eq. C.4 can be written in terms of a TN. Here, the Grey tensors represent the environment of the tensors A and B before applying the two-body gate. A' and B' represent the approximated tensors that minimize the distance δ.

Now, in order to find the A' that minimizes the distance δ, we simply differentiate it with respect to A' and equate it to zero as follows

$$\frac{\partial}{\partial \vec{A'}^{\dagger}} \left(\vec{A'}^{\dagger} \mathcal{N} \vec{A'} - \vec{A'}^{\dagger} \vec{\mathcal{M}} - \vec{\mathcal{M}}^{\dagger} \vec{A'} + \mathcal{C} \right) = 0. \tag{C.6}$$

Solving this, we get

$$\mathcal{N} \vec{A'} = \vec{\mathcal{M}} \tag{C.7}$$

Thus, we obtain the first tensor A' which minimizes the distance between $|\Psi\rangle$ and $|\tilde{\Psi}\rangle$. Now, we can fix all the tensors except B' and find the optimal B'. This process needs to be repeated for all the links in our lattice. This will form one time step of our evolution. Repeating this step for a large number of times, until we get convergence in both A' and B', will give us the ground state of our Hamiltonian. This is the basic idea behind the full update scheme of iPEPS. This technique is not so computationally efficient because it requires us to recompute the environment of the tensors at every step of the algorithm. There are several techniques by which we can improve the efficiency of the full update scheme. One of them is that instead of recomputing the environment at every step of the algorithm, we re-use the environment of the previous tensors. This way, we need to compute the environment from scratch only once during the start of the algorithm. This is the main idea behind the fast full update scheme of iPEPS which we have implemented and also used during this thesis, but we refer the readers to Ref. [184] for details on the algorithm.

C.4 Operator entanglement entropy

In what follows we explain two procedures to compute $S_{op}(\rho)$: one fully taking into account the environment of the block, and one approximately taking into account

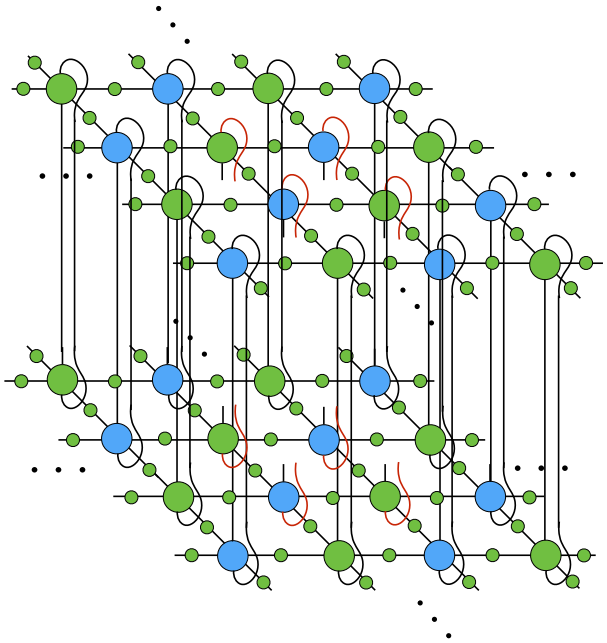

Figure C.8: TN for the operator $\sigma_\sharp$, obtained after tracing out the degrees of freedom of the environment of a 2×2 block in the vector $|\rho\rangle_\sharp$. We omit the name of the tensors for clarity of the diagram. Open indices of $\sigma_\sharp$ are shown in red.

some of the properties of the simple update.

Full calculation

The calculation taking into account the full environment follows the tensor contraction from Fig. C.8. In this case, we compute $\sigma_\sharp$ by tracing out the degrees of freedom outside the block, as shown in the figure. The corresponding contraction can be approximated in the thermodynamic limit using the CTM methods explained above.

Simple calculation

For the case of a phase with small correlation length, and using the information obtained from the simple update (namely, tensors at the sites and at the links), it is indeed possible to approximate, up to a good accuracy, the TN in Fig. C.8 by the one in Fig. C.9. In this approximation, one does not take the surrounding environment of the block fully into account. Instead, the effect of the environment is replaced by the effect of the λ tensors surrounding the block, which amounts to a mean-field approximation of the effective environment. Moreover, one can see that in such a case the eigenvalues of $\sigma_\sharp$ can be approximated with good accuracy by the product

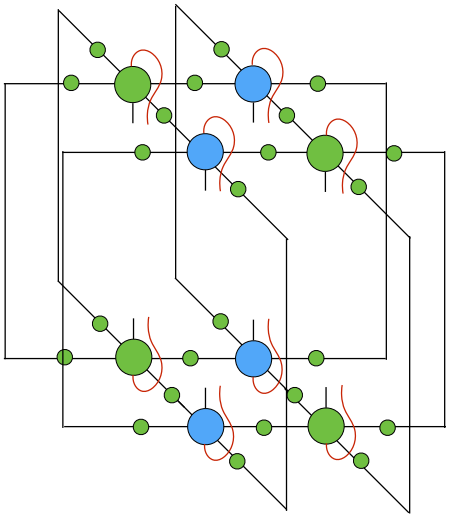

Figure C.9: TN for the operator $\sigma_\sharp$ for a 2×2 block in the vector $|\rho\rangle_\sharp$, with a mean-field approximation of the effective environment. We omit the name of the tensors for clarity of the diagram. Open indices of $\sigma_\sharp$ are shown in red.

of the squares of the surrounding λ tensors, i.e.,

$$eig(\sigma_\sharp) \approx \prod_{i \in \text{boundary}} \left(\lambda^{[i]}\right)^2, \tag{C.8}$$

and therefore the operator entanglement entropy reads

$$S_{op}(\rho) \approx \sum_{i \in \text{boundary}} S_{op}^{[i]} \tag{C.9}$$

with

$$S_{op}^{[i]} \equiv -\sum_{\alpha=1}^{D} \left(\lambda_\alpha^{[i]}\right)^2 \log \left(\lambda_\alpha^{[i]}\right)^2. \tag{C.10}$$

This approximation works very well in gapped phases computed via the simple update, and it is the one that we used in the main text.

List of Figures

List of Tables

Bibliography

[1] G. E. Moore, "Cramming more components onto integrated circuits," *Electronics*, vol. 38, no. 8, 1965.

[2] X.-G. Wen, "Topological orders in rigid states," *Int. J. Mod. Phys.*, vol. B4, no. 239, 1990.

[3] "The nobel prize in physics 2016," *Nobelprize.org*, 2017. [Online]. Available: http://www.nobelprize.org/nobel_prizes/physics/laureates/2016/

[4] A. Kitaev and C. Laumann, "Topological phases and quantum computation," *ArXiv e-prints*, Apr. 2009. [Online]. Available: http://adsabs.harvard.edu/abs/2009arXiv0904.2771K

[5] Aristotle, *Metaphysics*, vol. VIII, 350 B.C.E.

[6] [Online]. Available: https://en.wikipedia.org/wiki/Observable_universe#Matter_content

[7] J. Cullum and R. Willoughby, "Lanczos Algorithms for Large Symmetric Eigenvalue Computations," *Society for Industrial and Applied Mathematics*, vol. 1, 2002.

[8] M. P. Nightingale and J. C. Umrigar, "Quantum Monte Carlo Methods in Physics and Chemistry," *Springer*, 1999.

[9] J. Oitmaa, C. Hamer, and W. Zheng, "Series Expansion Methods for Strongly Interacting Lattice Models," *Cambridge University Press*, 2006.

[10] J. Stein, "Flow equations and the strong-coupling expansion for the hubbard model," *Journal of Statistical Physics*, vol. 88, no. 1, pp. 487–511, Jul 1997. [Online]. Available: https://doi.org/10.1007/BF02508481

[11] C. Knetter and G. Uhrig, "Perturbation theory by flow equations: dimerized and frustrated s = 1/2 chain," *The European Physical Journal B - Condensed Matter and Complex Systems*, vol. 13, no. 2, pp. 209–225, Jan 2000. [Online]. Available: https://doi.org/10.1007/s100510050026

[12] R. Orús, "A practical introduction to tensor networks: Matrix product states and projected entangled pair states," *Annals of Physics*, vol. 349, pp. 117 – 158, 2014. [Online]. Available: http://www.sciencedirect.com/science/article/pii/S0003491614001596

[13] V. Vedral, "Mean-field approximations and multipartite thermal correlations," *New Journal of Physics*, vol. 6, no. 1, p. 22, 2004. [Online]. Available: http://stacks.iop.org/1367-2630/6/i=1/a=022

[14] D. V. Else, I. Schwarz, S. D. Bartlett, and A. C. Doherty, "Symmetry-protected phases for measurement-based quantum computation," *Phys. Rev. Lett.*, vol. 108, p. 240505, Jun 2012. [Online]. Available: https://link.aps.org/doi/10.1103/PhysRevLett.108.240505

[15] H. P. Nautrup and T.-C. Wei, "Symmetry-protected topologically ordered states for universal quantum computation," *Phys. Rev. A*, vol. 92, p. 052309, Nov 2015. [Online]. Available: https://link.aps.org/doi/10.1103/PhysRevA.92.052309

[16] F. Verstraete, M. A. Martín-Delgado, and J. I. Cirac, "Diverging entanglement length in gapped quantum spin systems," *Phys. Rev. Lett.*, vol. 92, p. 087201, Feb 2004. [Online]. Available: https://link.aps.org/doi/10.1103/PhysRevLett.92.087201

[17] P. W. Anderson, *RVB Theory of High Tc Superconductivity*. Boston, MA: Springer US, 1987, pp. 295–299. [Online]. Available: https://doi.org/10.1007/978-1-4613-1937-5_32

[18] S. Diehl, E. Rico, M. A. Baranov, and P. Zoller, "Topology by dissipation in atomic quantum wires," *Nature Physics*, vol. 7, pp. 971–977, Dec. 2011.

[19] F. Verstraete, M. M. Wolf, and J. I. Cirac, "Quantum computation, quantum state engineering, and quantum phase transitions driven by dissipation," *ArXiv e-prints*, Mar. 2008.

[20] "The nobel prize in physics 1921," *Nobelprize.org*. [Online]. Available: http://www.nobelprize.org/nobel_prizes/physics/laureates/1921/

[21] A. Einstein, B. Podolsky, and N. Rosen, "Can Quantum-Mechanical Description of Physical Reality Be Considered Complete?" *Physical Review*, vol. 47, pp. 777–780, May 1935.

[22] J. Bell, "On the einstein podolsky rosen paradox," *Physics*, vol. 1, pp. 195–200, 1964.

[23] A. Aspect, P. Grangier, and G. Roger, "Experimental Realization of Einstein-Podolsky-Rosen-Bohm Gedankenexperiment: A New Violation of Bell's Inequalities," *Physical Review Letters*, vol. 49, pp. 91–94, Jul. 1982.

[24] J. F. Clauser, M. A. Horne, A. Shimony, and R. A. Holt, "Proposed Experiment to Test Local Hidden-Variable Theories," *Physical Review Letters*, vol. 23, pp. 880–884, Oct. 1969.

[25] B. e. a. Hensen, "Loophole-free Bell inequality violation using electron spins separated by 1.3 kilometres," *Nature*, vol. 526, pp. 682–686, Oct. 2015.

[26] S. J. Freedman and J. F. Clauser, "Experimental Test of Local Hidden-Variable Theories," *Physical Review Letters*, vol. 28, pp. 938–941, Apr. 1972.

[27] A. Aspect, P. Grangier, and G. Roger, "Experimental Tests of Realistic Local Theories via Bell's Theorem," *Physical Review Letters*, vol. 47, pp. 460–463, Aug. 1981.

[28] A. Aspect, J. Dalibard, and G. Roger, "Experimental Test of Bell's Inequalities Using Time- Varying Analyzers," *Physical Review Letters*, vol. 49, pp. 1804–1807, Dec. 1982.

[29] D. Boschi, S. Branca, F. de Martini, L. Hardy, and S. Popescu, "Experimental Realization of Teleporting an Unknown Pure Quantum State via Dual Classical and Einstein-Podolsky-Rosen Channels," *Physical Review Letters*, vol. 80, pp. 1121–1125, Feb. 1998.

[30] P. W. Shor, "Algorithms for quantum computation: discrete logarithms and factoring." *Proceedings of the 35th Annual Symposium on Fundations of Computer Science*, 1994.

[31] L. K. Grover, "A fast quantum mechanical algorithm for database search." *Proceedings of the 28th Annual ACM Symposium on the Theory of Computing*, p. 212, 1996.

[32] M. W. J. et al, "Quantum annealing with manufactured spins." *Nature*, 2011.

[33] U. Vazirani, "Shtetl-Optimized: D-Wave Easter Spectacular." *The Blog of Scott Aaronson*, 2007. [Online]. Available: http://www.scottaaronson.com/blog/?p=225

[34] S. Aaronson, "The Orion Quantum Computer Anti-Hype FAQ." *The Blog of Scott Aaronson*, 2007. [Online]. Available: http://www.scottaaronson.com/blog/?p=198

[35] "The nobel prize in physics 2012," *Nobelprize.org*, 2012. [Online]. Available: http://www.nobelprize.org/nobel_prizes/physics/laureates/2012/

[36] M. Reynolds, "Quantum simulator with 51 qubits is largest ever." *NewScientist*, July 2017. [Online]. Available: https://www.newscientist.com/article/2141105-quantum-simulator-with-51-qubits-is-largest-ever/

[37] C. H. Benett and G. Brassard, "Quantum cryptography: Public key distribution and coin tossing," *Proceedings of IEEE International Conference on Computers, Systems and Signal Processing*, vol. 175, 1984.

[38] K. Życzkowski, P. Horodecki, A. Sanpera, and M. Lewenstein, "Volume of the set of separable states," *Phys. Rev. A*, vol. 58, pp. 883–892, Aug 1998. [Online]. Available: https://link.aps.org/doi/10.1103/PhysRevA.58.883

[39] J. Eisert, "Entanglement in quantum information theory," Ph.D. dissertation, PhD Thesis, 2006.

[40] A. Rényi, "On measures of information and entropy." *Proceedings of the fourth Berkeley Symposium on Mathematics, Statistics and Probability*, pp. 547–561, 1960.

[41] J. Eisert and M. Cramer, "Single-copy entanglement in critical quantum spin chains," *Phys. Rev. A*, vol. 72, p. 042112, Oct 2005. [Online]. Available: https://link.aps.org/doi/10.1103/PhysRevA.72.042112

[42] I. Peschel and J. Zhao, "On single-copy entanglement," *Journal of Statistical Mechanics: Theory and Experiment*, vol. 2005, no. 11, p. P11002, 2005. [Online]. Available: http://stacks.iop.org/1742-5468/2005/i=11/a=P11002

[43] T.-C. Wei and P. M. Goldbart, "Geometric measure of entanglement and applications to bipartite and multipartite quantum states," *Phys. Rev. A*, vol. 68, p. 042307, Oct 2003. [Online]. Available: https://link.aps.org/doi/10.1103/PhysRevA.68.042307

[44] V. Coffman, J. Kundu, and W. K. Wootters, "Distributed entanglement," *Phys. Rev. A*, vol. 61, p. 052306, Apr 2000. [Online]. Available: https://link.aps.org/doi/10.1103/PhysRevA.61.052306

[45] S. R. White, "Density matrix formulation for quantum renormalization groups," *Phys. Rev. Lett.*, vol. 69, pp. 2863–2866, Nov 1992. [Online]. Available: https://link.aps.org/doi/10.1103/PhysRevLett.69.2863

[46] ——, "Density-matrix algorithms for quantum renormalization groups," *Phys. Rev. B*, vol. 48, pp. 10 345–10 356, Oct 1993. [Online]. Available: https://link.aps.org/doi/10.1103/PhysRevB.48.10345

[47] P. Corboz, "Variational optimization with infinite projected entangled-pair states," *Phys. Rev. B*, vol. 94, p. 035133, Jul 2016. [Online]. Available: https://link.aps.org/doi/10.1103/PhysRevB.94.035133

[48] I. P. McCulloch, "Infinite size density matrix renormalization group, revisited," *ArXiv e-prints*, Apr. 2008.

[49] G. M. Crosswhite, A. C. Doherty, and G. Vidal, "Applying matrix product operators to model systems with long-range interactions," *Phys. Rev. B*, vol. 78, p. 035116, Jul 2008. [Online]. Available: https://link.aps.org/doi/10.1103/PhysRevB.78.035116

[50] J. Jordan, R. Orús, G. Vidal, F. Verstraete, and J. I. Cirac, "Classical simulation of infinite-size quantum lattice systems in two spatial dimensions," *Phys. Rev. Lett.*, vol. 101, p. 250602, Dec 2008. [Online]. Available: https://link.aps.org/doi/10.1103/PhysRevLett.101.250602

[51] R. Orús and G. Vidal, "Simulation of two-dimensional quantum systems on an infinite lattice revisited: Corner transfer matrix for tensor

contraction," *Phys. Rev. B*, vol. 80, p. 094403, Sep 2009. [Online]. Available: https://link.aps.org/doi/10.1103/PhysRevB.80.094403

[52] ——, "Infinite time-evolving block decimation algorithm beyond unitary evolution," *Phys. Rev. B*, vol. 78, p. 155117, Oct 2008. [Online]. Available: https://link.aps.org/doi/10.1103/PhysRevB.78.155117

[53] P. Pippan, S. R. White, and H. G. Evertz, "Efficient matrix-product state method for periodic boundary conditions," *Phys. Rev. B*, vol. 81, p. 081103, Feb 2010. [Online]. Available: https://link.aps.org/doi/10.1103/PhysRevB.81.081103

[54] B. Pirvu, F. Verstraete, and G. Vidal, "Exploiting translational invariance in matrix product state simulations of spin chains with periodic boundary conditions," *Phys. Rev. B*, vol. 83, p. 125104, Mar 2011. [Online]. Available: https://link.aps.org/doi/10.1103/PhysRevB.83.125104

[55] F. Verstraete, D. Porras, and J. I. Cirac, "Density matrix renormalization group and periodic boundary conditions: A quantum information perspective," *Phys. Rev. Lett.*, vol. 93, p. 227205, Nov 2004. [Online]. Available: https://link.aps.org/doi/10.1103/PhysRevLett.93.227205

[56] I. P. McCulloch and M. Gulcsi, "The non-abelian density matrix renormalization group algorithm," *EPL (Europhysics Letters)*, vol. 57, no. 6, p. 852, 2002. [Online]. Available: http://stacks.iop.org/0295-5075/57/i=6/a=852

[57] S. Singh, R. N. C. Pfeifer, and G. Vidal, "Tensor network states and algorithms in the presence of a global u(1) symmetry," *Phys. Rev. B*, vol. 83, p. 115125, Mar 2011. [Online]. Available: https://link.aps.org/doi/10.1103/PhysRevB.83.115125

[58] V. Murg, F. Verstraete, and J. I. Cirac, "Variational study of hard-core bosons in a two-dimensional optical lattice using projected entangled pair states," *Phys. Rev. A*, vol. 75, p. 033605, Mar 2007. [Online]. Available: https://link.aps.org/doi/10.1103/PhysRevA.75.033605

[59] J. Jordan, R. Orús, and G. Vidal, "Numerical study of the hard-core bose-hubbard model on an infinite square lattice," *Phys. Rev. B*, vol. 79, p. 174515, May 2009. [Online]. Available: https://link.aps.org/doi/10.1103/PhysRevB.79.174515

[60] P. Corboz, G. Evenbly, F. Verstraete, and G. Vidal, "Simulation of interacting fermions with entanglement renormalization," *Phys. Rev. A*, vol. 81, p. 010303, Jan 2010. [Online]. Available: https://link.aps.org/doi/10.1103/PhysRevA.81.010303

[61] C. V. Kraus, N. Schuch, F. Verstraete, and J. I. Cirac, "Fermionic projected entangled pair states," *Phys. Rev. A*, vol. 81, p. 052338, May 2010. [Online]. Available: https://link.aps.org/doi/10.1103/PhysRevA.81.052338

[62] C. Pineda, T. Barthel, and J. Eisert, "Unitary circuits for strongly correlated fermions," *Phys. Rev. A*, vol. 81, p. 050303, May 2010. [Online]. Available: https://link.aps.org/doi/10.1103/PhysRevA.81.050303

[63] V. Murg, F. Verstraete, and J. I. Cirac, "Exploring frustrated spin systems using projected entangled pair states," *Phys. Rev. B*, vol. 79, p. 195119, May 2009. [Online]. Available: https://link.aps.org/doi/10.1103/PhysRevB.79.195119

[64] G. Evenbly and G. Vidal, "Frustrated antiferromagnets with entanglement renormalization: Ground state of the spin-$\frac{1}{2}$ heisenberg model on a kagome lattice," *Phys. Rev. Lett.*, vol. 104, p. 187203, May 2010. [Online]. Available: https://link.aps.org/doi/10.1103/PhysRevLett.104.187203

[65] S. Yan, D. A. Huse, and S. R. White, "Spin-Liquid Ground State of the S = 1/2 Kagome Heisenberg Antiferromagnet," *Science*, vol. 332, p. 1173, Jun. 2011.

[66] L. Wang, Z.-C. Gu, F. Verstraete, and X.-G. Wen, "Tensor-product state approach to spin-$\frac{1}{2}$ square J_1-J_2 antiferromagnetic heisenberg model: Evidence for deconfined quantum criticality," *Phys. Rev. B*, vol. 94, p. 075143, Aug 2016. [Online]. Available: https://link.aps.org/doi/10.1103/PhysRevB.94.075143

[67] F. Verstraete, J. J. García-Ripoll, and J. I. Cirac, "Matrix product density operators: Simulation of finite-temperature and dissipative systems," *Phys. Rev. Lett.*, vol. 93, p. 207204, Nov 2004. [Online]. Available: https://link.aps.org/doi/10.1103/PhysRevLett.93.207204

[68] M. Zwolak and G. Vidal, "Mixed-state dynamics in one-dimensional quantum lattice systems: A time-dependent superoperator renormalization algorithm," *Phys. Rev. Lett.*, vol. 93, p. 207205, Nov 2004. [Online]. Available: https://link.aps.org/doi/10.1103/PhysRevLett.93.207205

[69] J. Maldacena, "The Large-N Limit of Superconformal Field Theories and Supergravity," *International Journal of Theoretical Physics*, vol. 38, pp. 1113–1133, 1999.

[70] S. S. Gubser, I. R. Klebanov, and A. M. Polyakov, "Gauge theory correlators from non-critical string theory," *Physics Letters B*, vol. 428, pp. 105–114, May 1998.

[71] E. Witten, "Anti-de Sitter space and holography," *Advances in Theoretical and Mathematical Physics*, vol. 2, pp. 253–291, 1998.

[72] S. Ryu and T. Takayanagi, "Holographic derivation of entanglement entropy from the anti˘de sitter space/conformal field theory correspondence," *Phys. Rev. Lett.*, vol. 96, p. 181602, May 2006. [Online]. Available: https://link.aps.org/doi/10.1103/PhysRevLett.96.181602

[73] B. Swingle, "Entanglement renormalization and holography," *Phys. Rev. D*, vol. 86, p. 065007, Sep 2012. [Online]. Available: https://link.aps.org/doi/10.1103/PhysRevD.86.065007

[74] J. Molina-Vilaplana, "Holographic geometries of one-dimensional gapped quantum systems from tensor network states," *Journal of High Energy Physics*, vol. 2013, no. 5, p. 24, May 2013. [Online]. Available: https://doi.org/10.1007/JHEP05(2013)024

[75] O. Legeza and J. Sólyom, "Optimizing the density-matrix renormalization group method using quantum information entropy," *Phys. Rev. B*, vol. 68, p. 195116, Nov 2003. [Online]. Available: https://link.aps.org/doi/10.1103/PhysRevB.68.195116

[76] J. Rissler, R. M. Noack, and S. R. White, "Measuring orbital interaction using quantum information theory," *Chemical Physics*, vol. 323, pp. 519–531, Apr. 2006.

[77] G. Vidal, "Efficient classical simulation of slightly entangled quantum computations," *Phys. Rev. Lett.*, vol. 91, p. 147902, Oct 2003. [Online]. Available: https://link.aps.org/doi/10.1103/PhysRevLett.91.147902

[78] G. Vidal, "Efficient Simulation of One-Dimensional Quantum Many-Body Systems," *Physical Review Letters*, vol. 93, no. 4, p. 040502, Jul. 2004.

[79] G. Vidal, "Classical simulation of infinite-size quantum lattice systems in one spatial dimension," *Phys. Rev. Lett.*, vol. 98, p. 070201, Feb 2007. [Online]. Available: https://link.aps.org/doi/10.1103/PhysRevLett.98.070201

[80] F. Verstraete and J. I. Cirac, "Renormalization algorithms for Quantum-Many Body Systems in two and higher dimensions," *eprint arXiv:cond-mat/0407066*, Jul. 2004. [Online]. Available: http://adsabs.harvard.edu/abs/2004cond.mat..7066V

[81] M. Levin and C. P. Nave, "Tensor renormalization group approach to two-dimensional classical lattice models," *Phys. Rev. Lett.*, vol. 99, p. 120601, Sep 2007. [Online]. Available: https://link.aps.org/doi/10.1103/PhysRevLett.99.120601

[82] G. Evenbly and G. Vidal, "Class of highly entangled many-body states that can be efficiently simulated," *Phys. Rev. Lett.*, vol. 112, p. 240502, Jun 2014. [Online]. Available: https://link.aps.org/doi/10.1103/PhysRevLett.112.240502

[83] F. Verstraete and J. I. Cirac, "Continuous Matrix Product States for Quantum Fields," *Physical Review Letters*, vol. 104, no. 19, p. 190405, May 2010.

[84] J. Haegeman, J. I. Cirac, T. J. Osborne, H. Verschelde, and F. Verstraete, "Applying the variational principle to $(1+1)$-dimensional quantum field theories," *Phys. Rev. Lett.*, vol. 105, p. 251601, Dec 2010. [Online]. Available: https://link.aps.org/doi/10.1103/PhysRevLett.105.251601

[85] Z. Y. Xie, J. Chen, M. P. Qin, J. W. Zhu, L. P. Yang, and T. Xiang, "Coarse-graining renormalization by higher-order singular value decomposition," *Phys. Rev. B*, vol. 86, p. 045139, Jul 2012. [Online]. Available: https://link.aps.org/doi/10.1103/PhysRevB.86.045139

[86] U. Schollwöck, "The density-matrix renormalization group," *Rev. Mod. Phys.*, vol. 77, pp. 259–315, Apr 2005. [Online]. Available: https://link.aps.org/doi/10.1103/RevModPhys.77.259

[87] ——, "The density-matrix renormalization group in the age of matrix product states," *Annals of Physics*, vol. 326, no. 1, pp. 96 – 192, 2011, january 2011 Special Issue. [Online]. Available: http://www.sciencedirect.com/science/article/pii/S0003491610001752

[88] M. B. Plenio, J. Eisert, J. Dreißig, and M. Cramer, "Entropy, entanglement, and area: Analytical results for harmonic lattice systems," *Phys. Rev. Lett.*, vol. 94, p. 060503, Feb 2005. [Online]. Available: https://link.aps.org/doi/10.1103/PhysRevLett.94.060503

[89] M. Srednicki, "Entropy and area," *Phys. Rev. Lett.*, vol. 71, pp. 666–669, Aug 1993. [Online]. Available: https://link.aps.org/doi/10.1103/PhysRevLett.71.666

[90] P. Calabrese and J. Cardy, "Entanglement entropy and quantum field theory," *Journal of Statistical Mechanics: Theory and Experiment*, vol. 2004, no. 06, p. P06002, 2004. [Online]. Available: http://stacks.iop.org/1742-5468/2004/i=06/a=P06002

[91] M. B. Hastings, "Solving gapped hamiltonians locally," *Phys. Rev. B*, vol. 73, p. 085115, Feb 2006. [Online]. Available: https://link.aps.org/doi/10.1103/PhysRevB.73.085115

[92] M. M. Wolf, F. Verstraete, M. B. Hastings, and J. I. Cirac, "Area laws in quantum systems: Mutual information and correlations," *Phys. Rev. Lett.*, vol. 100, p. 070502, Feb 2008. [Online]. Available: https://link.aps.org/doi/10.1103/PhysRevLett.100.070502

[93] Y. Ge and J. Eisert, "Area laws and efficient descriptions of quantum many-body states," *New Journal of Physics*, vol. 18, no. 8, p. 083026, 2016. [Online]. Available: http://stacks.iop.org/1367-2630/18/i=8/a=083026

[94] J. Eisert, "Entanglement and tensor network states," *ArXiv e-prints*, Aug. 2013. [Online]. Available: http://adsabs.harvard.edu/abs/2013arXiv1308.3318E

[95] N. Schuch, "Condensed Matter Applications of Entanglement Theory," *ArXiv e-prints*, Jun. 2013. [Online]. Available: http://adsabs.harvard.edu/abs/2013arXiv1306.5551S

[96] J. I. Cirac and F. Verstraete, "Renormalization and tensor product states in spin chains and lattices," *Journal of Physics A: Mathematical and Theoretical*, vol. 42, no. 50, p. 504004, 2009. [Online]. Available: http://stacks.iop.org/1751-8121/42/i=50/a=504004

[97] F. Verstraete, V. Murg, and J. Cirac, "Matrix product states, projected entangled pair states, and variational renormalization group methods for quantum spin systems," *Advances in Physics*, vol. 57, no. 2, pp. 143–224, 2008. [Online]. Available: http://dx.doi.org/10.1080/14789940801912366

[98] M. Fannes, B. Nachtergaele, and R. F. Werner, "Finitely correlated states on quantum spin chains," *Communications in Mathematical Physics*, vol. 144, no. 3, pp. 443–490, Mar 1992. [Online]. Available: https://doi.org/10.1007/BF02099178

[99] A. Klmper, A. Schadschneider, and J. Zittartz, "Matrix product ground states for one-dimensional spin-1 quantum antiferromagnets," *EPL (Europhysics Letters)*, vol. 24, no. 4, p. 293, 1993. [Online]. Available: http://stacks.iop.org/0295-5075/24/i=4/a=010

[100] T. Nishino and K. Okunishi, "Product wave function renormalization group," *Journal of the Physical Society of Japan*, vol. 64, no. 11, pp. 4084–4087, 1995. [Online]. Available: http://dx.doi.org/10.1143/JPSJ.64.4084

[101] D. M. Greenberger, M. A. Horne, and A. Zeilinger, "Going Beyond Bell's Theorem," *ArXiv e-prints*, Dec. 2007.

[102] I. Affleck, T. Kennedy, E. H. Lieb, and H. Tasaki, "Valence bond ground states in isotropic quantum antiferromagnets," *Communications in Mathematical Physics*, vol. 115, no. 3, pp. 477–528, Sep 1988. [Online]. Available: https://doi.org/10.1007/BF01218021

[103] ——, "Rigorous results on valence-bond ground states in antiferromagnets," *Phys. Rev. Lett.*, vol. 59, pp. 799–802, Aug 1987. [Online]. Available: https://link.aps.org/doi/10.1103/PhysRevLett.59.799

[104] F. D. M. Haldane, "Nonlinear field theory of large-spin heisenberg antiferromagnets: Semiclassically quantized solitons of the one-dimensional easy-axis néel state," *Phys. Rev. Lett.*, vol. 50, pp. 1153–1156, Apr 1983. [Online]. Available: https://link.aps.org/doi/10.1103/PhysRevLett.50.1153

[105] F. Haldane, "Continuum dynamics of the 1-d heisenberg antiferromagnet: Identification with the o(3) nonlinear sigma model," *Physics Letters A*, vol. 93, no. 9, pp. 464 – 468, 1983. [Online]. Available: http://www.sciencedirect.com/science/article/pii/037596018390631X

[106] Z.-C. Gu and X.-G. Wen, "Tensor-entanglement-filtering renormalization approach and symmetry-protected topological order," *Phys. Rev. B*, vol. 80, p. 155131, Oct 2009. [Online]. Available: https://link.aps.org/doi/10.1103/PhysRevB.80.155131

[107] Z. Y. Xie, H. C. Jiang, Q. N. Chen, Z. Y. Weng, and T. Xiang, "Second renormalization of tensor-network states," *Phys. Rev. Lett.*, vol. 103, p. 160601, Oct 2009. [Online]. Available: https://link.aps.org/doi/10.1103/PhysRevLett.103.160601

[108] T. Nishino and K. Okunishi, "Corner transfer matrix renormalization group method," *Journal of the Physical Society of Japan*, vol. 65, no. 4, pp. 891–894, 1996. [Online]. Available: http://dx.doi.org/10.1143/JPSJ.65.891

[109] ——, "Corner transfer matrix algorithm for classical renormalization group," *Journal of the Physical Society of Japan*, vol. 66, no. 10, pp. 3040–3047, 1997. [Online]. Available: http://dx.doi.org/10.1143/JPSJ.66.3040

[110] R. Orús, "Exploring corner transfer matrices and corner tensors for the classical simulation of quantum lattice systems," *Phys. Rev. B*, vol. 85, p. 205117, May 2012. [Online]. Available: https://link.aps.org/doi/10.1103/PhysRevB.85.205117

[111] F. Verstraete, M. M. Wolf, D. Perez-Garcia, and J. I. Cirac, "Criticality, the area law, and the computational power of projected entangled pair states," *Phys. Rev. Lett.*, vol. 96, p. 220601, Jun 2006. [Online]. Available: https://link.aps.org/doi/10.1103/PhysRevLett.96.220601

[112] N. Schuch, M. M. Wolf, F. Verstraete, and J. I. Cirac, "Computational complexity of projected entangled pair states," *Phys. Rev. Lett.*, vol. 98, p. 140506, Apr 2007. [Online]. Available: https://link.aps.org/doi/10.1103/PhysRevLett.98.140506

[113] A. Kitaev, "Fault-tolerant quantum computation by anyons," *Annals of Physics*, vol. 303, no. 1, pp. 2 – 30, 2003. [Online]. Available: http://www.sciencedirect.com/science/article/pii/S0003491602000180

[114] Y.-Y. Shi, L.-M. Duan, and G. Vidal, "Classical simulation of quantum many-body systems with a tree tensor network," *Phys. Rev. A*, vol. 74,

p. 022320, Aug 2006. [Online]. Available: https://link.aps.org/doi/10.1103/PhysRevA.74.022320

[115] L. Tagliacozzo, G. Evenbly, and G. Vidal, "Simulation of two-dimensional quantum systems using a tree tensor network that exploits the entropic area law," *Phys. Rev. B*, vol. 80, p. 235127, Dec 2009. [Online]. Available: https://link.aps.org/doi/10.1103/PhysRevB.80.235127

[116] P. Silvi, V. Giovannetti, S. Montangero, M. Rizzi, J. I. Cirac, and R. Fazio, "Homogeneous binary trees as ground states of quantum critical hamiltonians," *Phys. Rev. A*, vol. 81, p. 062335, Jun 2010. [Online]. Available: https://link.aps.org/doi/10.1103/PhysRevA.81.062335

[117] Z. Y. Xie, J. Chen, J. F. Yu, X. Kong, B. Normand, and T. Xiang, "Tensor renormalization of quantum many-body systems using projected entangled simplex states," *Phys. Rev. X*, vol. 4, p. 011025, Feb 2014. [Online]. Available: https://link.aps.org/doi/10.1103/PhysRevX.4.011025

[118] G. Vidal, "Entanglement renormalization," *Phys. Rev. Lett.*, vol. 99, p. 220405, Nov 2007. [Online]. Available: https://link.aps.org/doi/10.1103/PhysRevLett.99.220405

[119] R. Orús, "Advances on tensor network theory: symmetries, fermions, entanglement, and holography," *The European Physical Journal B*, vol. 87, no. 11, p. 280, Nov 2014. [Online]. Available: https://doi.org/10.1140/epjb/e2014-50502-9

[120] H. Bethe, "Zur theorie der meta lie. eigenwerte und eigenfunktionen der linearen atomkette." *Z. Phys.*, vol. 71, p. 205, 1931.

[121] Y. Ajiro, T. Goto, H. Kikuchi, T. Sakakibara, and T. Inami, "High-field magnetization of a quasi-one-dimensional s=1 antiferromagnet $ni(c_2h_8n_2)_2no_2(clo_4$: Observation of the haldane gap," *Phys. Rev. Lett.*, vol. 63, pp. 1424–1427, Sep 1989. [Online]. Available: https://link.aps.org/doi/10.1103/PhysRevLett.63.1424

[122] R. Botet, R. Jullien, and M. Kolb, "Finite-size-scaling study of the spin-1 heisenberg-ising chain with uniaxial anisotropy," *Phys. Rev. B*, vol. 28, pp. 3914–3921, Oct 1983. [Online]. Available: https://link.aps.org/doi/10.1103/PhysRevB.28.3914

[123] W. J. L. Buyers, R. M. Morra, R. L. Armstrong, M. J. Hogan, P. Gerlach, Hirakawa, and K., "Experimental evidence for the haldane gap in a spin-1 nearly isotropic, antiferromagnetic chain," *Phys. Rev. Lett.*, vol. 56, pp. 371–374, Jan 1986. [Online]. Available: https://link.aps.org/doi/10.1103/PhysRevLett.56.371

[124] M. Hagiwara, K. Katsumata, I. Affleck, B. I. Halperin, and J. P. Renard, "Observation of s=1/2 degrees of freedom in an s=1 linear-chain heisenberg antiferromagnet," *Phys. Rev. Lett.*, vol. 65, pp. 3181–3184, Dec 1990. [Online]. Available: https://link.aps.org/doi/10.1103/PhysRevLett.65.3181

[125] K. Katsumata, H. Hori, T. Takeuchi, M. Date, A. Yamagishi, and J. P. Renard, "Magnetization process of an s=1 linear-chain heisenberg antiferromagnet," *Phys. Rev. Lett.*, vol. 63, pp. 86–88, Jul 1989. [Online]. Available: https://link.aps.org/doi/10.1103/PhysRevLett.63.86

[126] M. P. Nightingale and H. W. J. Blöte, "Gap of the linear spin-1 heisenberg antiferromagnet: A monte carlo calculation," *Phys. Rev. B*, vol. 33, pp. 659–661, Jan 1986. [Online]. Available: https://link.aps.org/doi/10.1103/PhysRevB.33.659

[127] T. Sakai and M. Takahashi, "Energy gap of the s=1 antiferromagnetic heisenberg chain," *Phys. Rev. B*, vol. 42, pp. 1090–1092, Jul 1990. [Online]. Available: https://link.aps.org/doi/10.1103/PhysRevB.42.1090

[128] M. Takahashi, "Monte carlo calculation of elementary excitation of spin chains," *Phys. Rev. Lett.*, vol. 62, pp. 2313–2316, May 1989. [Online]. Available: https://link.aps.org/doi/10.1103/PhysRevLett.62.2313

[129] E. Lieb, T. Schultz, and D. Mattis, "Two soluble models of an antiferromagnetic chain," *Annals of Physics*, vol. 16, no. 3, pp. 407 – 466, 1961. [Online]. Available: http://www.sciencedirect.com/science/article/pii/0003491661901154

[130] M. Kolb, "Symmetry and boundary condition of planar spin systems," *Phys. Rev. B*, vol. 31, pp. 7494–7496, Jun 1985. [Online]. Available: https://link.aps.org/doi/10.1103/PhysRevB.31.7494

[131] L. Landau, *Phys. Z. Sowjetunion*, vol. 11, p. 26, 1937.

[132] M. den Nijs and K. Rommelse, "Preroughening transitions in crystal surfaces and valence-bond phases in quantum spin chains," *Phys. Rev. B*, vol. 40, pp. 4709–4734, Sep 1989. [Online]. Available: https://link.aps.org/doi/10.1103/PhysRevB.40.4709

[133] F. Pollmann, A. M. Turner, E. Berg, and M. Oshikawa, "Entanglement spectrum of a topological phase in one dimension," *Phys. Rev. B*, vol. 81, p. 064439, Feb 2010. [Online]. Available: https://link.aps.org/doi/10.1103/PhysRevB.81.064439

[134] B. Schwarzschild, "Physics Nobel Prize goes to Tsui, Stormer and Laughlin for the fractional quantum Hall effect," *Physics Today*, vol. 51, pp. 17–19, Dec. 1998.

[135] Y. Fuji, F. Pollmann, and M. Oshikawa, "Distinct trivial phases protected by a point-group symmetry in quantum spin chains," *Phys. Rev. Lett.*, vol. 114, p. 177204, May 2015. [Online]. Available: https://link.aps.org/doi/10.1103/PhysRevLett.114.177204

[136] M. Oshikawa, "Hidden z 2 *z 2 symmetry in quantum spin chains with arbitrary integer spin," *Journal of Physics: Condensed Matter*, vol. 4, no. 36, p. 7469, 1992. [Online]. Available: http://stacks.iop.org/0953-8984/4/i=36/a=019

[137] T. Tonegawa, K. Okamoto, H. Nakano, T. Sakai, K. Nomura, and M. Kaburagi, "Haldane, large-d, and intermediate-d states in an s = 2 quantum spin chain with on-site and xxz anisotropies," *Journal of the Physical Society of Japan*, vol. 80, no. 4, p. 043001, 2011. [Online]. Available: http://dx.doi.org/10.1143/JPSJ.80.043001

[138] J. A. Kjäll, M. P. Zaletel, R. S. K. Mong, J. H. Bardarson, and F. Pollmann, "The phase diagram of the anisotropic spin-2 XXZ model: an infinite system DMRG study," *ArXiv e-prints*, Dec. 2012.

[139] H.-H. Tu and R. Orús, "Intermediate haldane phase in spin-2 quantum chains with uniaxial anisotropy," *Phys. Rev. B*, vol. 84, p. 140407, Oct 2011. [Online]. Available: https://link.aps.org/doi/10.1103/PhysRevB.84.140407

[140] Z.-X. Liu, X. Chen, and X.-G. Wen, "Symmetry-protected topological orders of one-dimensional spin systems with $D_2 + t$ symmetry," *Phys.*

Rev. B, vol. 84, p. 195145, Nov 2011. [Online]. Available: https://link.aps.org/doi/10.1103/PhysRevB.84.195145

[141] A. Kshetrimayum, H.-H. Tu, and R. Orús, "All spin-1 topological phases in a single spin-2 chain," *Phys. Rev. B*, vol. 91, p. 205118, May 2015. [Online]. Available: https://link.aps.org/doi/10.1103/PhysRevB.91.205118

[142] H.-H. Tu, G.-M. Zhang, and T. Xiang, "Class of exactly solvable $so(n)$ symmetric spin chains with matrix product ground states," *Phys. Rev. B*, vol. 78, p. 094404, Sep 2008. [Online]. Available: https://link.aps.org/doi/10.1103/PhysRevB.78.094404

[143] H.-H. Tu, G.-M. Zhang, T. Xiang, Z.-X. Liu, and T.-K. Ng, "Topologically distinct classes of valence-bond solid states with their parent hamiltonians," *Phys. Rev. B*, vol. 80, p. 014401, Jul 2009. [Online]. Available: https://link.aps.org/doi/10.1103/PhysRevB.80.014401

[144] F. Pollmann and A. M. Turner, "Detection of symmetry-protected topological phases in one dimension," *Phys. Rev. B*, vol. 86, p. 125441, Sep 2012. [Online]. Available: https://link.aps.org/doi/10.1103/PhysRevB.86.125441

[145] H. Li and F. D. M. Haldane, "Entanglement spectrum as a generalization of entanglement entropy: Identification of topological order in non-abelian fractional quantum hall effect states," *Phys. Rev. Lett.*, vol. 101, p. 010504, Jul 2008. [Online]. Available: https://link.aps.org/doi/10.1103/PhysRevLett.101.010504

[146] D. Pérez-García, M. M. Wolf, M. Sanz, F. Verstraete, and J. I. Cirac, "String order and symmetries in quantum spin lattices," *Phys. Rev. Lett.*, vol. 100, p. 167202, Apr 2008. [Online]. Available: https://link.aps.org/doi/10.1103/PhysRevLett.100.167202

[147] A. Keselman and E. Berg, "Gapless symmetry-protected topological phase of fermions in one dimension," *Phys. Rev. B*, vol. 91, p. 235309, Jun 2015. [Online]. Available: https://link.aps.org/doi/10.1103/PhysRevB.91.235309

[148] C. Holzhey, F. Larsen, and F. Wilczek, "Geometric and renormalized entropy in conformal field theory," *Nuclear Physics B*, vol. 424, no. 3, pp. 443 – 467, 1994. [Online]. Available: http://www.sciencedirect.com/science/article/pii/0550321394904022

[149] G. Vidal, J. I. Latorre, E. Rico, and A. Kitaev, "Entanglement in quantum critical phenomena," *Phys. Rev. Lett.*, vol. 90, p. 227902, Jun 2003. [Online]. Available: https://link.aps.org/doi/10.1103/PhysRevLett.90.227902

[150] J. I. Latorre, E. Rico, and G. Vidal, "Ground state entanglement in quantum spin chains," *eprint arXiv:quant-ph/0304098*, Apr. 2003. [Online]. Available: http://adsabs.harvard.edu/abs/2003quant.ph..4098L

[151] A. Kshetrimayum, H.-H. Tu, and R. Orús, "Symmetry-protected intermediate trivial phases in quantum spin chains," *Phys. Rev. B*, vol. 93, p. 245112, Jun 2016. [Online]. Available: https://link.aps.org/doi/10.1103/PhysRevB.93.245112

[152] Y. Fuji, "Effective field theory for one-dimensional valence-bond-solid phases and their symmetry protection," *Phys. Rev. B*, vol. 93, p. 104425, Mar 2016. [Online]. Available: https://link.aps.org/doi/10.1103/PhysRevB.93.104425

[153] I. Affleck and A. W. W. Ludwig, "Universal noninteger "ground-state degeneracy" in critical quantum systems," *Phys. Rev. Lett.*, vol. 67, pp. 161–164, Jul 1991. [Online]. Available: https://link.aps.org/doi/10.1103/PhysRevLett.67.161

[154] G. H. Wannier, "Antiferromagnetism. the triangular ising net," *Phys. Rev.*, vol. 79, pp. 357–364, Jul 1950. [Online]. Available: https://link.aps.org/doi/10.1103/PhysRev.79.357

[155] R. Houtappel, "Order-disorder in hexagonal lattices," *Physica*, vol. 16, no. 5, pp. 425 – 455, 1950. [Online]. Available: http://www.sciencedirect.com/science/article/pii/0031891450901303

[156] A. Yoshimori, "A new type of antiferromagnetic structure in the rutile type crystal," *Journal of the Physical Society of Japan*, vol. 14, no. 6, pp. 807–821, 1959. [Online]. Available: http://dx.doi.org/10.1143/JPSJ.14.807

[157] J. Villain, "La structure des substances magnetiques," *Journal of Physics and Chemistry of Solids*, vol. 11, no. 3, pp. 303 – 309, 1959. [Online]. Available: http://www.sciencedirect.com/science/article/pii/0022369759902318

[158] T. A. Kaplan, "Classical spin-configuration stability in the presence of competing exchange forces," *Phys. Rev.*, vol. 116, pp. 888–889, Nov 1959. [Online]. Available: https://link.aps.org/doi/10.1103/PhysRev.116.888

[159] G. Toulouse, *Commun. Phys.*, June 1977.

[160] J. Villain, *Phys. C. Solid St. Phys.*, vol. 10, pp. 1717–34, 1977.

[161] G. Toulouse, *The frustration model*. Berlin, Heidelberg: Springer Berlin Heidelberg, 1980, pp. 195–203. [Online]. Available: https://doi.org/10.1007/BFb0120136

[162] J. B. Marston and C. Zeng, "Spin-Peierls and spin-liquid phases of Kagomé quantum antiferromagnets," *Journal of Applied Physics*, vol. 69, pp. 5962–5964, Apr. 1991.

[163] K. Yang, L. K. Warman, and S. M. Girvin, "Possible spin-liquid states on the triangular and kagomé lattices," *Phys. Rev. Lett.*, vol. 70, pp. 2641–2644, Apr 1993. [Online]. Available: https://link.aps.org/doi/10.1103/PhysRevLett.70.2641

[164] M. B. Hastings, "Dirac structure, rvb, and goldstone modes in the kagomé antiferromagnet," *Phys. Rev. B*, vol. 63, p. 014413, Dec 2000. [Online]. Available: https://link.aps.org/doi/10.1103/PhysRevB.63.014413

[165] F. Wang and A. Vishwanath, "Spin-liquid states on the triangular and kagomé lattices: A projective-symmetry-group analysis of schwinger boson states," *Phys. Rev. B*, vol. 74, p. 174423, Nov 2006. [Online]. Available: https://link.aps.org/doi/10.1103/PhysRevB.74.174423

[166] Y. Ran, M. Hermele, P. A. Lee, and X.-G. Wen, "Projected-wave-function study of the spin-1/2 heisenberg model on the kagomé lattice," *Phys. Rev. Lett.*, vol. 98, p. 117205, Mar 2007. [Online]. Available: https://link.aps.org/doi/10.1103/PhysRevLett.98.117205

[167] R. R. P. Singh and D. A. Huse, "Triplet and singlet excitations in the valence bond crystal phase of the kagome lattice heisenberg model," *Phys. Rev. B*, vol. 77, p. 144415, Apr 2008. [Online]. Available: https://link.aps.org/doi/10.1103/PhysRevB.77.144415

[168] G. Evenbly and G. Vidal, "Frustrated antiferromagnets with entanglement renormalization: Ground state of the spin-$\frac{1}{2}$ heisenberg model on a kagome lattice," *Phys. Rev. Lett.*, vol. 104, p. 187203, May 2010. [Online]. Available: https://link.aps.org/doi/10.1103/PhysRevLett.104.187203

[169] O. Götze, D. J. J. Farnell, R. F. Bishop, P. H. Y. Li, and J. Richter, "Heisenberg antiferromagnet on the kagome lattice with arbitrary spin: A higher-order coupled cluster treatment," *Phys. Rev. B*, vol. 84, p. 224428, Dec 2011. [Online]. Available: https://link.aps.org/doi/10.1103/PhysRevB.84.224428

[170] Y. Iqbal, F. Becca, S. Sorella, and D. Poilblanc, "Gapless spin-liquid phase in the kagome spin-$\frac{1}{2}$ heisenberg antiferromagnet," *Phys. Rev. B*, vol. 87, p. 060405, Feb 2013. [Online]. Available: https://link.aps.org/doi/10.1103/PhysRevB.87.060405

[171] S. Yan, D. A. Huse, and S. R. White, "Spin-Liquid Ground State of the S = 1/2 Kagome Heisenberg Antiferromagnet," *Science*, vol. 332, p. 1173, Jun. 2011.

[172] S. Depenbrock, I. P. McCulloch, and U. Schollwöck, "Nature of the spin-liquid ground state of the $s = 1/2$ heisenberg model on the kagome lattice," *Phys. Rev. Lett.*, vol. 109, p. 067201, Aug 2012. [Online]. Available: https://link.aps.org/doi/10.1103/PhysRevLett.109.067201

[173] P. W. ANDERSON, "Resonating valence bonds: A new kind of insulator?" vol. 8, pp. 153–160, 02 1973.

[174] T.-H. Han, J. S. Helton, S. Chu, D. G. Nocera, J. A. Rodriguez-Rivera, C. Broholm, and Y. S. Lee, "Fractionalized excitations in the spin-liquid state of a kagome-lattice antiferromagnet," *Nature*, vol. 492, pp. 406–410, Dec. 2012.

[175] R. R. P. Singh and D. A. Huse, "Ground state of the spin-1/2 kagome-lattice heisenberg antiferromagnet," *Phys. Rev. B*, vol. 76, p. 180407, Nov 2007. [Online]. Available: https://link.aps.org/doi/10.1103/PhysRevB.76.180407

[176] H. J. Liao, Z. Y. Xie, J. Chen, Z. Y. Liu, H. D. Xie, R. Z. Huang, B. Normand, and T. Xiang, "Gapless spin-liquid ground state in the $s = 1/2$ kagome antiferromagnet," *Phys. Rev. Lett.*, vol. 118, p. 137202, Mar 2017. [Online]. Available: https://link.aps.org/doi/10.1103/PhysRevLett.118.137202

[177] T. Liu, W. Li, A. Weichselbaum, J. von Delft, and G. Su, "Simplex valence-bond crystal in the spin-1 kagome heisenberg antiferromagnet," *Phys. Rev. B*, vol. 91, p. 060403, Feb 2015. [Online]. Available: https://link.aps.org/doi/10.1103/PhysRevB.91.060403

[178] H. J. Changlani and A. M. Läuchli, "Trimerized ground state of the spin-1 heisenberg antiferromagnet on the kagome lattice," *Phys. Rev. B*, vol. 91, p. 100407, Mar 2015. [Online]. Available: https://link.aps.org/doi/10.1103/PhysRevB.91.100407

[179] W. Li, A. Weichselbaum, J. von Delft, and H.-H. Tu, "Hexagon-singlet solid ansatz for the spin-1 kagome antiferromagnet," *Phys. Rev. B*, vol. 91, p. 224414, Jun 2015. [Online]. Available: https://link.aps.org/doi/10.1103/PhysRevB.91.224414

[180] T. Picot and D. Poilblanc, "Nematic and supernematic phases in kagome quantum antiferromagnets under the influence of a magnetic field," *Phys. Rev. B*, vol. 91, p. 064415, Feb 2015. [Online]. Available: https://link.aps.org/doi/10.1103/PhysRevB.91.064415

[181] H. C. Jiang, Z. Y. Weng, and T. Xiang, "Accurate determination of tensor network state of quantum lattice models in two dimensions," *Phys. Rev. Lett.*, vol. 101, p. 090603, Aug 2008. [Online]. Available: https://link.aps.org/doi/10.1103/PhysRevLett.101.090603

[182] J. Jordan, R. Orús, G. Vidal, F. Verstraete, and J. I. Cirac, "Classical simulation of infinite-size quantum lattice systems in two spatial dimensions," *Phys. Rev. Lett.*, vol. 101, p. 250602, Dec 2008. [Online]. Available: https://link.aps.org/doi/10.1103/PhysRevLett.101.250602

[183] R. Orús and G. Vidal, "Simulation of two-dimensional quantum systems on an infinite lattice revisited: Corner transfer matrix for tensor contraction," *Phys. Rev. B*, vol. 80, p. 094403, Sep 2009. [Online]. Available: https://link.aps.org/doi/10.1103/PhysRevB.80.094403

[184] H. N. Phien, J. A. Bengua, H. D. Tuan, P. Corboz, and R. Orús, "Infinite projected entangled pair states algorithm improved: Fast full update and gauge fixing," *Phys. Rev. B*, vol. 92, p. 035142, Jul 2015. [Online]. Available: https://link.aps.org/doi/10.1103/PhysRevB.92.035142

[185] R. Orús and G. Vidal, "Infinite time-evolving block decimation algorithm beyond unitary evolution," *Phys. Rev. B*, vol. 78, p. 155117, Oct 2008. [Online]. Available: https://link.aps.org/doi/10.1103/PhysRevB.78.155117

[186] T. Picot, M. Ziegler, R. Orús, and D. Poilblanc, "Spin-s kagome quantum antiferromagnets in a field with tensor networks," *Phys. Rev. B*, vol. 93, p. 060407, Feb 2016. [Online]. Available: https://link.aps.org/doi/10.1103/PhysRevB.93.060407

[187] M. Ziegler, "Tensor network methods for infinite 2d systems," 2015. [Online]. Available: http://www.romanorus.com/MasterThesis_MarcZiegler.pdf

[188] K. Hida, "Magnetization process of the s=1 and 1/2 uniform and distorted kagom heisenberg antiferromagnets," *Journal of the Physical Society of Japan*, vol. 70, no. 12, pp. 3673–3677, 2001. [Online]. Available: http://dx.doi.org/10.1143/JPSJ.70.3673

[189] J. Schulenburg, A. Honecker, J. Schnack, J. Richter, and H.-J. Schmidt, "Macroscopic magnetization jumps due to independent magnons in frustrated quantum spin lattices," *Phys. Rev. Lett.*, vol. 88, p. 167207, Apr 2002. [Online]. Available: https://link.aps.org/doi/10.1103/PhysRevLett.88.167207

[190] J. Richter, J. Schulenburg, and A. Honecker, "Quantum Magnetism in Two Dimensions: From Semi-classical Néel Order to Magnetic Disorder," in *Quantum Magnetism*, ser. Lecture Notes in Physics, Berlin Springer Verlag, U. Schollwöck, J. Richter, D. J. J. Farnell, and R. F. Bishop, Eds., vol. 645, 2004, p. 85.

[191] A. Honecker, J. Schulenburg, and J. Richter, "Magnetization plateaus in frustrated antiferromagnetic quantum spin models," *Journal of Physics: Condensed Matter*, vol. 16, no. 11, p. S749, 2004. [Online]. Available: http://stacks.iop.org/0953-8984/16/i=11/a=025

[192] H. Nakano and T. Sakai, "Magnetization process of kagome-lattice heisenberg antiferromagnet," *Journal of the Physical Society of Japan*, vol. 79, no. 5, p. 053707, 2010. [Online]. Available: http://dx.doi.org/10.1143/JPSJ.79.053707

[193] T. Sakai and H. Nakano, "Critical magnetization behavior of the triangular- and kagome-lattice quantum antiferromagnets," *Phys. Rev. B*, vol. 83, p. 100405, Mar 2011. [Online]. Available: https://link.aps.org/doi/10.1103/PhysRevB.83.100405

[194] S. Capponi, O. Derzhko, A. Honecker, A. M. Läuchli, and J. Richter, "Numerical study of magnetization plateaus in the spin-$\frac{1}{2}$ kagome heisenberg antiferromagnet," *Phys. Rev. B*, vol. 88, p. 144416, Oct 2013. [Online]. Available: https://link.aps.org/doi/10.1103/PhysRevB.88.144416

[195] S. Nishimoto, N. Shibata, and C. Hotta, "Controlling frustrated liquids and solids with an applied field in a kagome Heisenberg antiferromagnet," *Nature Communications*, vol. 4, p. 2287, Aug. 2013.

[196] A. Kshetrimayum, T. Picot, R. Orús, and D. Poilblanc, "Spin-$\frac{1}{2}$ kagome xxz model in a field: Competition between lattice nematic and solid orders," *Phys. Rev. B*, vol. 94, p. 235146, Dec 2016. [Online]. Available: https://link.aps.org/doi/10.1103/PhysRevB.94.235146

[197] D. C. Cabra, M. D. Grynberg, P. C. W. Holdsworth, A. Honecker, P. Pujol, J. Richter, D. Schmalfuß, and J. Schulenburg, "Quantum kagomé antiferromagnet in a magnetic field: Low-lying nonmagnetic excitations versus valence-bond crystal order," *Phys. Rev. B*, vol. 71, p. 144420, Apr 2005. [Online]. Available: https://link.aps.org/doi/10.1103/PhysRevB.71.144420

[198] K. Kumar, K. Sun, and E. Fradkin, "Chern-simons theory of magnetization plateaus of the spin-$\frac{1}{2}$ quantum xxz heisenberg model on the kagome lattice," *Phys. Rev. B*, vol. 90, p. 174409, Nov 2014. [Online]. Available: https://link.aps.org/doi/10.1103/PhysRevB.90.174409

[199] R. Orús, T.-C. Wei, O. Buerschaper, and A. García-Saez, "Topological transitions from multipartite entanglement with tensor networks: A procedure for sharper and faster characterization," *Phys. Rev. Lett.*, vol. 113, p. 257202, Dec 2014. [Online]. Available: https://link.aps.org/doi/10.1103/PhysRevLett.113.257202

[200] J. I. Cirac, D. Poilblanc, N. Schuch, and F. Verstraete, "Entanglement spectrum and boundary theories with projected entangled-pair states," *Phys. Rev. B*, vol. 83, p. 245134, Jun 2011. [Online]. Available: https://link.aps.org/doi/10.1103/PhysRevB.83.245134

[201] T. B. Wahl, H.-H. Tu, N. Schuch, and J. I. Cirac, "Projected entangled-pair states can describe chiral topological states," *Phys. Rev. Lett.*, vol. 111, p. 236805, Dec 2013. [Online]. Available: https://link.aps.org/doi/10.1103/PhysRevLett.111.236805

[202] M. Schlosshauer, "Decoherence, the measurement problem, and interpretations of quantum mechanics," *Rev. Mod. Phys.*, vol. 76, pp. 1267–1305, Feb 2005. [Online]. Available: https://link.aps.org/doi/10.1103/RevModPhys.76.1267

[203] S. Vinjanampathy and J. Anders, "Quantum thermodynamics," *Contemporary Physics*, vol. 57, pp. 545–579, Oct. 2016.

[204] M. Kliesch, D. Gross, and J. Eisert, "Matrix-product operators and states: Np-hardness and undecidability," *Phys. Rev. Lett.*, vol. 113, p. 160503, Oct 2014. [Online]. Available: https://link.aps.org/doi/10.1103/PhysRevLett.113.160503

[205] H. Weimer, "Variational analysis of driven-dissipative rydberg gases," *Phys. Rev. A*, vol. 91, p. 063401, Jun 2015. [Online]. Available: https://link.aps.org/doi/10.1103/PhysRevA.91.063401

[206] ——, "Variational principle for steady states of dissipative quantum many-body systems," *Phys. Rev. Lett.*, vol. 114, p. 040402, Jan 2015. [Online]. Available: https://link.aps.org/doi/10.1103/PhysRevLett.114.040402

[207] A. Kshetrimayum, H. Weimer, and R. Orús, "A simple tensor network algorithm for two-dimensional steady states," *Nature Communications*, vol. 8, p. 1291, Nov. 2017.

[208] M. Nielsen and I. Chuang, *Quantum Computation and Quantum Information*. Cambridge University Press, Cambridge, 2000.

[209] G. D. las Cuevas, N. Schuch, D. Prez-Garca, and J. I. Cirac, "Purifications of multipartite states: limitations and constructive methods," *New Journal of Physics*, vol. 15, no. 12, p. 123021, 2013. [Online]. Available: http://stacks.iop.org/1367-2630/15/i=12/a=123021

[210] A. H. Werner, D. Jaschke, P. Silvi, M. Kliesch, T. Calarco, J. Eisert, and S. Montangero, "Positive tensor network approach for simulating open quantum many-body systems," *Phys. Rev. Lett.*, vol. 116, p. 237201, Jun 2016. [Online]. Available: https://link.aps.org/doi/10.1103/PhysRevLett.116.237201

[211] J. Cui, J. I. Cirac, and M. C. Bañuls, "Variational matrix product operators for the steady state of dissipative quantum systems," *Phys. Rev. Lett.*, vol. 114, p. 220601, Jun 2015. [Online]. Available: https://link.aps.org/doi/10.1103/PhysRevLett.114.220601

[212] Z. Cai and T. Barthel, "Algebraic versus exponential decoherence in dissipative many-particle systems," *Phys. Rev. Lett.*, vol. 111, p. 150403, Oct 2013. [Online]. Available: https://link.aps.org/doi/10.1103/PhysRevLett.111.150403

[213] L. Bonnes, D. Charrier, and A. M. Läuchli, "Dynamical and steady-state properties of a bose-hubbard chain with bond dissipation: A study based on matrix product operators," *Phys. Rev. A*, vol. 90, p. 033612, Sep 2014. [Online]. Available: https://link.aps.org/doi/10.1103/PhysRevA.90.033612

[214] E. Mascarenhas, H. Flayac, and V. Savona, "Matrix-product-operator approach to the nonequilibrium steady state of driven-dissipative quantum arrays," *Phys. Rev. A*, vol. 92, p. 022116, Aug 2015. [Online]. Available: https://link.aps.org/doi/10.1103/PhysRevA.92.022116

[215] A. A. Gangat, T. I, and Y.-J. Kao, "Steady states of infinite-size dissipative quantum chains via imaginary time evolution," *Phys. Rev. Lett.*, vol. 119, p. 010501, Jul 2017. [Online]. Available: https://link.aps.org/doi/10.1103/PhysRevLett.119.010501

[216] T. E. Lee, S. Gopalakrishnan, and M. D. Lukin, "Unconventional magnetism via optical pumping of interacting spin systems," *Phys. Rev. Lett.*, vol. 110, p. 257204, Jun 2013. [Online]. Available: https://link.aps.org/doi/10.1103/PhysRevLett.110.257204

[217] J. Jin, A. Biella, O. Viyuela, L. Mazza, J. Keeling, R. Fazio, and D. Rossini, "Cluster mean-field approach to the steady-state phase diagram of dissipative spin systems," *Phys. Rev. X*, vol. 6, p. 031011, Jul 2016. [Online]. Available: https://link.aps.org/doi/10.1103/PhysRevX.6.031011

[218] S. Finazzi, A. Le Boité, F. Storme, A. Baksic, and C. Ciuti, "Corner-space renormalization method for driven-dissipative two-dimensional correlated systems," *Phys. Rev. Lett.*, vol. 115, p. 080604, Aug 2015. [Online]. Available: https://link.aps.org/doi/10.1103/PhysRevLett.115.080604

[219] S. Sahin, K. P. Schmidt, and R. Ors, "Entanglement continuous unitary transformations," *EPL (Europhysics Letters)*, vol. 117, no. 2, p. 20002, 2017. [Online]. Available: http://stacks.iop.org/0295-5075/117/i=2/a=20002

[220] E. Mascarenhas, H. Flayac, and V. Savona, "Matrix-product-operator approach to the nonequilibrium steady state of driven-dissipative quantum arrays," *Phys. Rev. A*, vol. 92, p. 022116, Aug 2015. [Online]. Available: https://link.aps.org/doi/10.1103/PhysRevA.92.022116

[221] F. Letscher, O. Thomas, T. Niederprüm, M. Fleischhauer, and H. Ott, "Bistability versus metastability in driven dissipative rydberg gases," *Phys. Rev. X*, vol. 7, p. 021020, May 2017. [Online]. Available: https://link.aps.org/doi/10.1103/PhysRevX.7.021020

[222] N. Malossi, M. M. Valado, S. Scotto, P. Huillery, P. Pillet, D. Ciampini, E. Arimondo, and O. Morsch, "Full counting statistics and phase diagram of a dissipative rydberg gas," *Phys. Rev. Lett.*, vol. 113, p. 023006, Jul 2014. [Online]. Available: https://link.aps.org/doi/10.1103/PhysRevLett.113.023006

[223] T. E. Lee, H. Häffner, and M. C. Cross, "Antiferromagnetic phase transition in a nonequilibrium lattice of rydberg atoms," *Phys. Rev. A*, vol. 84, p. 031402, Sep 2011. [Online]. Available: https://link.aps.org/doi/10.1103/PhysRevA.84.031402

[224] M. Marcuzzi, E. Levi, S. Diehl, J. P. Garrahan, and I. Lesanovsky, "Universal nonequilibrium properties of dissipative rydberg gases," *Phys. Rev. Lett.*, vol. 113, p. 210401, Nov 2014. [Online]. Available: https://link.aps.org/doi/10.1103/PhysRevLett.113.210401

[225] M. F. Maghrebi and A. V. Gorshkov, "Nonequilibrium many-body steady states via keldysh formalism," *Phys. Rev. B*, vol. 93, p. 014307, Jan 2016. [Online]. Available: https://link.aps.org/doi/10.1103/PhysRevB.93.014307

[226] M. Höning, D. Muth, D. Petrosyan, and M. Fleischhauer, "Steady-state crystallization of rydberg excitations in an optically driven lattice gas," *Phys. Rev. A*, vol. 87, p. 023401, Feb 2013. [Online]. Available: https://link.aps.org/doi/10.1103/PhysRevA.87.023401

[227] M. Hoening, W. Abdussalam, M. Fleischhauer, and T. Pohl, "Antiferromagnetic long-range order in dissipative rydberg lattices," *Phys. Rev. A*, vol. 90, p. 021603, Aug 2014. [Online]. Available: https://link.aps.org/doi/10.1103/PhysRevA.90.021603

[228] J. J. Mendoza-Arenas, S. R. Clark, S. Felicetti, G. Romero, E. Solano, D. G. Angelakis, and D. Jaksch, "Beyond mean-field bistability in driven-dissipative lattices: Bunching-antibunching transition and quantum simulation," *Phys. Rev. A*, vol. 93, p. 023821, Feb 2016. [Online]. Available: https://link.aps.org/doi/10.1103/PhysRevA.93.023821

[229] R. Rota, F. Storme, N. Bartolo, R. Fazio, and C. Ciuti, "Critical behavior of dissipative two-dimensional spin lattices," *Phys. Rev. B*, vol. 95, p. 134431, Apr 2017. [Online]. Available: https://link.aps.org/doi/10.1103/PhysRevB.95.134431

[230] A. Lucia, T. S. Cubitt, S. Michalakis, and D. Pérez-García, "Rapid mixing and stability of quantum dissipative systems," *Phys. Rev. A*, vol. 91, p. 040302, Apr 2015. [Online]. Available: https://link.aps.org/doi/10.1103/PhysRevA.91.040302

[231] M. Roncaglia, M. Rizzi, and J. I. Cirac, "Pfaffian state generation by strong three-body dissipation," *Phys. Rev. Lett.*, vol. 104, p. 096803, Mar 2010. [Online]. Available: https://link.aps.org/doi/10.1103/PhysRevLett.104.096803

[232] C. Holzhey, F. Larsen, and F. Wilczek, "Geometric and renormalized entropy in conformal field theory," *Nuclear Physics B*, vol. 424, no. 3, pp. 443 – 467, 1994. [Online]. Available: http://www.sciencedirect.com/science/article/pii/0550321394904022

[233] J. L. Cardy and I. Peschel, "Finite-size dependence of the free energy in two-dimensional critical systems," *Nuclear Physics B*, vol. 300, pp. 377 – 392, 1988. [Online]. Available: http://www.sciencedirect.com/science/article/pii/0550321388906049

[234] P. Calabrese and J. Cardy, "Entanglement entropy and quantum field theory," *Journal of Statistical Mechanics: Theory and Experiment*, vol. 2004, no. 06, p. P06002, 2004. [Online]. Available: http://stacks.iop.org/1742-5468/2004/i=06/a=P06002